Title	Studies on Control of Phase Variability in Lipid Nanoparticles and Its Effect on Their Interaction with Cell Membranes
Author(s)	Xuehui, Rui
Citation	大阪大学, 2024, 博士論文
Version Type	VoR
URL	https://doi.org/10.18910/101459
rights	
Note	

Studies on Control of Phase Variability in Lipid Nanoparticles and Its Effect on Their Interaction with Cell Membranes

XUEHUI RUI

NOVEMBER 2024

Studies on Control of Phase Variability in Lipid Nanoparticles and Its Effect on Their Interaction with Cell Membranes

A dissertation submitted to

THE GRADUATE SCHOOL OF ENGINEERING SCIENCE

OSAKA UNIVERSITY

in partial fulfillment of the requirements for the degree of

DOCTRO OF PHILOSOPHY IN ENGINEERING

BY

Xuehui Rui

NOVEMBER 2024

Abstract

Lipid-based self-assembling nanomaterials hold significant promise across a range of applications. The organization of lipid molecules into distinct nanomaterial phases is influenced by specific lipid formulations and preparation techniques, enabling transitions between different states. This research prepared lipid nanoparticles (LNPs) in various phases and assessed their impact on the cell plasma membrane during incubation. Interactions with these lipid nanoparticles induced alterations in the lipid composition and biophysical properties of the cell plasma membrane.

Chapter 1 introduces the fundamental concepts of lipid-based self-assembling nanoparticles and key properties related to the biophysical properties of cytoplasmic membranes. This chapter offers insights into LNP systems from three key perspectives: lipid/amphiphile molecular shapes, membrane packing characteristics, and resulting assembly morphologies. Additionally, it reviews studies on membrane polarity and fluidity, shedding light on the interactions between LNPs and cell membranes.

Chapter 2 focuses on the preparation and characterization of LNPs in different lyotropic phases. Depending on the lipid composition and fabrication methodologies, LNPs could form micelle, lamellar vesicle (*La*), cubic (Q_{II}) and hexagonal (H_{II}) phases. Techniques such as small-angle X-ray scattering (SAXS), transmission electron microscopy (TEM), and cryo-transmission electron microscopy (cryo-TEM) were employed to comprehensively analyze LNP lyotropic phase status and morphologies. Key structural parameters of the LNPs across various phases were calculated and compared.

Chapter 3 investigates the physicochemical properties of lipid membranes across different LNP phases. These properties were characterized using fluorescence probes (Laurdan and DPH) and Raman spectroscopy. The 2-OHOA/MO binary component system served as an ideal model for studying membrane properties during the transition from lamellar (*La*) to cubic (Q_{II}) phases. The results provided insights into changes in lipid packing statuses, membrane-water interfacial polarities, and lyotropic phase transitions.

Chapter 4 examines the polarities of the cell plasma membranes using Laurdan two-

photon microscopy (TPM). The study reveals that different cell types exhibit distinct lipid membrane polarities. Additionally, the high resolution of TPM enables the visualization of heterogeneity in membrane fluidity and polarity. Basing on this methodology, this study further investigated how the LNPs modulates the biophysical properties of cell plasma membranes. This study proposes that nanoparticle internalization influences cell plasma membrane characteristics directly or indirectly.

Chapter 5 elucidates the impact of LNPs on cellular plasma membrane dynamics from both physical and biological perspectives. Building on these findings, this study introduced a novel strategy for coating cubic-phase lyotropic liquid crystalline nanoparticles (Cubosomes) with cell membranes. This biomimetic surface modification aims to create a stabilized, immune-evasive nanodrug delivery system (DDS). The established nano-DDS system was evaluated both *in vitro* and *in vivo*, focusing on stability, drug release profiles, macrophage evasion efficiency, and *in vivo* distribution patterns.

Chapter 6 presents the general conclusions of this work. The findings advance the understanding of lyotropic phase behaviors in LNPs, examining lipid/amphiphile shapes, membrane packing characteristics, and the acid dissociation constant of ionizable lipids. This study also explores how LNPs interact with cell plasma membranes and offers methodologies to assess changes in cell membrane biophysical properties upon LNP contact. These insights may guide the optimization of LNPs, enhancing their effectiveness in drug delivery applications.

Contents

Chapter 1

General Introduction

Self-assembled lipid nanoparticles (LNPs) serve as a versatile and efficient platform for delivering a variety of biological materials as well as small molecule drugs. In the perspective of self-assemblies, the lyotropic liquid crystalline phase behavior, morphologies, and surface properties of LNPs vary based on their compositions and preparation methods. From the viewpoint of lipid membrane system, distinct LNPs would have different lipid packing status and lipid membrane interfacial hydration status. The distinct lyotropic phases and membrane properties of LNPs not only influence their cargo loading capacities/releasing patterns, but also impact their interaction mechanisms with cells. LNPs can differently impact cellular plasma membranes through physical interactions or biological mechanisms. This chapter introduces fundamental concepts and key studies related to LNP lyotropic phase behavior, cellular plasma membrane properties, and LNP-cell membrane interactions.

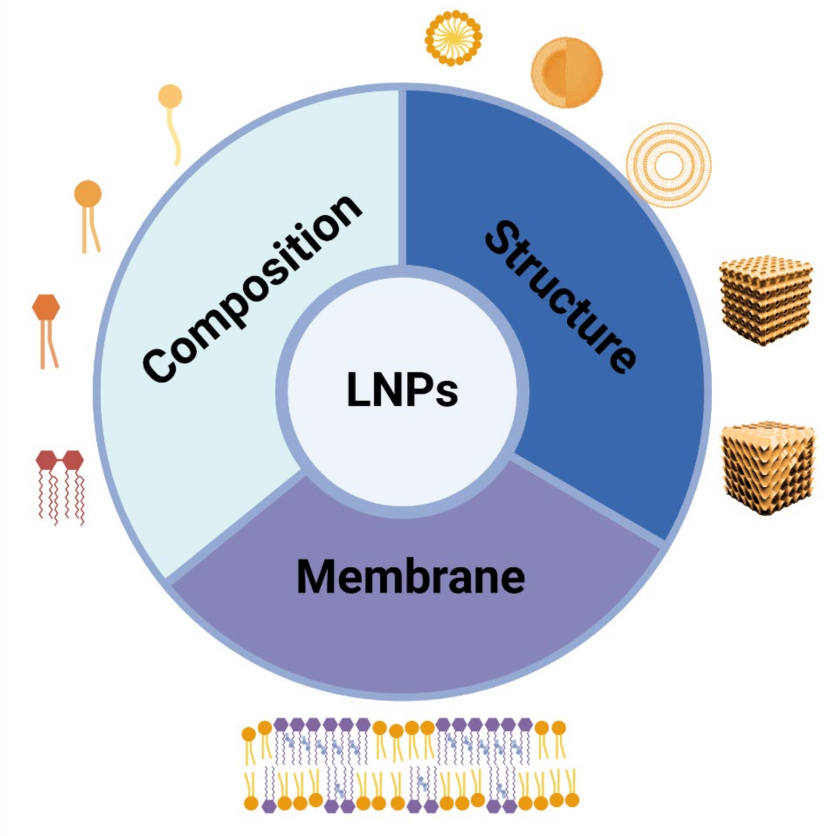

Figure 1-1. Key Concepts of Lipid Nanoparticles (LNPs) in This Study

1. Lipid self-assembled system

Lipid self-assembly refers to the process by which lipids spontaneously organize into ordered structures in aqueous environments due to their amphiphilic nature. Lipids contain both hydrophobic (water-repelling) and hydrophilic (water-attracting) regions, typically represented by several hydrophobic tails (usually aliphatic chains) and a hydrophilic head group (such as phosphate or choline). When placed in water, different lipids arrange themselves to minimize unfavorable interactions, resulting in the formation of various structures. Inspired by the biologically significant, hierarchically ordered structures found in nature, lipid self-assembled systems have been creatively engineered for various biomedical applications, including bio-imaging, diagnostics, and controlled drug delivery.

Lipid lyotropic liquid crystalline phase behavior refers to the diverse lyotropic phases that lipid molecules can form in aqueous solutions, depending on their nature and preparation process (Raffaele et al., 2019). Key self-assembled lipid structures include micelles, lamellar vesicles (liposome), cubic phased nanoparticles (cubosome) and hexagonal phased particles (hexosome). Micelles are spherical assemblies where the hydrophobic tails aggregate in the center, away from the water, while the hydrophilic heads face outward, interacting with the surrounding water (Tanford et al., 1972). Micelles are often used for solubilizing hydrophobic drugs in aqueous solutions (Kim et al., 2009). Lipids can form bilayers, where two sheets of lipids align tail-to-tail with the hydrophilic heads facing outward on both sides (Akbarzadeh et al., 2013). When the bilayer folds into a spherical shape, it forms a liposome, a structure with an internal aqueous core. Liposomes are commonly used for drug delivery because they can encapsulate both hydrophilic and hydrophobic molecules, protecting them from degradation. Cubosome consists of a highly ordered three-dimensional network of interconnected channels (Garg et al., 2007). This structure is known for its ability to host a variety of guest molecules, making it suitable for both hydrophobic and hydrophilic drugs delivery applications. Lipids can also organize into more complex structures such as hexagonal phases, where the lipids form a honeycomb-like array of tubes (Hirlekar et al., 2010). These structures are particularly relevant for membrane fusion and can influence the release of encapsulated drugs.

A key concept in understanding lipid lyotropic phase behavior is the critical packing parameter (*CPP*) (Israelachvili et al., 1976), which predicts how the molecular geometry of lipids influences their self-assembled morphology. The molecular shape of lipids or amphiphiles is a critical factor in lipid membrane self-assembly. The physical dimensions of a lipid component can often predict its phase behavior upon hydration and its position within the membrane structures. By considering interaction free energies, molecular geometry, and entropy, theoreticians have developed a dimensionless parameter called the critical packing parameter (*CPP*), which is instrumental in predicting the lipid shapes, lipid membrane packing statuses and the final morphologies of lipid aggregates. *CPP* is given by a descriptive equation: $CPP = \nu/(\alpha_0 \cdot l_c)$, where, "$\nu$" is the hydrophobic tail volume, "α_0" is the area of hydrophilic headgroup area, and "l_c" is the critical length of the hydrocarbon chain. α_0, ν, and l_c are all estimable or measurable.

The volume of the hydrophobic tail can be approximated using molecular dimensions. For hydrocarbons, a common approach is to use the Tanford equation (Tanford, 1972): $\nu = (27.4 + 26.9 \cdot n)$ [Å^3], where n is the total number of carbon atoms in the hydrocarbon tail. The headgroup area (α_0) depends on the type of lipid and can be measured experimentally using techniques like X-ray scattering or surface pressure-area isotherms. For phosphatidylcholine (PC), the approximate $\alpha_0 \approx 71.7$ [Å^2]; for Phosphatidylethanolamine (PE), the approximate $\alpha_0 \approx 42$ [Å^2]; for cholesterol, the approximate $\alpha_0 \approx 19$ [Å^2] (Kumar 1991). The critical tail length (l_c) can be approximated as the maximum extended length of the lipid hydrophobic tails. For a hydrocarbon chain, this is typically calculated as: $lc = 1.5 + 1.265 \cdot n_c$ [Å], where n_c is the total number of carbon atoms in one hydrocarbon chain. Also, some research (Carnie et al., 1979) reported an optimized equation for lc calculation: $lc = 1.5 + 1.265 \cdot n_c'$ [Å], where n_c' is the number of carbon atoms of the hydrocarbon chain that are embedded in the hydrocarbon core. n_c' is usually less than the n_c $(n \approx 0.8 \cdot n_c')$.

As shown in **Fig. 1-2**, the *CPP* values of lipids describe the shapes of lipid amphiphiles upon hydration. Lipid molecules with $CPP < 1$ adopt a "cone" shape, leading to formation of positive membrane curvature. Lipids with $CPP \approx 1$ adopt a "cylindrical" shape and form planar membranes with zero curvature. Conversely, lipid molecules with $CPP > 1$ adopt an "inverted-cone" shape, resulting in negative membrane curvature. Additionally, the morphologies of lipid self-assemblies are closely related to lipid membrane curvature, allowing predictions of LNP morphologies based on *CPP* values. When *CPP* < 1/3, lipids form spherical micelles; when 1/3< *CPP* < 1/2, lipids form cylindrical shaped micelles; when 1/2< *CPP* <1, lipids form into lamellar (Lα) structures (vesicles or planner). Lipid molecules with a *CPP* greater than 1 tend to form negatively curved membranes and inverse phases in aqueous environments, such as the inverted micelles, hexagonal (H_{II}) phase or bicontinuous cubic (Q_{II}) phase. **Table 1-1** summarized the literature reported *CPP* values of some commonly used amphiphiles for drug delivery.

For the drug delivery system, the LNP formulations are usually multicomponents. The *CPP* values of a mixture of the lipids could be predicated by defining a mean *CPP* for the mixed amphiphilic system using the following equation (Kumar, 1991). $CPP_{mean} = \sum_i X_i \times CPP_i$. Where X_i donates the molar ratio of the i^{th} component in the mixture and CPP_i is the *CPP* of i^{th} lipid component.

However, the *CPP* concepts are based on the “ideal” self-assembly of single-component lipids or mixtures, assuming minimal specific interactions between molecules. Various additional factors such as ionic strength, temperature, preparation methods and cargo molecule loading would significantly influence the packing state of lipid amphiphiles, thus altering their physical properties and morphologies.

For instance, temperature changes can alter the structural parameters of lipids. As temperature increases, both the hydrophobic tail volume (ν) and the area of the hydrophilic headgroup (α_0) of phosphatidylcholines (PCs) increase (Costigan et al., 2000). This temperature-induced expansion in both parameters can influence the *CPP*, potentially leading to a shift in lipid morphology and membrane curvature. Additionally, the encapsulation or loading of cargo molecules in LNPs can alter the lipid packing arrangement.

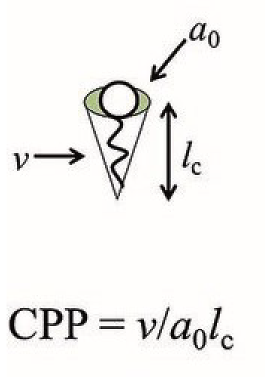

v: Hydrophobic tail volume [Å^3]

α_0: Area of hydrophilic headgroup [Å^2]

l_c: Critical length of the hydrocarbon chain [Å]

Lipid Shape	Membrane Packing		Final Assembly	Inner Structure
Cone shape 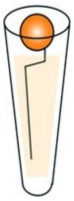 ($CPP < 1$)	Positive Curvature 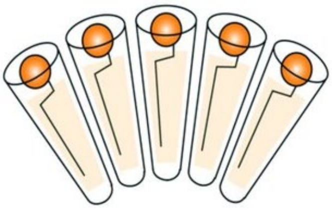	**CPP**	Micelle 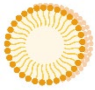	Hydrophobic core
Cylindrical 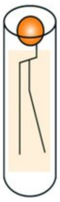 ($CPP = 1$)	Zero Curvature 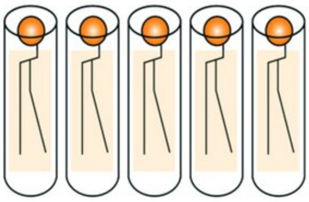		Liposome ($L\alpha$) 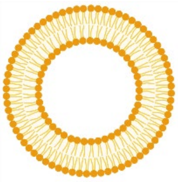	Hydrophilic water pool
Inverted cone shape 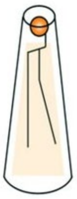 ($CPP > 1$)	Negative Curvature 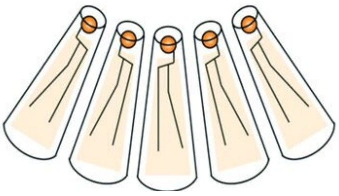		Cubosome (Q_{II}) 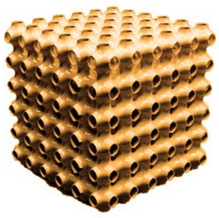	Hydrophilic water channel 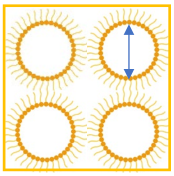
			Hexosome (H_{II}) 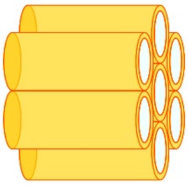	Hydrophilic water channel 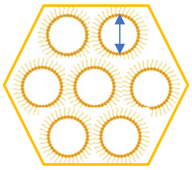

Figure. 1-2. Illustration of *CPP*, Membrane Packing and Diverse Phases of Lipid-Self Assemble Nanoparticles.

Table 1-1 Literature Reported *CPP* Values of Some Amphiphiles

Lipid Type	Name	Structure	Literature Values					Phase	Temperature	Reference
			α_0 [Å^2]	l_c [Å]	ν [Å^3]	CPP	Shape			
PC	DOPC (18:1 PC)	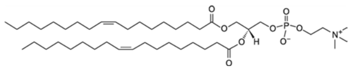	71	19.7	1139.8	0.81	Cone	Lα	N.A.	Kumar 1991
			74.3	17.4	1295.4	1.00	Cylindrical	Lα	298 K	Costigan et al., 2000
	DSPC (18:0 PC)	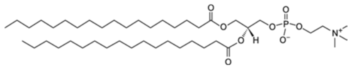	71.7	19.7	1139.8	0.81	Cone	Lα	N.A.	Kumar 1991
	DPPC (16:0 PC)	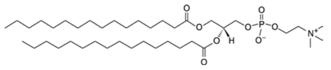	71	20.48	847.0	0.58	Cone	Lα	293 K	Reiss et al., 1976
			62.71	19.22	722.57	0.60	Cone	Lα	293 K	Kobierski et al., 2022
			71.7	17.7	1016.2	0.80	Cone	Lα	N.A.	Kumar 1991
			60.0	17.6	871.0	0.83	Cone	Lα	293 K	Angelov et al., 1999
	DMPC (14:0 PC)	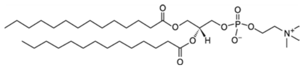	71.7	15.7	892.6	0.79	Cone	Lα	N.A.	Kumar 1991
			64.9	16.8	1089.9	1.00	Cylindrical	Lα	298 K	Costigan et al., 2000
	DLPC (12:0 PC)	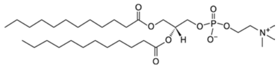	71.7	13.6	169	0.79	Cone	Lα	N.A.	Kumar 1991
	POPC (16:0-18:1 PC)	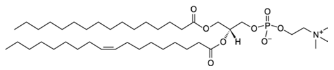	71	20.48	910.0	0.62	Cone	Lα	293 K	Reiss et al., 1976
			71.95	16.65	735.40	0.61	Cone	Lα	293 K	Kobierski et al., 2022
			65	23	969.4	0.65	Cone	Lα	293 K	Lantzsch et al., 1996

Lipid Type	Name	Structure	Literature Values					Phase	Temperature	Reference
			α_0 [Å^2]	l_c [Å]	ν [Å^3]	CPP	Shape			
PE	DOPE (18:1 PE)	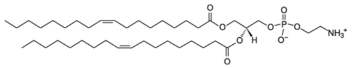	46.0	18.6	953.0	1.11	Inverted cone	H_{II}	293 K	Angelov et al., 1999
	POPE (16:0-18:1 PE)	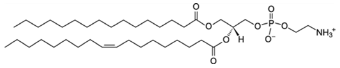	41	20.48	910.0	1.08	Inverted cone	H_{II}	293 K	Reiss et al., 1976
	DPPE (16:0 PE)	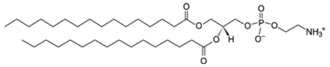	41	20.48	847.0	1.00	Cylindrical	H_{II}	293 K	Reiss et al., 1976
SL	Sphingomyelin (SM)	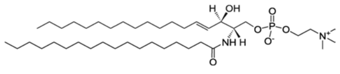	55	20.48	837.6	0.74	Cone	Lα	293 K	Reiss et al., 1976
Chol	Cholesterol	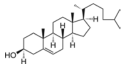	19	17.25	400.0	1.22	Inverted cone	Lα	293 K	Reiss et al., 1976
Fatty Acid	Monoolein (MO)	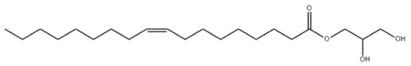	34.55	15.5	628.5	1.17	Inverted cone	Pn3m	318 K	Kulkarni et al., 2010
	Monoelaidin (ME)	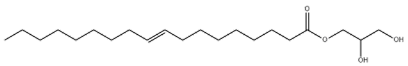	24.80	18.5	533.4	1.16	Inverted cone	Pn3m	318 K	Kulkarni et al., 2010
	Monovaccenin (MV)	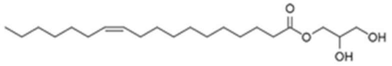	33.76	16.3	628.5	1.14	Inverted cone	Pn3m	318 K	Kulkarni et al., 2010
	Monolinolein (ML)	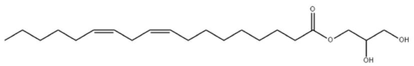	44.40	14.2	741.3	1.18	Inverted cone	Pn3m	318 K	Kulkarni et al., 2010

PC: Phosphatidylcholine; PE: Phosphatidylethanolamine; SL: Sphingolipid; Chol: Cholesterol.

In multi-component LNP systems, lipids may mix homogeneously at specific molar ratios, while phase separation can occur at others, influenced by factors like charge distribution, hydrogen bonding, and specific functional groups (Angelov et al., 1999). This variability can result in significantly different α_0 for the same lipid molecule, depending on the local environment and the presence of other components.

Another crucial factor in engineering lipid self-assembly systems is the ionization state of the lipids, commonly described by their apparent acid dissociation constant (p*K*a). Changes in ionic strength and pH can significantly influence the α_0 of ionizable lipids, subsequently altering their *CPP*. For instance, the *CPP* values of the ionizable lipids ALC-0315 (used in Moderna's LNPs) and SM-102 (used in Pfizer's LNPs) are 1.33 and 1.05 in their neutral and charged states for ALC-0315, and 1.30 and 0.96 for SM-102, respectively (Yu et al., 2023). Furthermore, while *CPP* theory generally applies under neutral conditions, strong electrostatic repulsion between highly charged lipids can considerably impact membrane packing status, leading to pH-dependent phase transitions. This underscores the pivotal role of lipid ionization states, governed by environmental pH and ionic strength, in self-assembly behavior. Incorporating cationic, anionic, or ionizable lipids into LNP formulations can confer pH-responsive properties, enabling nanoparticles to dynamically adapt to changing environments.

2. Lipid Membrane Properties

From the perspective of lipid membrane packing status, different LNP phases exhibit distinct lipid membrane structures and properties. For instance, micelles form closed lipid monolayers, while liposomes (*La*) feature either classic bilayer membranes or densely packed multilayer membranes. Cubosomes (Q_{II}) consist of a single lipid bilayer arranged in a periodic lattice structure, whereas hexosomes (H_{II}) have a twisted, continuous lipid bilayer that forms an intricate network.

Lipid-membrane fluidity and lipid-water interfacial hydration status (polarity) are pivotal factors influencing the emergent functions of LNPs. Specifically, lipid-membrane fluidity is a fundamental physicochemical property of LNPs, reflecting the dynamics, micro-viscosity, and organization of lipids within the lipid membranes. This fluidity is crucial for determining the stability and functionality of LNPs, impacting both their *in vitro* and *in vivo* fates, which ultimately influences the therapeutic efficiency of encapsulated cargo molecules (Zhao, J. et al., 2020). Additionally, lipid-water interfacial polarity provides insight into how lipid molecules interact with their aqueous surroundings. Understanding this polarity helps in elucidating the packing and organization of lipid molecules in aqueous environments, as it is closely linked to LNP phase behavior.

While substantial researches have focused on elucidating the physicochemical properties of LNPs, particularly lamellar structures (liposomes), there remains a notable gap in the literature regarding the understanding of lipid-membrane properties in cubic and hexagonal mesophase LNPs. Most studies to date have primarily employed X-ray scattering and cryo-TEM methods to explore the structural and morphological changes of these mesophase LNPs in the presence of water (Larsson, K. et al., 2005). However, there has been less emphasis on probing the physicochemical behaviors of lipid membranes in these systems.

This study aims to address this gap by providing detailed insights into the variations in lipid-membrane physicochemical properties during the lamellar ($L\alpha$) to cubic (Q_{II}) phase transition. Utilizing fluorescence probes (Laurdan and DPH), this study monitored changes in lipid-water interfacial polarity and lipid-membrane fluidity throughout the phase transition process. This study's findings indicate that variations in lipid-membrane properties closely coincide with LNP lyotropic phase transitions, suggesting that these physicochemical changes are integral to the functionality of the LNPs. Additionally, Raman spectroscopy was employed as a label-free method to investigate lipid chain packing during the transition, offering information about the molecular organization within the lipid-membranes.

These combined methodologies enable us to observe the dynamic changes in lipid-membrane physicochemical behavior associated with phase transitions, contributing to a deeper understanding of the implications of lipid-membrane properties on the *in vitro* and *in vivo* fates of various phased LNPs. By elucidating the relationship between lipid phase behavior and membrane properties, this research provides essential insights that can inform the design of more effective lipid-based drug delivery systems.

3. Biophysical Properties of Cell Plasma Lipid Membranes

Cell membrane biophysical properties are critical for understanding the membrane's physical behavior, structure, and function. These properties are fundamental for maintaining cellular integrity, facilitating cell communication, and regulating the movement of substances into and out of the cell.

In living systems, the cellular plasma membrane exists as a complex three-dimensional assembly with diverse physical features that influence cell signaling and protein function. The natural formation of lamellar and non-lamellar lipid structures is essential for supporting various biological processes. For example, lamellar structures such as exosomes and extracellular vesicles (ECVs) secreted by cells play a pivotal role in intercellular communication by transporting biomolecules, including proteins, lipids, RNA (such as mRNA and miRNA), and other signaling molecules between cells. Additionally, mammalian cell and organelle membranes can transiently adopt cubic periodic structures to regulate osmolality or form hexagonal phases to facilitate calcium transport in muscle cells.

Similar to the LNP lipid-membrane properties investigations, this study specifically investigates the biophysical properties of the cellular plasma lipid membranes, focusing on two critical aspects: membrane lipid-water interfacial hydration status (polarity) and lipid packing status (fluidity). Interfacial polarity affects how the membrane interacts with water and various molecules, impacting membrane stability, permeability, and protein behavior. Lipid packing influences membrane fluidity and overall structural integrity. Tighter packing results in a more rigid membrane, while looser packing enhances fluidity, which can significantly affect cellular processes such as signaling, transport, and membrane fusion.

The study hypothesizes that different LNP formulations/lyotropic phases may alter cellular membrane polarity and lipid packing status. To test this hypothesis, Laurdan two-photon microscopy was employed to visualize and monitor changes in cell membrane polarity and fluidity, as well as to assess the impacts of LNPs on cell plasma membranes.

4. LNP Interactions with Cell Membranes

Effective drug delivery via LNPs depends on their successful internalization into target cells. Despite extensive research, the exact mechanisms underlying nanoparticle-mediated cargo delivery and the subsequent intracellular fate of therapeutic agents remain unclear. Optimizing these internalization pathways and intracellular trafficking processes is essential to enhancing the therapeutic efficacy of these drug delivery systems. Further exploration of functionalization strategies for LNPs is crucial for controlling their internalization and intracellular fate, ultimately improving therapeutic outcomes. As LNPs circulate and interact within the animal bodies, they frequently encounter cell plasma membranes, forming nano-bio interfaces. These interactions at the nano-bio interface significantly influence the physiological effects of LNPs. Therefore, understanding how LNP properties affect their interactions with cell membranes is vital for advancing their designs and functions.

LNPs interact with cell membranes through various mechanisms, including: endocytosis and phagocytosis; membrane adsorption, disruption and fusion. Among those mechanisms, endocytosis (**Fig. 1-3-A**) and membrane fusion (**Fig. 1-3-B**) are the most important mechanisms for LNPs internalization with cells. The most common uptake pathway for LNPs is endocytosis, where the cell membrane engulfs the LNP, leading to internalization into cells. This process can be mediated by clathrin, caveolae, or other non-specific pathways, depending on the physicochemical properties of the LNPs as well as cell lines. LNPs can adsorb onto the cell membrane surface due to electrostatic or hydrophobic interactions. Under specific conditions, LNPs may fuse with the membrane, allowing the cargo to enter the cell via direct membrane fusion. This mechanism is critical for delivering mRNA or proteins that must reach intracellular targets. LNPs with different lyotropic phases (micelles, liposomes, cubosomes, and hexosomes) exhibit distinct cellular uptake mechanisms due to their varied structural organization, surface properties, and size. Also, same LNPs may exhibit differed uptake mechanisms on different cell lines.

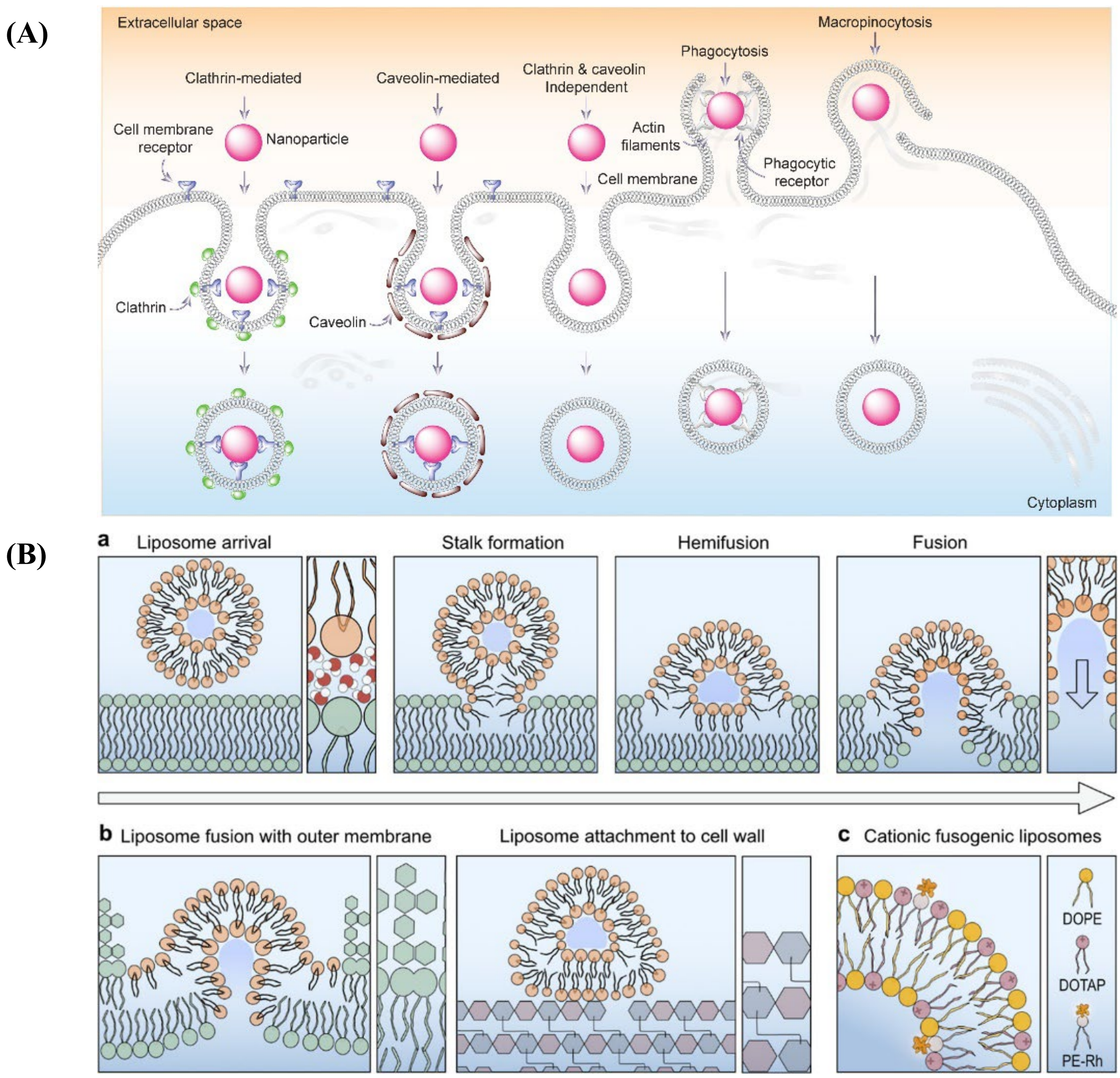

Figure 1-3. Interactions Between LNPs and Cell Membranes. (A) Endocytosis, phagocytosis and micropinocytosis pathways (Robin Augustine, 2020); **(B)** LNP fusion procedure with cellular membranes (Anna Scheeder, 2023).

Micelles are generally small (5-50 nm), allowing them to be efficiently taken up by cells via endocytosis (clathrin- or caveolae-mediated). Their small size and high surface curvature make micelles more prone to fast cellular uptake but also rapid clearance from the bloodstream. Also, the highly dynamic surface of micelles can facilitate direct fusion with the cell membrane, leading to payload release into the cytoplasm.

Cellular uptake mechanisms of liposomes are highly dependent on their formulation, morphology, and surface properties. Neutral liposomes are primarily internalized through endocytic pathways. Larger liposomes tend to be taken up via macropinocytosis, while smaller ones typically favor clathrin-mediated uptake. In addition, depending on the lipid composition (e.g., the presence of phosphatidylethanolamine (PE) or cationic lipids), liposomes can fuse directly with the cell membrane. PEGylated liposomes, which reduce protein adsorption and enhance circulation time due to the "stealth effect," often exhibit slower cellular uptake. Generally, factors such as size, surface charge, and PEGylation significantly influence liposome circulation time and cellular uptake efficiency.

Cubosomes may internalized by cells through both endocytosis and membrane fusion pathways, with uptake mechanisms shown to vary depending on the cell types. For example, cubosomes preferentially utilize membrane fusion pathways in fibroblast cells, whereas phagocytosis is the dominant pathway in macrophages (Strachan et al., 2020). This cell-type specificity highlights the versatility of cubosomes in interacting with different cellular environments.

Hexosomes typically utilize a membrane fusion-based cellular uptake mechanism. A study by Rodrigues et al. (2019) suggests that direct biomechanical interactions between hexosomes and cell membrane lipids are crucial, with their unique morphology playing a pivotal role in membrane activity. The authors proposed that hexosomes destabilize the lipid bilayer, allowing them to "phase through" the membrane. Furthermore, the lipid DOPE, characterized by its inverted-cone shape and low melting temperature (~30°C), is a key component in promoting membrane fusion. According to critical packing parameter (*CPP*) theory, DOPE lipids tend to adopt an inverted hexagonal (H_{II}) phase when incorporated into LNPs. This phase is known to destabilize endosomal membranes, facilitating efficient endosomal escape, a crucial step for successful intracellular delivery (Hou et al., 2021).

Table-1-2 summarized some reports about different LNPs cellular uptake mechanisms. The lipid composition of the cell membrane, membrane-water polarity, and membrane fluidity are particularly sensitive to interactions with LNPs. ER stress induced by specific fatty acids, LNP fusion with the cell membrane, and lipid exchange between LNPs and cell membranes can affect cell membrane fluidity and membrane-water interfacial polarity. Therefore, it is essential to develop methodologies and utilize specific tools to visualize and analyze these properties.

Table 1-2 Reported LNP Cellular Uptake Mechanisms

LNP phase	Material	Cell Line	Uptake Mechanism	Ref
Micelle	FA-BSP-SA	4T1	Endocytosis	Zhang et al., 2020
	C_{16}-S-S-mPEG and C_{16}-C-C-mPEG	HeLa	Endocytosis	Cui et al., 2013
	PEG-b-PLA polymeric micelles	A2780	Endocytosis	Zhang et al., 2012
Liposome (*La*)	DOPC: DOPG (87.5:12.5 mol%)	Hippocampal neurons	Clathrin-mediated endocytosis	Lakkaraju et al., 2002
	DMPC: DMPG (7:3 molar ratio)	HCAECs	Clathrin-mediated endocytosis	Zhaorigetu et al., 2014
	DOTAP: DOPC: DOPE: DC-cholesterol (1:1:1:1 molar ratio)	HeLa	Clathrin-mediated endocytosis	Digiacomo et al., 2017
	DOPC: chol (45:50, 50:45 and 95:5 molar ratio)	HeLa and HT-29	Clathrin-mediated endocytosis	Un et al., 2012
	DOPE: DOTAP (1:1 wt ratio)	CHO	Membrane fusion	Kube et al., 2017
	DSPE-PEG, DOPC, and DOTAP	HeLa	Membrane fusion	Kong et al., 2024
	DMPC: DSPE-PEG: DOTAP (76.2: 3.8: 20 molar ratio)	ARPE-19	Membrane fusion	Chen et al., 2021
Cubosome (Q_{II})	Monoolein	STO fibroblast stem cell	Membrane fusion	Strachan et al., 2020
		TIB-67	Phagocytosis	
	Monoolein	Hela	Membrane fusion	Rosa et al., 2015
	Monoolein	HeLa	Cholesterol-dependent fusion	Deshpande et al., 2017
	Monoolein + Poly-ε-lysine	HeLa	Endocytosis	
	Monoolein	HepG-2	Clathrin- and caveolae-mediated endocytosis	Abdel-Bar et al., 2017
Hexosome (H_{II})	Phytantriol	HeLa	Membrane fusion	Rodrigues et al., 2019

This study investigated LNPs’ direct and indirect interactions with cell membranes, focusing on LNPs’ lyotropic phase behavior, properties of the cellular plasma membrane, and mechanisms of LNP-cell membrane interactions. This approach aims to provide deeper insights into how LNP phase behavior influences their fate *in vitro* and *in vivo*.

5. Overview of this study

The purpose of this study is to characterize the physicochemical properties of LNPs with different lyotropic phase structures, understating their phase inter-changing behavior and their impacts on cellular plasma membranes. Basing on such knowledge, this study aims at optimizing the LNP formulations and customize the phase structures of LNPs for different purposes.

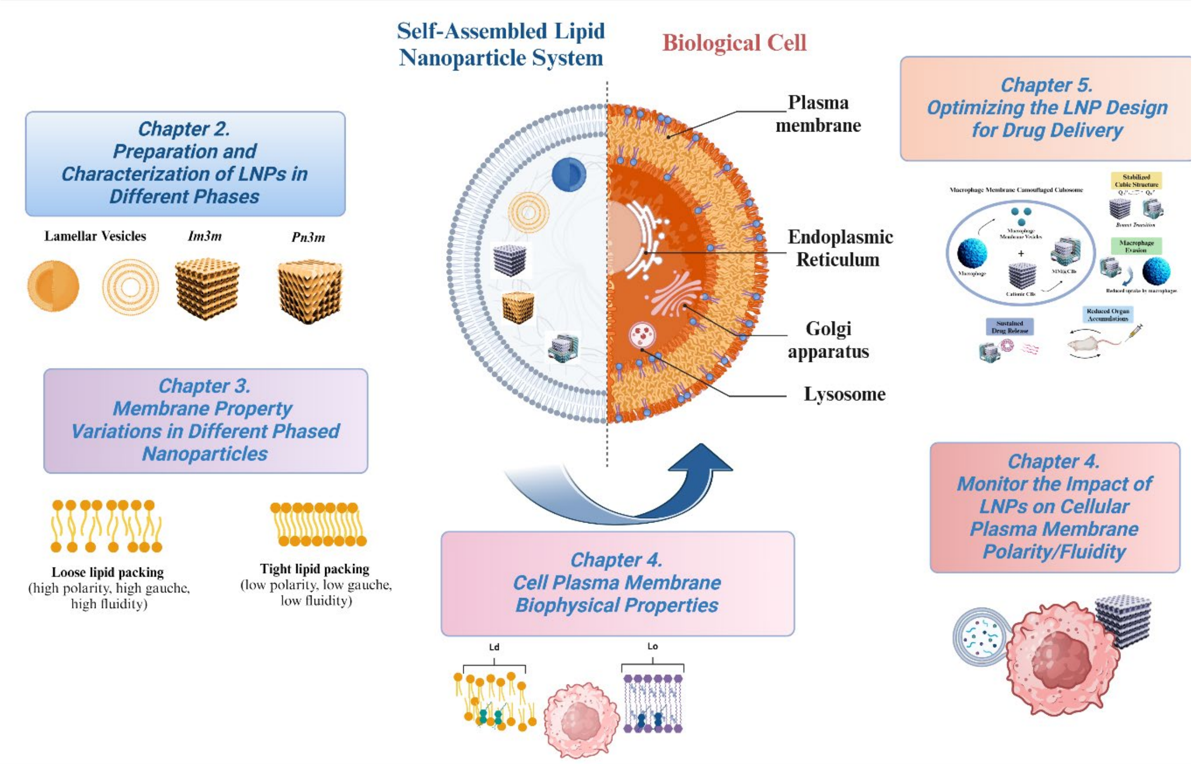

Figure 1-4. Concept of this Study

Chapter 2 focuses on the preparation and characterization of LNPs in various phases, presenting a comprehensive study of their phase behavior using techniques such as small-angle X-ray scattering (SAXS), dynamic light scattering (DLS), and cryo-TEM. Representative SAXS patterns are shown for different LNP lyotropic phases, including lamellar vesicles ($L\alpha$) and cubic phase nanoparticles (*Im3m* and *Pn3m*). Specifically, pH-triggered phase transitions in 2-hydroxyoleic acid/monoolein (2-OHOA/MO) nano-dispersions, shifting from liposomes (La) to cubosomes (Q_{II}), are confirmed through SAXS measurements at different pH levels.

These transitions are further correlated with changes in particle size and surface charge. Cryo-TEM images provide additional validation of the internal structures. The results underscore that LNP phase behavior is strongly influenced by lipid composition, pH, and molecular packing parameters.

Chapter 3 investigates the properties of lipid membranes across different LNP phases, characterized using fluorescence probes such as Laurdan and DPH (1,6-Diphenyl-1,3,5-hexatriene), as well as Raman spectroscopy. Laurdan is a hydrophobic solvatochromic fluorescent probe commonly used to detect the hydration status (polarity) at the lipid membrane-water interface. The fluorescence anisotropy of DPH provides a measure of lipid membrane fluidity, while Raman spectroscopy offers a label-free method for detecting and quantifying lipid membrane viscosity, specifically examining C–C and C–H bond stretching and vibration. In this chapter, 2-OHOA/MO binary component nano-dispersion system was used as a model to study lipid membrane behavior during pH-triggered lamellar to cubic phase transition. The results offer insights into changes in lipid packing status, membrane-water interfacial hydration status, and phase transitions. This study underscores the potential to track LNP lipid membrane physicochemical properties in tandem with LNP phase behavior, paving the way for the development of phase-engineered drug delivery systems with enhanced drug loading efficiency and controlled release profiles.

Chapter 4 examines the hydration status (polarity) of the cell plasma membrane using Laurdan two-photon microscopy (TPM). These findings were complemented by LipiORDER fluorescence microscopy results, which assess cell membrane fluidity. The study reveals that different cell types exhibit distinct lipid membrane fluidity/polarity patterns. Additionally, the high resolution of TPM enables the visualization of heterogeneity in membrane fluidity and polarity. Basing on this methodology, this study further investigated how the LNPs modulates the biophysical properties of cell plasma membranes. This study was extended to explore the LNP internalization mechanisms, which would influence cell membrane characteristics directly or indirectly.

Chapter 5 introduces a strategy for stabilizing cubic-phase lyotropic liquid crystalline nanoparticles (Cubosomes, CBs) by camouflaged them with macrophage cell membranes, instead of the conventional PEGylation or block polymer coating method. The goal of this approach is to improve the immune escape capabilities of cubosomes while maintaining their structural integrity and functionality. The prepared bio-memetic nano-DDS was systematically characterized using SAXS, TEM, cryo-TEM and DLS *et al*. The macrophage evasion performance, biodistribution and anticancer performance were analyzed as well. This strategy shows promise in improving the stabilities and macrophage evasion performance of CB-based nanomedicine delivery systems. Furthermore, future engineering of the membrane source cells for the membrane coating could probably enhance cancer-targeting capabilities, opening new avenues for more precise and effective drug delivery platforms.

Chapter 6 presents the overall conclusions of this work. The findings advance our understanding of LNP characteristics, focusing on lipid shape, membrane packing properties, ionization status of lipids and the morphologies/phases of resulting lipid assemblies. Building on the study and control of LNP phase behaviors, this research further explores how LNPs interact with cellular plasma membranes, offering potential insights for optimizing LNPs to enhance drug delivery performance.

Chapter 2

Preparation and Characterization of Lipid Nanoparticles in Different Phases

1. Introduction

This chapter focuses on the preparation and characterization of lipid nanoparticles in different phases. Several factors would impact the lyotropic phases of the lipid self-assemblies. Those factors including lipid composition (type of lipids, saturation degree and lipid ratios etc.), preparation method (thin film hydration, ethanol injection, microfluidics etc.), hydration level, temperature, pH and ionic strength etc. Typically, the LNPs prepared using phospholipid via thing-film hydration method exhibits lamellar (*La*) vesicle structure. On the other hand, the preparation of cubic (Q_{II}) phased LNPs mainly based on monoolein (MO) or phytantriol (PYT). The top-down method is one of the commonly used techniques for preparing cubic phased LNPs. In this approach, a bulk cubic liquid crystalline phase (formed from MO or PYT in water) is physically fragmented into nanoparticles using mechanical forces (ultra-sonification or high-pressure homogenization). Techniques such as small-angle X-ray scattering (SAXS), transmission electron microscopy (TEM), and cryo-TEM were employed to comprehensively analyze LNP phase status and morphologies. Key parameters of the LNPs across various phases were calculated and compared.

SAXS is a powerful analytical technique that plays a crucial role in characterizing LNPs at the nanometer and sub-nanometer scale. It provides detailed insights into the internal structures of LNPs, including their sizes, shapes, and inner structure organizations, without requiring crystallization or extensive preparation. SAXS is particularly useful for understanding the arrangement of lipids within nanoparticles, revealing essential details about their mesophases, including lamellar (*La*), cubic (Q_{II}) and hexagonal (H_{II}) phases. SAXS is often used to determine the lattice parameters of ordered internal structures in LNPs, such as cubosomes and hexosomes. These phases exhibit unique SAXS scattering patterns, allowing researchers to map out the internal arrangement of lipid molecules. Furthermore, SAXS can measure structural parameters like the thickness of lipid bilayers in liposomes, the periodicity of multilamellar vesicles (MLVs), the lattice parameter (a) and water channel radius (r_w) of cubosomes and hexosomes. This quantitative information is essential for assessing the uniformity and stability of LNPs. One of the significant advantages of SAXS is its non-destructive nature, enabling the study of LNPs in their native hydrated state without altering their structures. The technique is highly sensitive to nanoscale features and can monitor how the internal structure of LNPs changes in response to environmental conditions such as temperature, pH, or the incorporation of drugs or targeting ligands. This capability is critical for understanding stimuli-responsive LNP phase behaviors for further optimizing LNP formulations for specific therapeutic applications. Overall, SAXS is an indispensable tool for the detailed characterization of LNPs, helping researchers understand LNP structures and fine-tune the design of LNPs.

Cryo-transmission electron microscopy (cryo-TEM) is a vital technique for the high-resolution visualization of LNPs, allowing researchers to study their structures in a near-native, hydrated state. This method differs from conventional TEM by eliminating the need for staining or extensive sample preparation, which can alter the structural integrity of delicate biological materials including lipid-based drug delivery systems. By freezing the LNPs rapidly, cryo-TEM preserves their morphology and internal organization, providing accurate insights into their size, shape, and detailed arrangement at the nanometer scale. Those properties make cryo-TEM an essential tool for visualizing the morphologies and inner structures of LNPs.

In this chapter, LNPs with different phases were prepared using thin-film hydration or ultrasonication methods. The characteristic scattering patterns of lamellar vesicles (unilamellar or multilamellar) and cubic phase nanoparticles (*Im3m* or *Pn3m* space groups) were demonstrated. Based on these findings, this study developed and characterized a 2-OHOA/MO binary component LNPs, which exhibited a pH-triggered transition from a lamellar (L_a) to a cubic (Q_{II}) phase.

2. Materials and Methods

2.1. Materials

Phospholipids (DOPC, DOTAP) and 2-hydroxyoleic acid (2-OHOA, >99%) were purchased from Avanti Polar Lipids (Alabaster, AL. USA). Monoolein (≥99%,1-Oleoyl-rac-glycerol), Pluronic F127 (Poly (ethylene oxide)-poly-(propylene oxide)-poly (ethylene oxide)), 1,6-Diphenyl-1,3,5-hexatriene (DPH, >98%) and Dodecanoyl-2-Dimethylaminonaphthalene (Laurdan, >97%) were purchased from Sigma-Aldrich. Sodium hydroxide (NaOH, ≥97.0%), hydrochloric acid (HCl, 35.0~37.0%), chloroform (≥99.0%) and methanol (≥99.8%) were purchased from Wako Pure Chemical Industries.

2.2. Preparation of Liposome via Thing-Film Hydration Method

Liposomes were prepared using the thin-film hydration-extrusion method. In brief, DOPC and 2-OHOA were first dissolved in chloroform and mixed in varying ratios in 100 mL round-bottom flasks. These lipid solutions underwent vacuum evaporation at 60 ℃, followed by maintenance under high vacuum conditions at room temperature for 24 h. Following the vacuum step, D-PBS was added to the flasks to hydrate lipid films. The resulting vesicle suspensions were subjected to 4 cycles of freezing at –80 ℃ and thawing at 65 ℃. After the freeze-thaw process, the suspensions were extruded 13 times through a polycarbonate membrane with an average pore diameter of 200 nm, using an extruder (LiposoFast LF-1, Avestin, Canada). The DOPC:2-OHOA ratios were set at 10:0, 9:1, 7:3, 5:5, 3:7, 1:9, and 0:10 (molar ratios). For brevity, liposomes fabricated from different formulations and 2-OHOA-only particles were named as follows: DOPC-only liposomes, 9-1 liposomes, 7-3 liposomes, 5-5 liposomes, 3-7 liposomes, 1-9 liposomes, and 2-OHOA-only particles. To investigate the cellular internalization efficiency and uptake mechanism, 1 mol% 16:0 NBD-PE was incorporated into the liposome formulations before the vacuum-evaporation step.

2.3. Preparation of 2-OHOA/MO Nano Assembles via Ultra-sonification Method

MO, 2-OHOA and DOTAP were dissolved in chloroform as stock solutions. MO with or without 2-OHOA or DOPTA were added in Eppendorf tubes at predetermined amount. The solutions were then vacuumed for 48 hr to remove the organic solvent. The dried samples were then heated at 70 °C and hydrated using a preheated Pluronic F127 solution (2 mg/mL). The final concentrations of amphiphiles (MO + 2-OHOA or DOTAP) were 56.1 mM and the final Pluronic F127 concentration was 2 mg/mL. The 2-OHOA-only dispersion was prepared using same procedure, the final 2-OHOA concentration was 56.1 mM containing 2 mg/mL Pluronic F127. The resulting mixtures were vortexed for 10 mins and exposed to probe-style ultrasonication (Ultrasonic Disruptor, UD-200, TOMY, Japan) on ice for 20 mins at 100 W.

2.4. Small-Angle X-ray Scattering (SAXS) Investigation

SAXS investigation was carried out in Spring-8 (Super Photon ring-8 GeV radiation faculty). The leveraged beamline was BL19B2. Trial experiments were firstly carried out to confirm the optimized experiment conditions. Each sample was analyzed with 300s scattering exposure time. The detector was PILATUS-2M (two-dimensional pixel detector, camera length is 3 m). The beam energy was set at 18 keV; X-ray wavelength (λ) was about 0.69 [Å], q value detection range was set from 0.06 to 3 nm^{-1} and the sample-to-detector distance was calibrated using silver behenate. All measurements were carried out at 25 °C.

The lattice parameters were calculated using **Eq. (2-1)** and the interlamellar distance of the multilamellar vesicles' (MLV) bilayer stacks (d-space) was calculated according to **Eq. (2-2)** (Kulkarni, C *et.al.*, 2011).

$$a_{Im3m/Pn3m} = \frac{2\pi}{q} \times \sqrt{h^2 + k^2 + l^2} \qquad Eq.(2-1)$$

Where, $a_{Im3m/Pn3m}$ is the lattice parameter of *Im3m* space group and *Pn3m* space group structures; $h,\ k,\ l$ are the Miller indices $[h,\ k,\ l]$.

$$d = \frac{2\pi h}{q_h} \qquad Eq.(2-2)$$

where h is the order of the Bragg peak, and q_h is the q-value of the h-th order Bragg peak.

The water channel radius (r_w) was calculated according to **Eq. (2-3)** and **Eq. (2-4)**:

For *Im3m* phase:

$$r_w = 0.306 * a - l \qquad Eq.(2-3)$$

For *Pn3m* phase:

$$r_w = 0.391 * a - l \qquad Eq.(2-4)$$

Here, a is the lattice parameter, l is the length of MO hydrophobic chain.

l is calculated according to the equation: $l = 1.8e^{(-0.0019T)}$ (Mazzoni *et.al.*, 2016). *T* and *l* have units of °C and nm, respectively. At 25 °C, the l is calculated to be 1.7 nm.

2.5. Cryogenic transmission electron microscopy (cryo-TEM) and TEM

Morphological characterization of different particles was performed using cryo-TEM. Specimen were prepared using Vitrobot mark IV (Thermo/FEI, USA). 2.4 µL of the sample was deposited onto freshly glow discharged (10 mA for 20 s) Cu QUANTIFOIL grids (R1.2/1.3, 300 mesh). The carbon-coated grids were blotted with sample for 3 s (blotting force of 7 at 25°C under 100% relative humidity) before being plunged into liquid ethane. Samples were imaged using a Titan KRIOS microscope (Thermo Fisher Scientific, USA) with an accelerating voltage of 300 kV and a defocus value of −4 µm at a magnification of 59000 which has a pixel size of 0.14 nm or 7500 times magnification with a pixel size of 1.1 nm. Image processing and analysis were performed using ImageJ (Version 1.53t).

2.6. Particle size & ζ-potential characterization

Hydrodynamic particle size, polydispersity index (PDI), and ζ-potential were investigated using a Zetasizer (ZEN5600, Malvern, UK). Various LNP suspensions were diluted to a final concentration of 100 µM before measurements. These measurements were conducted in triplicate at a temperature of 25 °C.

2.7. Estimation of apparent p*Ka* of 2-OHOA

The pH-ζ-potential function was fitted using Sigmoidal-Boltzmann equation (Prajapati, R et al., 2019):

$$\zeta(pH) = \frac{\zeta_1 - \zeta_2}{1 + 10^{(pKa - pH)}} + \zeta_2 \qquad Eq.(2-5)$$

In this equation ζ(pH) is the ζ-potential at a given pH; ζ_1 and ζ_2 are the asymptotic zeta potentials at low and high pH, respectively; p*Ka* is the dissociation constant. In this study, the estimated apparent p*Ka* values were 5.05 ± 0.19, 5.32 ± 0.66 and 4.43 ± 0.72 for 5, 7.5 and 10 mol% 2-OHOA/MO nano-dispersions respectively.

2.8. Critical packing parameter (*CPP*)

The *CPP* can be calculated by the following equation (J. N. Israelachvili. Et al., 1976):

$$CPP = \frac{v}{a_0 l_c} \qquad Eq.(2-6)$$

In this equation, v is the effective hydrophobic chain volume, a_0 is the effective headgroup area at the interface, and l_c is the length of the hydrophobic tail.

Typically, when 1/2 < *CPP* < 1: The molecules tend to form lamellar vesicles (unilamellar or multilamellar); when *CPP* ≈ 1, the amphiphiles form a typical planner lamellar structure; when *CPP* > 1, the amphiphiles tend to form inverted structures, such as cubic phases (*Im3m/Pn3m*). In this study, the *CPP* of prepared nano-dispersions follows the trend: $CPP_{(\mathrm{ULV})} < CPP_{(\mathrm{MLV})} < CPP_{(Im3m)} < CPP_{(Pn3m)}$. (Sarkar, S. et al., 2018).

3. Results and Discussion

3.1. Representative SAXS Patterns of LNPs of Different Lyotropic Phases

For the purpose of characterizing the lyotropic phase structure of LNPs, a SAXS investigation was conducted. **Fig 2-1** summarized some representative SAXS patterns of prepared LNPs. Typically, the DOPC liposome (**Fig 2-1-A**) exhibits lamellar vesicle (*La*) structure with low stacking of lamellar layers, indicating a coexistence of unilamellar vesicles (ULVs) and muitilamellar vesicles (MLVs) with low stack. While the doping of 2-OHOA (10 mol%) induced a drastic reduction of stack of lamellar layers, resulting in a diffused scattering pattern (**Fig 2-1-B**), characterized a dominating ULV structures. Additionally, the peak appears at q ~ 1.4 nm^{-1} indicated an existence of trace amount of swollen MLVs with low stacks. Meanwhile, the 2-OHOA-only dispersion (**Fig. 2-1-C**) showed Bragg peaks at q values of about 1.57 nm^{-1} and 3.14 nm^{-1}, characterizing a typical MLVs with an interlamellar d-spacing of about 4.00 nm. Also, the peak appeared at lower q value region (1.44 nm^{-1}) indicated the formation of swollen MLV structure (low stack).

MO was utilized for preparing the cubic structures lyotropic liquid crystalline (Cubsomes, CBs) via ultra-sonification method. MO-based CBs could have different cubic phases, including primitive cubic phase (*Im3m*, Q_{II}^{P}), diamond cubic phase (*Pn3m*, Q_{II}^{D}) and gyroid cubic phase (*Ia3d*, Q_{II}^{G}). As shown in **Fig 2-1-D**, the SAXS patterns of MO-only CBs displayed prominent peaks at ~0.681, 0.965, and 1.176 nm^{-1}. On the other hand, the SAXS pattern of cationic CBs exhibited prominent peaks at ~0.615, 0.870, and 1.074 nm^{-1}. Both MO-only CB and cationic CBs SAXS patterns exhibited distinct Bragg peaks at the space ratio of $\sqrt{2}$: $\sqrt{4}$: $\sqrt{6}$, corresponding to Miller indices [h, k, l]: [1, 1, 0], [2, 0, 0], and [2, 1, 1], respectively. These patterns are indicative of a primitive cubic phase (Q_{II}^{P}), belonging to the space group *Im3m.* The lattice parameters (a) of the MO-only CBs and cationic CBs were measured to be 13.05 nm and 14.46 nm, respectively. The doping of the DOTAP cationic lipid resulted in a slight increase of lattice parameter (a). However, the internal Q_{II}^{P} nanostructure was retained, which is consistent to the previous reported results that the interplay between charge repulsion of the lipid membrane interfaces induced larger water channels in CBs, **Table 2-1** summarized calculated phase lattice parameters of different LNPs.

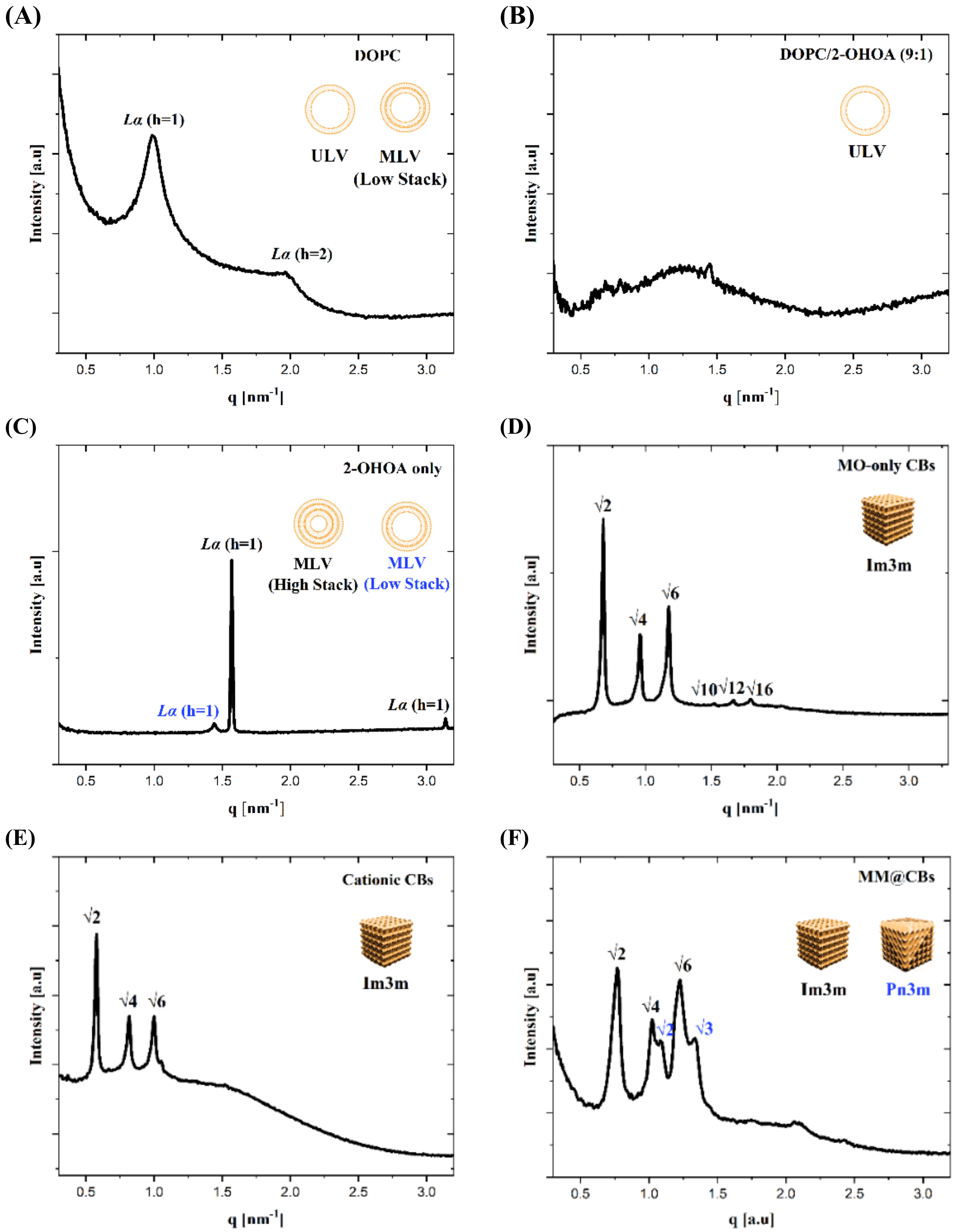

Figure 2-1. Representative SAXS Patterns of Different Prepared LNPs. (A) DOPC lamellar vesicles (unilamellar and low stacked mutilamellar); **(B)** DOPC + 10 mol% 2-OHOA lamellar vesicles (unilamellar); **(C)** 2-OHOA only vesilces (high stacked mutilamellar); **(D)** MO-only cubosomes (*Im3m* space group); **(E)** MO+1 mol% DOTAP (*Im3m* space group); **(F)** Macrophage membrane camouflagged cubosomes (*Im3m* and *Pn3m* space group).

For sample **A** and **B**, concentration was set at 20 mM; for sample **C-E**, concentratuion was 56 mM; for sample **F**, concentration was 28 mM. Measurements were carried out at 25 °C.

Table 2-1 Calculated Phase Lattice Parameters of Different LNPs

Name	Formulation	Lattice Parameter (*a*/*d*) [nm]	Water Channel radius (r_w) [nm]	Structure
MO-only CBs	MO	13.05	2.72	Q_{II}^P
Cationic CBs	MO+ 1 mol% DOTAP	14.46	2.29	Q_{II}^P
DOPC only Liposome	DOPC	6.28	-	*Lα*
DOPC/2-OHOA (9-1)	DOPC + 10 mol% 2-OHOA	4.48	-	*Lα*
2-OHOA only	2-OHOA	4.00	-	*Lα*

3.2. pH-Triggered Phase Changing of 2-OHOA/MO Nano-dispersion

2-OHOA is an oleic acid (OA) derivative with an additional hydroxyl group on the *α*-carbon of the fatty acid backbone (Alemany et al., 2004). The 2-OHOA/MO binary component nano-dispersions have been reported to exhibit pH-triggered phase transition behavior, similar to the OA/MO dispersion system (Prajapati et al., 2019). The additional hydroxyl group gives 2-OHOA a lower p*K*a (~5.6) compared to OA (~7.0) (Barceló et al., 2004). At physiological pH (~7.4), the net negative charge of 2-OHOA induces strong electrostatic repulsion between lipid membrane interfaces, significantly impacting the lipid membrane packing state. In this study, 2-OHOA/MO nano-dispersions with varying 2-OHOA ratios (5, 7.5, and 10 mol%) were prepared to investigate changes in lipid membrane physicochemical properties during the pH-triggered lyotropic phase transition.

To confirm the lyotropic phase changes in 2-OHOA/MO nano-dispersions, this study prepared samples at various ratios and adjusted the pH to 7.4, 4.5, and 3.0. These dispersions were stabilized for 24 hours and then characterized using SAXS. **Fig. 2-2** presents the SAXS patterns of the dispersions under different pH conditions. Key parameters for the lamellar (*Lα*) and cubic (Q_{II}) phases, including lattice parameters (a_0) and water channel radii (r_w), were calculated and summarized in **Table 2-2**.

At pH 7.4, the MO-only dispersions (**Fig. 1-A**, upper raw) showed distinct Bragg peaks at 0.61, 0.87 and 1.07 nm^{-1}, with position ratios of $\sqrt{2}$: $\sqrt{4}$: $\sqrt{6}$, corresponding to Miller indices [*h, k, l*]: [1, 1, 0], [2, 0, 0], and [2, 1, 1], characterizing a typical *Im3m* cubic phase structure with a lattice parameter (α) of 14.47 nm.

In 2-OHOA/MO binary nano-dispersions, decreasing pH typically induced phase transitions in the sequence of lamellar phase vesicles (*Lα*) → cubosomes (*Im3m/Pn3m*). At pH 7.4, even a low 2-OHOA content (5 mol% relative to MO) exhibited diffuse-dominant scattering patterns (**Fig. 2-2-A**). Based on previous studies, the diffuse-dominant scattering at pH 7.4 suggests the formation of ULVs rather than MLVs nor cubosomes.

At pH 4.5, a subtle structural transition was observed in the 5 mol% 2-OHOA/MO formulation, with a peak at 0.301 nm^{-1} (marked with a red asterisk) possibly indicating a cubic phase with a high lattice parameter. However, the peak positions did not align with the typical *Im3m* or *Pn3m* cubic structures, possibly due to overlapping of other Bragg peaks with diffuse scattering peaks. Following the *Lα* → *Im3m* → *Pn3m* transition sequence, this structure (at pH 4.5) is likely an *Im3m* cubic phase. Despite the overlap and diffusion of Bragg peaks, broad correlation peaks in the 0.5–1.0 nm^{-1} range could still be observed, likely due to weak bilayer correlations in coexisting ULVs and MLVs.

When pH was reduced to 3.0, both the 5 mol% (**Fig. 2-2-A**, lower row) and 7.5 mol% (**Fig. 2-2-B**, lower row) 2-OHOA/MO dispersions displayed clear Bragg peaks in the ratio of $\sqrt{2}$: $\sqrt{4}$: $\sqrt{6}$, characteristic of an Im3m cubic phase. However, in the 10 mol% 2-OHOA/MO dispersion, a coexistence of *Im3m* and *Pn3m* phases was observed (**Fig. 2-2-C**, lower row). The lattice parameter ratio (*aIm3m*/*aPn3m*) was calculated as 1.33, close to the theoretical Bonnet ratio of 1.27.

According to critical packing parameter (*CPP*) theory (discussed in **Chapter 1**), the lipid-water interfacial curvature of self-assemblies is governed by the lipid molecular shape, described by the *CPP*. For typical *Lα* phase vesicles, the *CPP* value is approximately 0.5–1, whereas for cubic phases, the *CPP* exceeds 1. Additionally, the *Pn3m* cubic phase has greater negative interfacial curvature than that of *Im3m* cubic phase (higher negative membrane curvature), leading to the phase transition sequence to follow increasing negative curvature as

Lα→Im3m→Pn3m. The coexistence of *Im3m* and *Pn3m* phases in the 10 mol% 2-OHOA formulation at pH 3.0 suggests that a higher 2-OHOA content induces greater negative curvature in the lipid membrane, causing part of the *Im3m* phase to transition to the *Pn3m* phase.

Previous research (H. Yu et al., 2024) has shown that the phase behavior of pH-responsive nano-dispersions is primarily determined by lipid composition, with the stabilizer exerting minimal impact on inner membrane curvature. This is because Pluronic F127 primarily adsorbs and incorporates on the cubic nanoparticle surface, preserving the internal structure (Tilley et al., 2013). While Pluronic F127 concentration can influence membrane curvature in cubosomes and affect colloidal assembly formation (Salentinig et al., 2010), all nano-dispersion formulations in this study contained the same F127 concentration (2 mg/mL). During pH reduction, the SAXS patterns of the 5 mol% 2-OHOA/MO dispersions showed more pronounced changes than those of the 10 mol% formulation, indicating that nano-dispersion composition is a key factor in determining membrane curvature and phase transitions. The SAXS results align well with *CPP* theory predictions and prior studies.

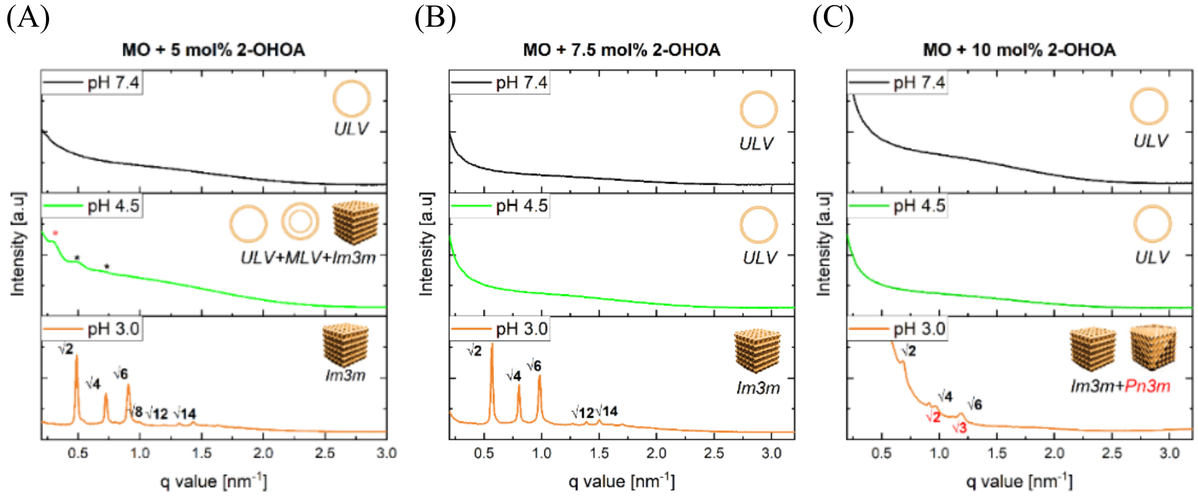

Figure 2-2. The One-Dimensional SAXS Patterns of 2-OHOA/MO Nano-Dispersions at Different pHs. SAXS patterns of (A) MO containing 5 mol% 2-OHOA, at pH 7.4, 4.5 and 3.0. (B) MO containing 7.5 mol% 2-OHOA, at pH 7.4, 4.5 and 3.0. (C) MO containing 10 mol% 2-OHOA, at pH 7.4, 4.5 and 3.0. The final concentration of dispersions was 50 mM (calculated according to MO+2-OHOA amount). All measurements were conducted at 25 °C. For 5 mol% 2-OHOA formulation at pH 4.5, the low intensity peaks potentially derived from MLVs are marked with black asterisks; the peak potentially derived from *Im3m* phase is marked with red asterisk. For the cubic structures, the Bragg peak spacing ratios identifying *Im3m* and *Pn3m* space group are represented in black and red, respectively.

Table 2-2. Calculated phase lattice parameters of different nano-dispersions

Formulation	pH	Lattice Parameter (*a*/*d*) [nm]	Water Channel radius (r_w) [nm]	Structure
MO-only	7.4	14.47	2.73	*Im3m*
2-OHOA-only	7.4	4.00	-	*Lα*
MO+5 mol% 2-OHOA	7.4	-	-	-
	4.5	20.86/12.61	4.68/-	*Im3m/Lα*
	3.0	18.11	3.84	*Im3m*
MO+7.5 mol% 2-OHOA	7.4	-	-	-
	4.5	-	-	-
	3.0	15.56	3.06	*Im3m*
MO+10 mol% 2-OHOA	7.4	-	-	-
	4.5	-	-	-
	3.0	13.06/9.80	2.29/2.13	*Im3m/Pn3m*

Based on the findings above, this study hypothesized that the pH-triggered phase transition in 2-OHOA/MO nano-dispersions would result in a pH-dependent drug release profile in the prepared pH-sensitive formulations. To test this, 0.5 mol% doxorubicin (DOX) was incorporated into 2-OHOA/MO LNPs, and their drug release behavior was monitored under varying pH conditions. As shown in **Fig. 2-3**, all LNP formulations exhibited similar DOX release profiles at neutral pH (7.4). However, as pH decreased, a significant increase in DOX release rate was observed across all formulations. This suggests that the pH-triggered transition from the lamellar (*Lα*) phase to the cubic phase is crucial for enhancing DOX release from the LNPs. Mechanistically, the transition from the *Lα* phase to the cubic (*Im3m/Pn3m*) phase involves a reorganization of vesicular water pools into the more intricate water channel structures characteristic of the cubic phase. This structural rearrangement likely expels the encapsulated DOX, accelerating the release rate.

This behavior is especially relevant in the context of the tumor microenvironment, which is typically more acidic than normal physiological conditions. The ability of these LNPs to release their payload more efficiently under acidic conditions suggests enhanced tumor-targeting potential. This feature could improve the therapeutic efficacy of DOX by concentrating its release within tumor tissues, while minimizing off-target effects in healthy tissues where the pH remains neutral.

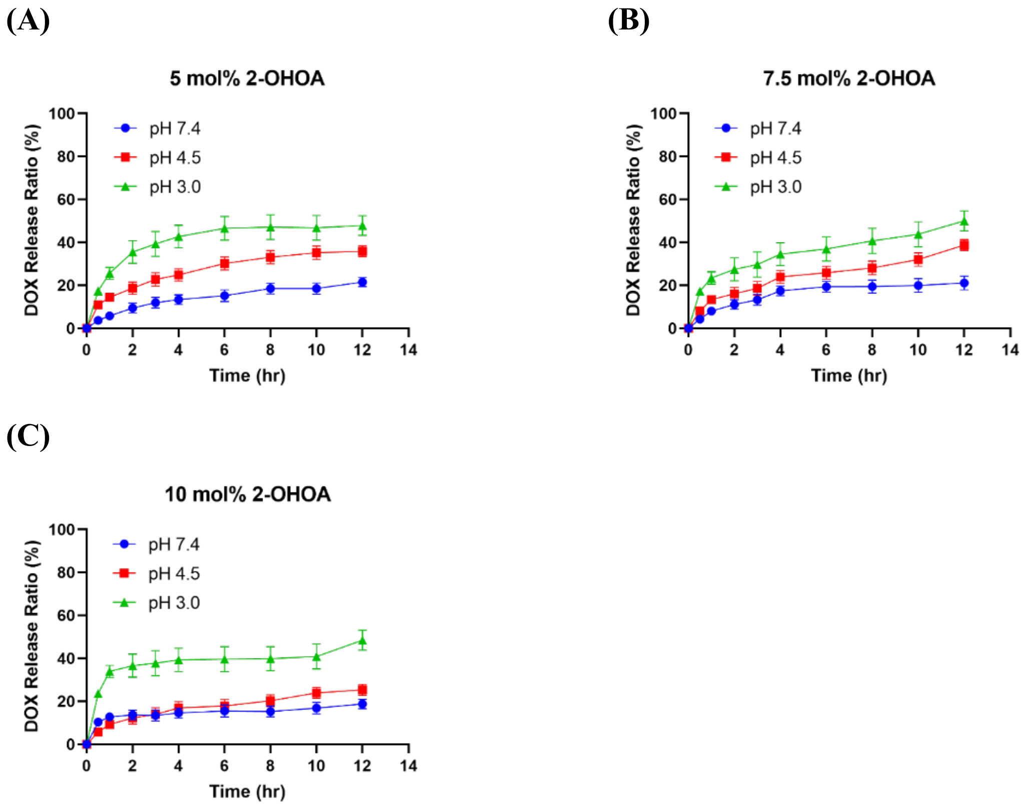

Fig 2-3. DOX Release Patterns at Different pH Conditions. (A) 5 mol% 2-OHOA; **(B)** 7.5 mol% 2-OHOA; **(C)** 10 mol% 2-OHOA. LNP concentrations were set at 50 mM, containing 0.5 mol% DOX, the drug release were monitored for 12 hr at 25 °C.

While these findings are promising, several additional factors must be addressed to translate this system successfully into clinical applications. The *in vivo* stability of the LNPs is crucial, as premature phase transitions or drug release in the bloodstream could reduce therapeutic efficacy and increase systemic toxicity. Important considerations include serum stability, circulation time, and the ability of the LNPs to reach tumor sites intact. Additionally, optimizing the lipid composition to fine-tune release kinetics at specific pH thresholds could further enhance the precision of this delivery system. Overall, these pH-sensitive 2-OHOA/MO LNPs show promise for targeted cancer therapy, but further investigation, particularly through *in vivo* studies, is necessary to fully evaluate their therapeutic potential and safety.

3.3. DOPC Liposome Phase Changing Induced by 2-OHOA Doping

As discussed in **Section 3.2**, incorporating 2-OHOA into MO dispersions led to significant lyotropic phase changes at neutral pH (7.4) compared to MO-only dispersions. Upon lowering the pH, SAXS characterization revealed a phase transition from lamellar ($L\alpha$) to cubic (*Im3m/Pn3m*) structures. This phase transition is primarily driven by two factors: the critical packing parameter (*CPP*) of the amphiphiles and the acid dissociation constant (p*K*a) of the ionizable amphiphiles within the LNP formulations.

In clinical LNP research, phospholipids like DOPC, DSPC, and DOPE are commonly used as "helper lipids." Compared to MO, these phospholipids have significantly lower *CPP* values, both experimentally and thermodynamically, as shown in **Table 1-1**. To assess the impact of 2-OHOA on phospholipid-based systems, this study formulated a series of DOPC/2-OHOA binary LNPs at varying molar ratios and evaluated their phase structures at neutral pH (7.4). The SAXS patterns of these formulations are presented in **Fig. 2-5**.

LNPs composed solely of DOPC displayed a characteristic two-peak SAXS pattern, with Bragg peaks at 0.994 and 1.985 nm^{-1}. These peaks, following a $\sqrt{1}$: $\sqrt{4}$ ratio and corresponding to Miller indices [h, k, l]: [1, 0, 0] and [2, 0, 0], indicate a lamellar ($L\alpha$) phase with low-stacked MLV structures. Adding 10–50 mol% of 2-OHOA to DOPC introduced a diffused scattering pattern, suggesting the formation of ULVs typical of the $L\alpha$ phase. The addition of 2-OHOA also promoted loosely stacked MLV structures, evidenced by a Bragg peak at ~1.45 nm^{-1}.

The behavior of 2-OHOA in DOPC-based systems mirrors its effect in MO-based formulations. At neutral pH (7.4), the high negative charge of 2-OHOA induces strong electrostatic repulsion between adjacent lipid membranes, preventing tight membrane stacking and favoring ULV formation. This underscores 2-OHOA's role in modulating membrane architecture and phase behavior, shifting lipid systems from MLV to ULV structures by altering the electrostatic landscape. 2-OHOA's ability to drive phase transitions through electrostatic interactions is especially relevant for designing pH-sensitive drug delivery systems. The observed shift from stacked MLV to ULV or cubic structures under different conditions suggests that 2-OHOA-modified LNPs could be engineered for pH-responsive cargo release in environments like tumor tissues. This potential for controlled drug release highlights the importance of further optimizing lipid composition and *CPP* to fine-tune phase behavior for specific therapeutic applications.

Overall, these findings reinforce 2-OHOA's versatility as a functional lipid component that can drive phase transitions in LNP systems, enhancing their potential for targeted drug delivery and controlled release across diverse physiological environments.

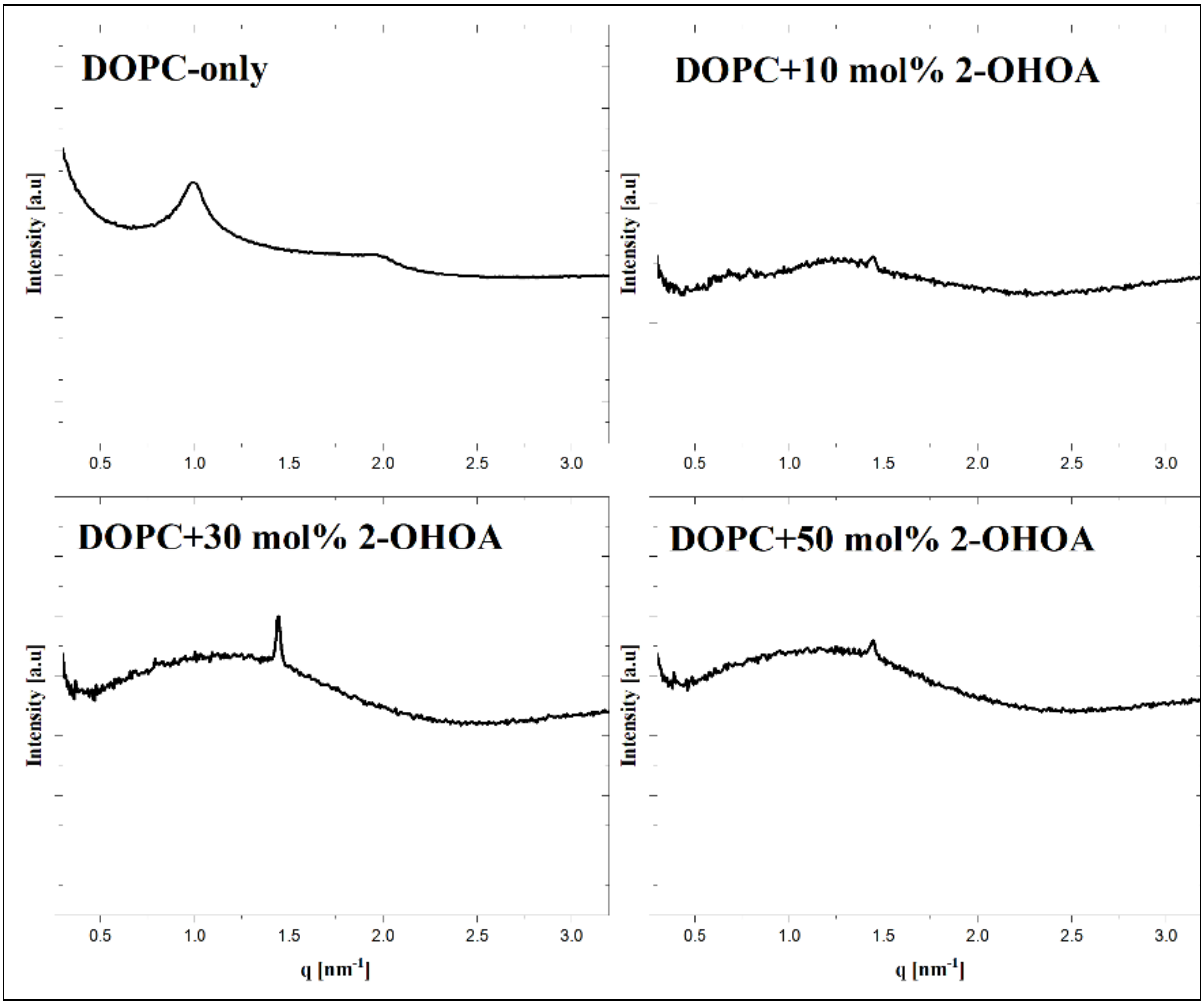

Figure 2-4. SAXS Patterns of DOPC-only and DOPC/2-OHOA LNPs. The liposomes prepared via thing-film hydration method as described in Material and Experimental section. The lipid concentrations were set at 20 mM. All measurements were conducted at 25 °C.

3.4. Dynamic Light Scattering (DLS) and ζ-Potential Analysis

The structural transformations of 2-OHOA/MO nano-dispersions triggered by pH reduction can be attributed to the pH-dependent protonation/deprotonation of the carboxylic groups in 2-OHOA. As protonation reduces charge repulsion between lipid membranes, it promotes the structural transition from lamellar vesicles to cubic phases (Prajapati et al., 2019). The ζ-potentials of these nano-dispersions are closely related to the protonation state of 2-OHOA's carboxyl groups. To monitor this, the samples were titrated, and the resulting pH-induced changes in ζ-potential are shown in **Fig. 2-5**. Generally, the ζ-potential of 2-OHOA/MO nano-dispersions decreased with pH reduction. At neutral pH (7.4), the 2-OHOA molecules are fully deprotonated, resulting in high negative ζ-potentials of –28.5 ± 1.3, –31.8 ± 1.0, and –31.4 ± 0.3 mV for 5, 7.5, and 10 mol% 2-OHOA in MO, respectively. Lowering the pH to 4.5 led to ζ-potentials of approximately –9.7 to –16.9 mV, reflecting partial protonation of 2-OHOA and a corresponding decrease in surface charge. At pH 3.0, ζ-potentials increased further to values between 0.0 and –2.1 mV, indicating full protonation and resulting in near-neutral surface charge. The apparent p*K*a values of 2-OHOA within the nano-dispersions were estimated as 5.05 ± 0.19, 5.32 ± 0.66, and 4.43 ± 0.72 for 5, 7.5, and 10 mol% 2-OHOA/MO, respectively. A lower concentration of ionizable carboxylic groups on the lipid membrane reduces negative surface charge density, decreasing the accumulation of protons and, consequently, lowering the apparent p*K*a (Salentinig et al., 2010). This explains the more pronounced structural transition at pH 4.5 in the 5 mol% 2-OHOA formulation.

Regarding hydrodynamic diameter and polydispersity index (PDI), all formulations showed a mean hydrodynamic diameter around 100 nm and a PDI of about 0.1 at pH 7.4, indicating a uniform size distribution. At pH 4.5, the mean hydrodynamic diameter increased significantly to 264.0 ± 2.7, 220.9 ± 4.4, and 214.4 ± 2.6 nm, with corresponding PDI increases to 0.31 ± 0.06, 0.26 ± 0.02, and 0.23 ± 0.01. These changes suggest an unstable state, with partial aggregation and a transition from ULVs to MLVs, reflected by the increase in particle size and PDI. At pH 3.0, the 5 mol% 2-OHOA formulation showed a reduction in particle size, while the 7.5 and 10 mol% formulations retained consistent sizes. The PDIs for all formulations at pH 3.0 decreased notably compared to pH 4.5, indicating a re-stabilized state and supporting the formation of cubic structures.

Together, the ζ-potential and DLS results confirm that the phase transition in nano-dispersions involves changes in both hydrodynamic diameter and surface charge state, providing further evidence of the pH-responsive structural transformations in these systems.

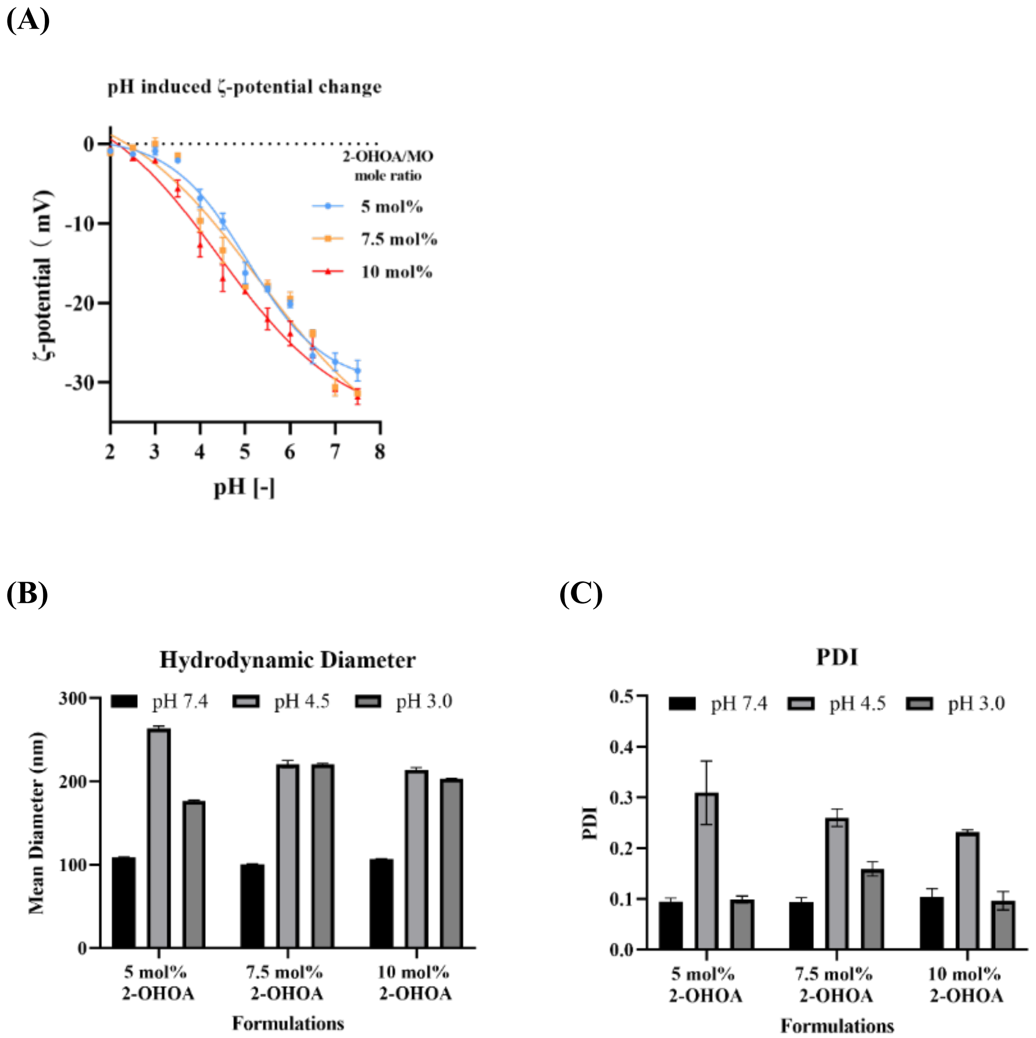

Figure 2-5. 2-OHOA/MO LNP ζ-potential and DLS Investigation Results. (A) ζ-potential as a function of pH for 5 (●), 7.5 (■) and 10 (▲) mol % 2-OHOA/MO nano-dispersions. **(B)** Polydispersity index (PDI) of 2-OHOA/MO nano-dispersions at pH 7.4, 4.5 and 3.0. **(C)** Mean hydrodynamic diameter of 2-OHOA/MO nano-dispersions at pH 7.4, 4.5 and 3.0. Samples concentrations were set at 1 mM. All measurements were conducted at 25 °C. Error bars represent *s.d*, *n*=3.

In the case of DOPC-based lamellar vesicles, as discussed in **Section 3.3**, this study observed the transition from MLVs to ULVs upon the incorporation of 2-OHOA. This study also monitored the hydrodynamic particle size and ζ-potential of liposomal formulations with and without 2-OHOA doping.

After LNP formulation, the amount of DOPC was quantified using the LabAssay Phospholipid kit. The results for particle size, polydispersity index (PDI), and ζ-potential are shown in **Fig. 2-6-(A~C)**. Compared to DOPC-only LNPs, the presence of 2-OHOA (in the 9-

1, 7-3, 5-5, and 3-7 formulations) slightly reduced the mean hydrodynamic diameters. This reduction can be attributed to the incorporation of 2-OHOA, which disrupts the packing order and increases the fluidity of the liposomal membranes by intercalating between phosphorylcholine (PC) molecules. The kinked structure of the 2-OHOA hydrocarbon tail, similar to oleic acid, is thought to enhance this effect (Jiang et al., 2017). Increased membrane fluidity promotes the formation of smaller LNPs (Zhao et al., 2021). In contrast, when 2-OHOA was used alone (without DOPC), it formed particles with a hydrodynamic diameter of 1634.0 ± 180.4 nm and a PDI of 1, indicating that 2-OHOA alone could not form stable nano-sized particles in aqueous solution at neutral pH.

LNPs composed solely of DOPC exhibited a ζ-potential of −2.40 ± 0.90 mV at pH 7.4. However, even at low concentrations, the incorporation of 2-OHOA significantly reduced the ζ-potential of the LNPs. Moreover, the ζ-potential of 2-OHOA-embedded LNPs showed a clear decreasing trend that corresponded to the ratio of 2-OHOA in the formulation. This is because the carboxylic groups in 2-OHOA dissociate in aqueous solution, resulting in a negative surface charge (Olechowska et al., 2019). Based on the structural stability of the formulations, DOPC-only, 9-1, 7-3, and 5-5 liposomes were selected for further investigation.

Water trapping efficiency is an important property of lamellar (*La*) structured LNPs, particularly for their use as drug carriers. The water trapping assay results (**Fig. 2-6-D**) confirmed the presence of an inner aqueous phase in the prepared *La* LNPs. Compared to DOPC-only LNPs, the 2-OHOA-embedded LNPs exhibited a reduced water trapping volume, which can be attributed to the decrease in hydrodynamic particle size as well as a reduced inner water pool volume.

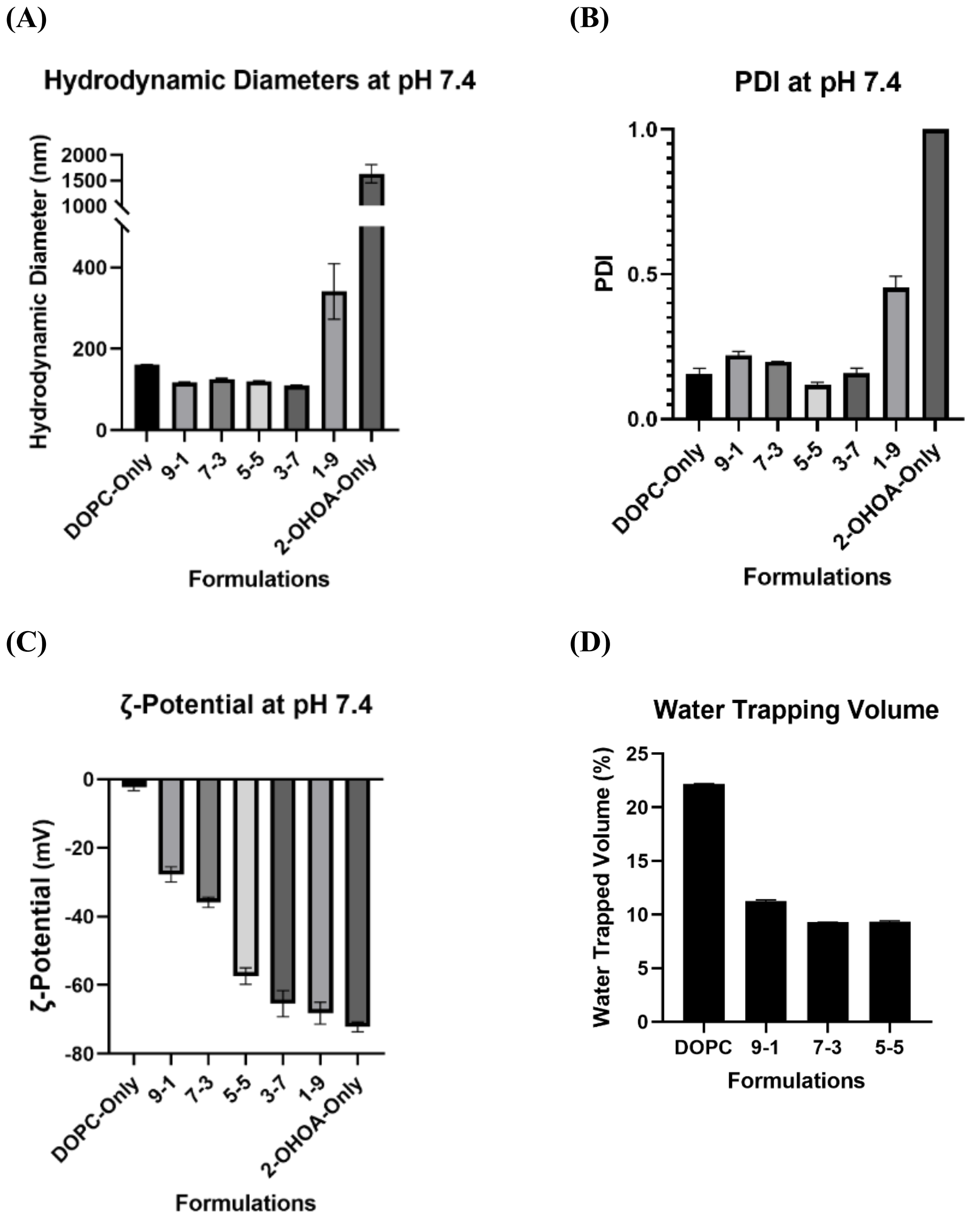

Figure 2-6. DOPC and DOPC/2-OHOA LNP Particle Size, ζ-potential and Water Trapping Volume Analysis Results. **(A)** Hydrodynamic diameter; **(B)** PDI and **(C)** ζ-potential. **(D)** Water trapping volume of 10 mM different liposomes. For DLS and ζ-potential investigation, all the liposome samples were diluted into 100 μM using D-PBS and the measurement were carried out at pH 7.4 and 25 °C, error bars represent ± *s.d*, *n*=3.

3.5. Cryo-TEM Images of Different LNPs

Cryo-TEM imaging reveals the internal lipid structures in an aqueous environment. As shown in **Fig. 2-7**, the MO-only cubosomes (**Fig. 2-7-A**) and cationic cubosomes (**Fig. 2-7-B**) exhibited cubic or spherical morphologies with clear internal lattice structures, with sizes approximately 200 nm. The DOPC-only liposomes (**Fig. 2-7-C**) displayed both ULV and MLV architectures, with diameters around 100 nm. For the 2-OHOA/MO nano-dispersion (MO + 5 mol% 2-OHOA) at pH 4.5, corresponding to the multi-phase mixture described in Section 3.2, the cryo-TEM images show a coexistence of ULVs, fused or closely approaching ULVs, MLVs, and cubosome-like particles. The morphologies and lattice structures observed by cryo-TEM align with the SAXS characterization patterns

(A) MO-only CBs **(B) Cationic CBs**

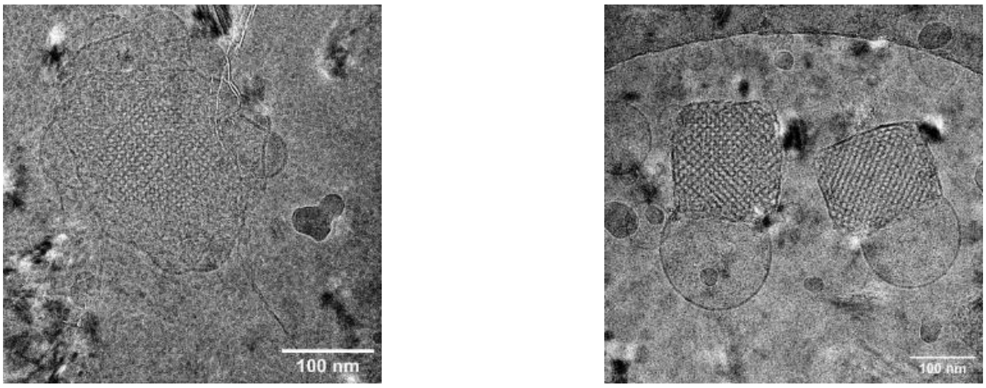

(C) DOPC-only LNPs **(D) 2-OHOA/MO LNPs (pH 4.5)**

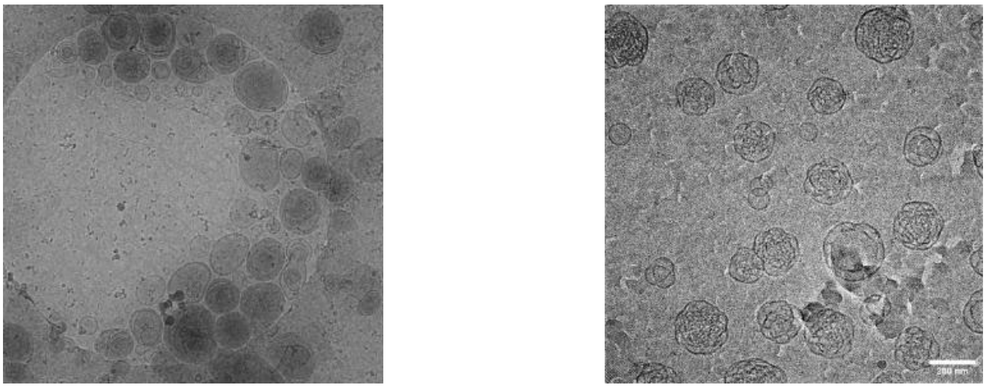

Figure 2-7. Cryo-TEM Images of Prepared LNPs. **(A)** MO-only cubosomes; **(B)** Cationic cubosomes (MO + 1 mol % DOTAP); **(C)** DOPC-only liposomes; **(D)** 2-OHOA/MO nano-dispersion (pH 4.5). For cubosomes, the concentrations were 56 mM; for DOPC liposome, the concentration was 10 mM; for the 2-OHOA/MO LNPs, the concentration was 56 mM. **A** and **B** were 59000 magnification (scale bar = 100 nm); **C** and **D** were 7500 magnifications (scale bar = 200 nm).

4. Summary

This chapter provides an in-depth investigation into the phase behavior of LNPs, characterized using advanced techniques including small-angle X-ray scattering (SAXS), dynamic light scattering (DLS), and cryo-transmission electron microscopy (cryo-TEM). The study demonstrates the versatility of lipid-based systems by showcasing representative SAXS patterns of various lyotropic phases, including lamellar vesicles (*Lα*) and cubic phase nanoparticles (*Im3m* and *Pn3m*).

The incorporation of 2-OHOA into DOPC and MO-based dispersions significantly altered the internal structure of these LNPs. Specifically, 2-OHOA induced a phase transition in DOPC-based liposomes from low-stacked MLVs to ULVs, highlighting its ability to modulate membrane architecture. In MO-based systems, a pH-triggered phase transition from lamellar vesicles to cubosomes was observed, confirmed by distinct SAXS patterns under different pH conditions.

The study also examined dynamic changes in size and surface charge using DLS and ζ-potential measurements, correlating these properties with the observed phase transitions. The changes in surface charge and particle size were in alignment with the structural rearrangements, emphasizing the role of pH and electrostatic interactions in modulating the stability and behavior of LNPs. Cryo-TEM imaging further supported these findings by capturing detailed morphologies of the LNPs, including both cubosomes and liposomes, under various pH environments.

Overall, these findings reinforce the concept that the phase behavior of LNPs is highly sensitive to their lipid composition, pH, and molecular packing parameters. This insight is crucial for the rational design of LNPs with tunable properties for drug delivery, particularly for developing pH-responsive systems capable of releasing therapeutic agents in a controlled manner under specific physiological conditions, such as the acidic tumor microenvironment. This chapter underscores the significance of lipid composition and phase behavior in optimizing LNP formulations for targeted drug delivery and controlled release.

Chapter 3

Study on the properties of lipid membranes across different LNP phases

1. Introduction

Chapter 3 explores the properties of lipid membranes across different LNP phases, characterized using fluorescence probes (Laurdan and DPH) and Raman spectroscopy. The 2-OHOA/MO binary system served as an ideal model for studying membrane properties during the transition from lamellar (*La*) to cubic (Q_{II}) phases. The results provided insights into changes in lipid packing, membrane-water interfacial polarity, and phase transitions. SAXS characterization confirmed that the prepared 2-OHOA/MO nano-dispersions exhibited lamellar phase structures (*Lα*) at pH 7.4 and 4.5, while at pH 3.0, cubic phase structures (*Im3m* and *Pn3m* space group) were observed. Additionally, DLS results indicated an unstable state of 2-OHOA/MO nano-dispersions at pH 4.5.

As illustrated in **Schematic 3-1**, at neutral pH (7.4), strong charge repulsion prevents tight packing of the 2-OHOA/MO lipid membrane system, resulting in the formation of lamellar phase vesicles. Upon pH reduction, embedded 2-OHOA undergoes partial protonation at pH 4.5 and full protonation at pH 3.0. Protonation of the carboxylic group on 2-OHOA reduces the negative charge at the lipid-water interface, modifying the membrane's spontaneous curvature and promoting tighter lipid packing, which facilitates the transition to cubic phase structures (Prajapati, R. et al., 2019). The distinct lipid packing in the *Lα* phase contrasts with that of the cubic phases (*Im3m/Pn3m*). This study hypothesizes that pH-triggered phase transitions are accompanied by changes in lipid-water interfacial polarity and variations in lipid membrane fluidity. To explore this further, this study employed Laurdan and DPH fluorescence probes to characterize the hydration state (polarity) and viscosity (fluidity) of the lipid membranes, respectively.

This study demonstrates the potential to track the physicochemical behavior and phase transitions of 2-OHOA/MO binary component nano-dispersions using Raman spectroscopy and fluorescence probes. These findings provide valuable insights into the relationship between lipid membrane property variations and the lamellar-to-cubic phase transition, which could inspire further development of pH-responsive drug delivery systems with optimized drug loading efficiency and controlled release patterns.

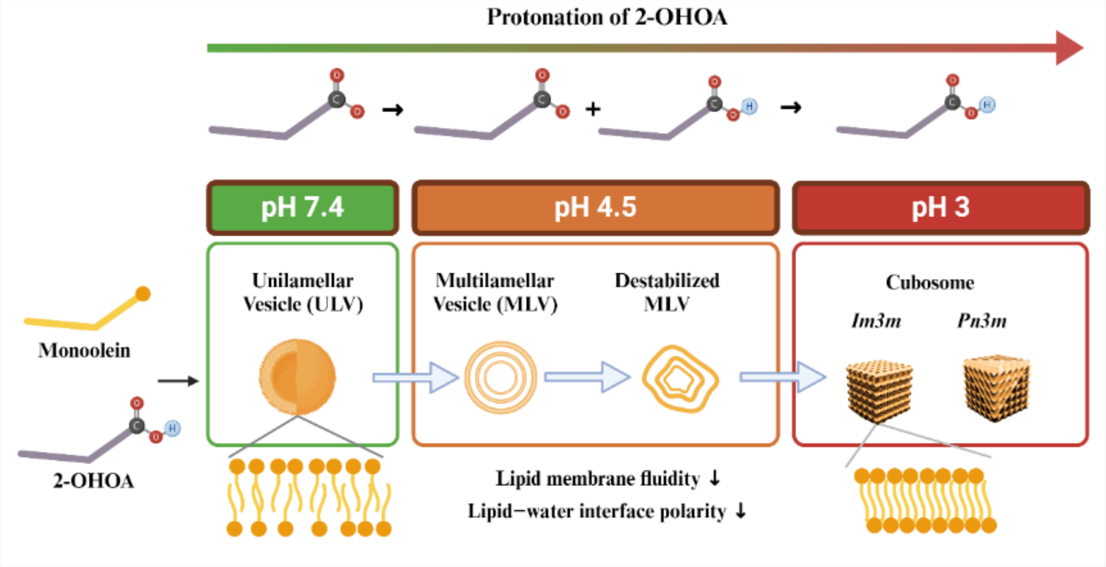

Schematic 3-1. Illustration of pH-Triggered Lamellar to Cubic Phase Transition.

2. Materials and Methods

2.1. Materials

Phospholipids (DOPC, DOTAP) and 2-hydroxyoleic acid (2-OHOA, >99%) were purchased from Avanti Polar Lipids (Alabaster, AL. USA). Monoolein (≥99%,1-Oleoyl-rac-glycerol), Pluronic F127 (Poly (ethylene oxide)-poly-(propylene oxide)-poly (ethylene oxide)), 1,6-Diphenyl-1,3,5-hexatriene (DPH, >98%) and Dodecanoyl-2-Dimethylaminonaphthalene (Laurdan, >97%) were purchased from Sigma-Aldrich. Sodium hydroxide (NaOH, ≥97.0%), hydrochloric acid (HCl, 35.0~37.0%), chloroform (≥99.0%) and methanol (≥99.8%) were purchased from Wako Pure Chemical Industries.

2.2. State Steady Laurdan Fluorescence Spectra Measurement

Laurdan was dissolved in ethanol at 1 mM as stock solution. The prepared LNPs were adjusted to 1 mM. Laurdan was added into samples (final Laurdan concentration of 10 μM) and incubated for 1 hr shielded from light. The Laurdan stained samples were investigated using fluorescence spectrophotometer (FP-6500, JASCO, Japan). Samples were excited with 340 nm wavelength light, and emission spectra were recorded from 400 to 600 nm. All the measurements were carried out at 25°C. The generalized polarization value (*GP*) was calculated using **Eq. (3-1)** (Parassassi et al., 1991):

$$GP = \frac{(I_{440} - I_{490})}{(I_{440} + I_{490})} \qquad Eq. (3-1)$$

Where I_{440} and I_{490} are Laurdan emission intensities at 440 and 490 nm, respectively.

2.3. DPH Anisotropy Measurements

DPH was dissolved in ethanol to prepare a stock solution. LNP suspensions were adjusted to a concentration of 1 mM, and DPH was added to the samples to reach a final concentration of 5 μM. The mixtures were then incubated at 25°C for 1 hour, protected from light. The samples were analyzed using a fluorescence spectrophotometer (FP-6500, JASCO, Japan) equipped with polarizers. Excitation was performed with vertically or horizontally polarized light at 360 nm, and emission fluorescence intensities, both perpendicular and parallel to the excitation light, were recorded at 430 nm. All the measurements were carried out at 25°C. The polarization (*P*) of DPH was calculated using the following equations:

$$P = \frac{I_\perp - G \times I_\parallel}{I_\perp + G \times I_\parallel} \qquad Eq.(3-2)$$

$$G = \frac{i_\perp}{i_\parallel} \qquad Eq.(3-3)$$

Where $I_\perp$ (0°, 0°) and $I_{/\!/}$ (0°, 90°) are emission intensities perpendicular and parallel to the vertically polarized excited light, respectively; $i_\perp$(90°, 0°) and $i_{/\!/}$(90°, 90°) are emission intensities perpendicular and parallel to the horizontally polarized excited light, respectively; *G* is the correction factor. The fluidity was evaluated and compared basing on the reciprocal of polarization (*1/P*).

2.4. Raman Spectroscopic Investigation

The LNPs were analyzed using Raman spectroscopy. The pH of the samples was adjusted as previously described, and the final concentration of each sample was set to 50 mM. Raman spectra of the prepared nano-dispersions were acquired using a LabRAM HR-800 confocal Raman microscope (Horiba, Ltd., Japan). A YAG laser (100 mW, 532 nm wavelength) was focused through a ×20 objective lens. Spectra were recorded with a 30s exposure time and repeated three times for each sample. All measurements were conducted at 25°C. After background signals from the Pluronic F127 solution (2mg/mL) were subtracted, the spectra were baseline corrected.

To compare the lipid membrane physicochemical properties of nano-dispersions with different phases, the lipid chain packing (R value) and lipid chain torsion (S value) were calculated according to the following equations (Suga, K. et al., 2018).

$$R = \frac{I_{2850}}{I_{2930}} \qquad Eq.(3-4)$$

$$S = \frac{I_{1082}}{I_{1124}} \qquad Eq.(3-5)$$

In these equations, I_{2850}, I_{2930}, I_{1082} and I_{1124} are the Raman spectra peak intensities at 2850, 2930, 1082 and 1124 cm^{-1} respectively.

3. Results and Discussion

3.1. 2-OHOA/MO Membrane Fluidity/Polarity Variation During Phase Changing

The presence of the stabilizer Pluronic F127 in the nano-dispersion is an important factor that could influence membrane characteristics. Pluronic F127 is a triblock copolymer composed of polyethylene oxide (PEO) and polypropylene oxide (PPO) arranged in a symmetric PEO-PPO-PEO structure. As a stabilizer, Pluronic F127 primarily localizes on the outer membranes of nanoparticles (Yu, H. et al., 2024). Additionally, unbound Pluronic F127 molecules in solution may also affect the Laurdan fluorescence spectra. To standardize the effect of Pluronic F127, all samples for Laurdan and DPH investigations were adjusted to the same concentration (1 mM 2-OHOA + MO and 0.036 mg/mL Pluronic F127). This approach enables the tracking and comparison of changes in lipid membrane-water interfacial polarity and membrane fluidity during the pH-triggered phase transition.

The *GP* values of 2-OHOA/MO nano-dispersions under different pH conditions are summarized in **Fig. 3-1-A**. The typical Laurdan spectra of 5 mol% 2-OHOA/MO dispersions at pH 7.4, 4.5, and 3.0 are shown in **Fig. 3-1-B**. To assess the impact of unbound Pluronic F127 on Laurdan spectra, Laurdan was added to a Pluronic F127 solution (0.036 mg/mL), and the resulting spectra are displayed in **Fig. 3-1-C, D**. Laurdan molecules can bind to the PPO regions of Pluronic F127, emitting fluorescence (Calori, I. R. et al., 2019). However, Laurdan spectra in Pluronic F127 solution differ significantly from those in 2-OHOA/MO nano-dispersions. The calculated *GP* value for Pluronic F127 solution was –0.049 ± 0.003 (at pH 7.4), with no observable variations upon pH changes. Therefore, the impact of unbound Pluronic F127 on Laurdan spectra remains consistent across different pH conditions. Additionally, the fluorescence of Laurdan in the Pluronic F127 solution was notably lower than that in the 2-OHOA/MO dispersions (**Fig. 3-1-C**), likely due to quenching by excess water molecules (Lakowicz, J. R. 2006). Thus, it can be concluded that the Laurdan spectra in the 2-OHOA/MO dispersions primarily reflect lipid membrane properties, rather than contributions from unbound Pluronic F127.

For the 2-OHOA/MO nano-dispersion, as the pH decreased from 7.4 to 4.5, no significant changes in *GP* values were observed across all formulations. However, at pH 3.0, a dramatic increase in *GP* values was noted in all formulations. According to the SAXS characterization results, at pH 3.0, a transition from *Lα* to *Im3m/Pn3m* phases was observed, resulting in a more ordered packing of lipid bilayers both at the membrane surface and within the internal structure. This more ordered lipid packing reduces membrane permeability to water, resulting in decreased polarity at the lipid-water interface and a less polar environment around the Laurdan probe.

(A)

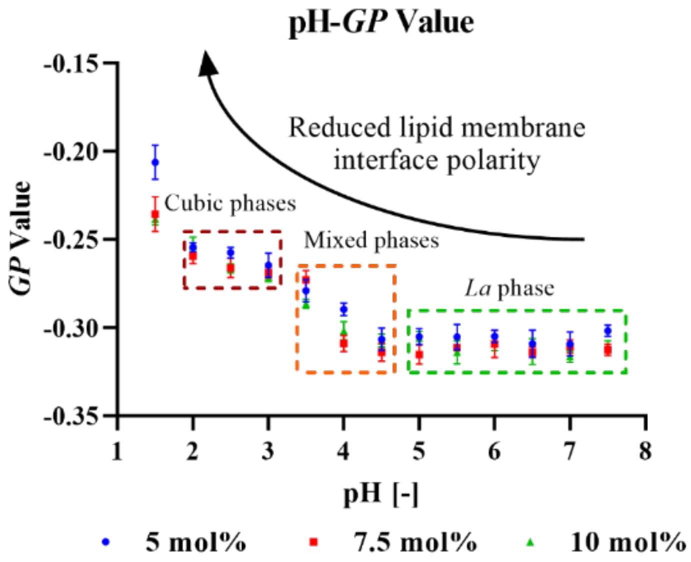

(B)

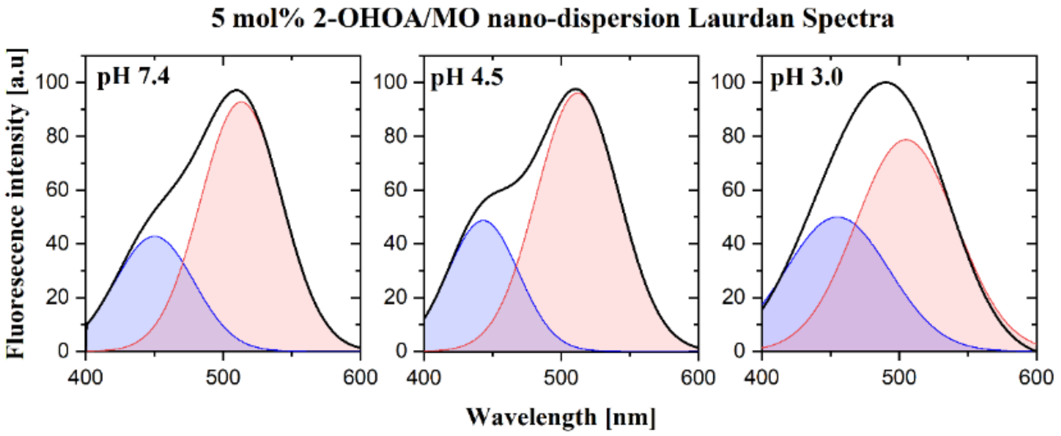

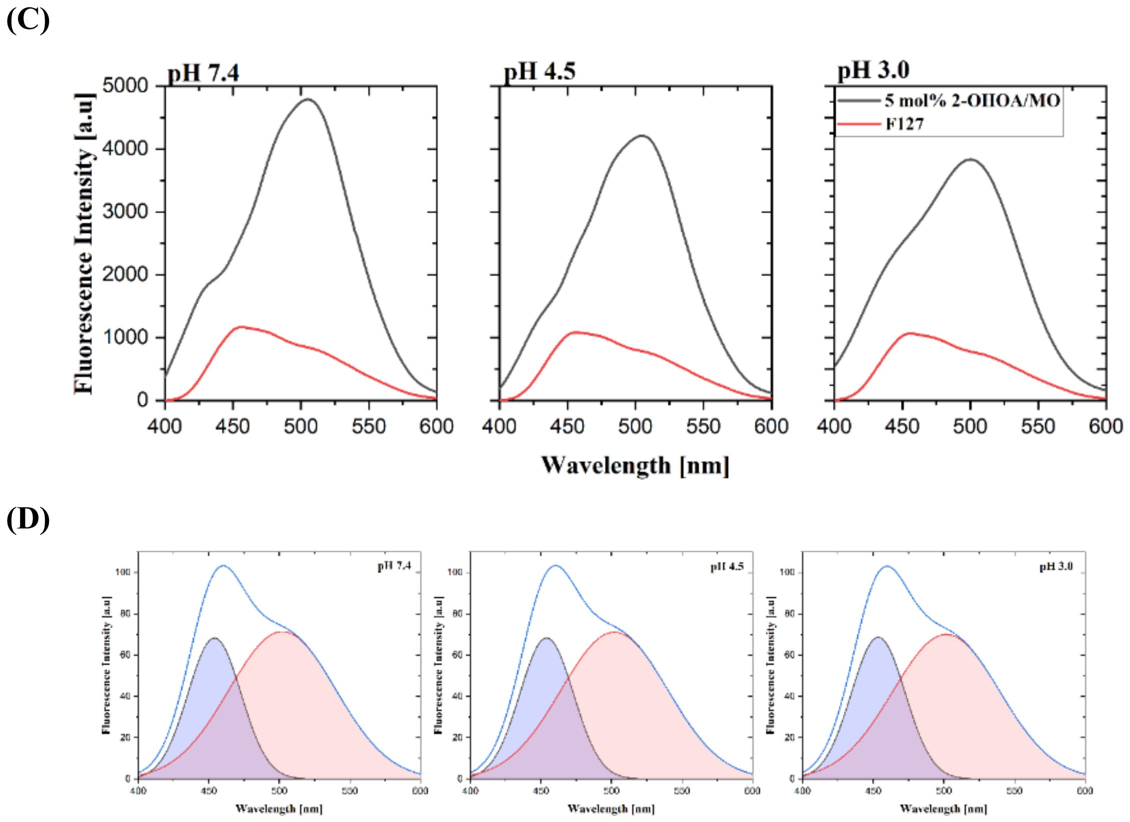

Figure 3-1. Laurdan *GP* value results. (A) pH-dependent *GP* values of 2-OHOA/MO nano-dispersions. The blue, red and green color represents 5 mol%, 7.5 mol% and 10 mol% 2-OHOA formulation respectively. **(B)** Normalized Laurdan spectras of 5 mol% 2-OHOA nano-dispersions at pH 7.4, 4.5 and 3.0. The obtained fluorescence spectrum (black line) was deconvoluted into two spectra: a blue peak originates from the Laurdan in the low polarity region; and a red peak originates from the Laurdan in the high polarity region. The fatty acid concentrations were set at 1 mM and Laurdan concentration was 10 µM. **(C)** Comparation of Laurdan (10 µM) spectra in 5 mol% 2-OHOA/MO dispersion (1 mM 2-OHOA+MO, containing 0.036 mg/mL Pluronic F127, shown in black line) and in Pluronic F127 solution (0.036 mg/mL, shown in red line). **(D)** Normalized Laurdan spectras of 0.036 mg/mL F127 at pH 7.4, pH 4.5 and pH 3.0 respectively. The obtained fluorescence spectrum (black line) was deconvoluted into two spectra: a blue peak originates from the Laurdan in the low polarity region; and a red peak originates from the Laurdan in the high polarity region. All measurements were carried out at 25 °C. Error bars represent ± *s.d*, *n*=3.

To further confirm variations in lipid membrane fluidity induced by phase transitions, another fluorescence probe, DPH, was employed. As shown in **Fig. 3-2**, DPH exhibited negligible fluorescence in the Pluronic F127 solution (0.036 mg/mL), in contrast to its strong fluorescence in 2-OHOA/MO nano-dispersions (1 mM 2-OHOA + MO and 0.036 mg/mL F127). This difference is due to the quenching of DPH in aqueous solution, which is more pronounced than with Laurdan. However, after incubation with the 2-OHOA/MO dispersion, DPH fluorescence significantly increased, indicating successful insertion into the hydrophobic lipid membrane chains. Thus, the impact of unbound Pluronic F127 on DPH fluorescence can be considered negligible. Furthermore, Nakano et al. demonstrated that DPH-PA (a DPH analogue) probes are located in the interior of cubosomes rather than at the particle surface, and DPH anisotropy did not depend on Pluronic F127 concentrations (Nakano, M. et al., 2005). In contrast to Laurdan, which predominantly localizes at the membrane-water interface, DPH resides in the lipid acyl chain regions and is therefore more sensitive to changes in the internal lipid chain packing status (Aguilar, L. et al., 2012).

The variations in membrane fluidity were quantified by calculating the *1/P* value, where a high *1/P* value corresponds to higher membrane fluidity, and a low *1/P* value indicates lower fluidity (Suga, K. et al., 2013). The *1/P* values are summarized in **Fig. 3-2**. At pH 7.4, higher amounts of 2-OHOA led to increased membrane fluidity, as reflected by higher 1/P values. An interesting phenomenon occurred as the pH was reduced to 4.5, where the binary component nano-dispersions showed increased membrane fluidity (higher 1/P values). However, at pH 3.0, the membrane fluidity sharply decreased, with 1/P values lower than those observed at pH 7.4. The dispersions in the Lα phase were destabilized and entered a pre-transition state at pH 4.5. During this pre-transition state, the 2-OHOA/MO lipid membranes were reorganizing, leading to a more disordered lipid packing and, thus, increased fluidity.

Referring to the lattice parameter (α) and water channel radius (r_w) results obtained from SAXS measurements (**Table 2-2**), at pH 3.0, the cubic phase nano-dispersions exhibited the following trends: α (5 mol% 2-OHOA) > α (7.5 mol% 2-OHOA) > α (10 mol% 2-OHOA), and similarly, r_w (5 mol% 2-OHOA) > r_w (7.5 mol% 2-OHOA) > r_w (10 mol% 2-OHOA). A higher concentration of 2-OHOA in MO resulted in smaller lattice parameters and narrower water channel radius. The lattice parameter and water channel radius are influenced by the lipid packing properties of 2-OHOA/MO and the repulsive force in the lipid membrane, which is affected by the protonation state of 2-OHOA. At pH 3.0, when 2-OHOA is fully protonated (in a less charged state), lipid packing properties become the dominant factor. The 5 mol% 2-OHOA cubic phase nano-dispersion had the largest lattice parameter (18.11 nm) and the widest water channel radius (3.84 nm), which correlates with a highly ordered lipid membrane (low *1/P* value). Conversely, the high membrane fluidity (high *1/P* value) of the 10 mol% 2-OHOA nano-dispersion is likely associated with looser lipid packing, resulting in increased membrane curvature and consequently smaller lattice parameters and narrower water channels (Czeslik, C. et al., 1995).

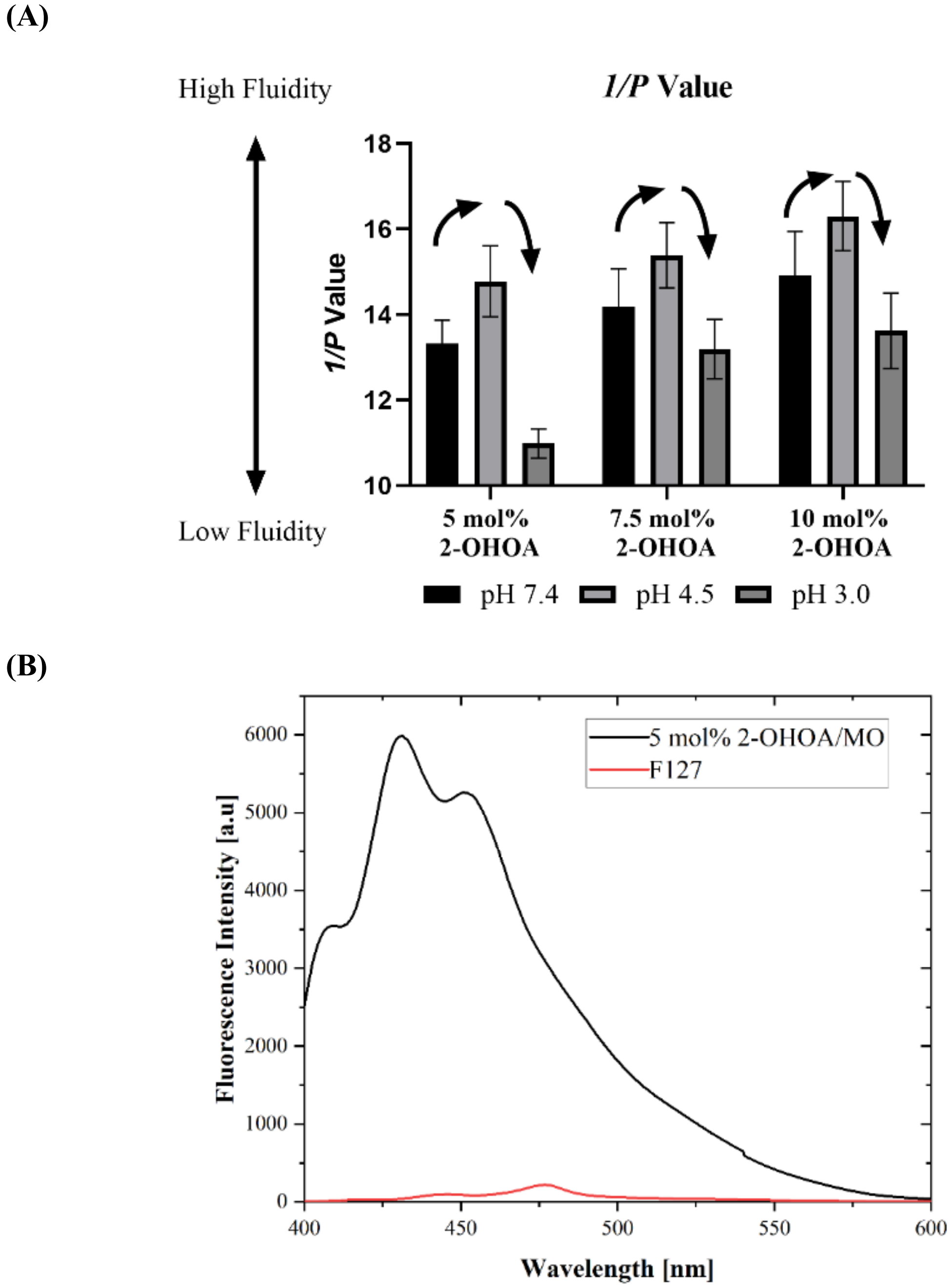

Figure 3-2. DPH Analysis Results. (A) DPH 1/P value results of 2-OHOA/MO nano-dispersions at pH 7.4, 4.5 and 3.0. The fatty acid concentrations were set at 1 mM and DPH concentration was 5 µM. **(B)** DPH fluorescence spectra in 5 mol% 2-OHOA/MO dispersion and F127 solution. Black line is DPH (5 µM) spectra in 5 mol% 2-OHOA/MO dispersion (1

mM 2-OHOA+MO, containing 0.036 mg/mL F127). Red line is DPH (5 μM) spectra in 0.036 mg/mL F127 solution. Samples were adjusted to pH 7.4 for measurements. DPH was incubated with each sample for 1 hr shielded from light. Samples were measured in triplicate and averaged among 3 measurements results, measurement temperature was set at 25 °C.

3.2. Raman Spectroscopic Analysis

Raman spectroscopy offers a label-free method for characterizing the physicochemical properties of lipid membranes (Batenjany, M. M. et al., 1994). Specifically, the peak intensity ratios in the 1000–1200 cm^{-1} and 2800–3000 cm^{-1} region serve as reliable indicators of lipid chain torsion and chain packing behaviors in lipid membrane systems (Suga, K. et al., 2015). As previously discussed, the 5 mol% 2-OHOA/MO formulation exhibited the most pronounced transition from ULV (pH 7.4) to MLV (pH 4.5) to *Im3m* cubosome (pH 3.0). Therefore, in this Raman spectroscopic investigation, the 5 mol% 2-OHOA formulation was chosen to track the variations in lipid membrane physicochemical properties during the *Lα* to Q_{II} phase transition.

Typical Raman spectra of the nano-dispersions are shown in **Fig. 3-3**. The spectral region from 1000 to 1200 cm–1 corresponds to the stretching vibrations of the C–C bonds in the alkyl chains of the lipids (Lis, L. J. et al., 1976). The symmetric and asymmetric vibrational modes of the methyl (−CH3) and methylene (−CH2−) groups are clearly visible in the 2800–3100 cm^{-1} region of the Raman spectra (**Fig. 3-3-B**).

The peak intensity ratios of different C–C stretching and C–H stretching peaks provide a qualitative method for monitoring lipid membrane behavior. The peak assignments in the C–C stretching and C–H stretching regions used in this study are summarized in Table 3-1. The Raman peaks at 1082 cm^{-1} and 1124 cm^{-1} correspond to the gauche and trans modes of the C–C chain vibrations, respectively, and are indicative of lipid hydrocarbon chain torsion (Fox, C. B. 2007). The peaks at 2854 cm^{-1} and 2890 cm^{-1} correspond to the asymmetric and symmetric vibrations of (−CH2−), respectively, which are sensitive to hydrophobic interactions between hydrocarbon chains and reflect chain packing (Czamara, K. et al., 2014). In this study, chain torsion (S) was defined as the Raman peak intensity ratio at 1082 cm^{-1} and 1124 cm^{-1}, which indicates lipid chain torsion. Chain packing (R) was defined as the Raman peak intensity ratio at 2854 cm^{-1} and 2890 cm^{-1}, reflecting lipid chain lateral packing density. S and R values were calculated to assess the lipid membrane behavior of the nano-dispersions. In general, higher S and R values indicate greater viscosity and a more tightly packed lipid membrane.

Fig. 3-3-C, D summarize the S and R values for MO-only (pH 7.4), 2-OHOA-only (pH 7.4), and 5 mol% 2-OHOA (pH 7.4, 4.5, and 3.0) dispersions. Generally, MO-only dispersions at pH 7.4 exhibited the highest S and R values, while 2-OHOA-only dispersions at pH 7.4 showed the lowest S and R values. These results confirm that cubic phase nano-dispersions have a more densely packed lipid membrane state compared to Lα phase nano-dispersions. For the 5 mol% 2-OHOA/MO dispersion, maximum S and R values were observed at pH 3.0, suggesting that the 2-OHOA/MO assembly at pH 3.0 represented the most ordered state (*Im3m* cubic phase). These Raman spectroscopic findings align with the Laurdan *GP* value results and the DPH (*1/P*) results. Together, these results confirm that cubic phase dispersions exhibit a higher lipid membrane packing state, lower fluidity, and lower lipid-water interfacial polarity compared to lamellar phase dispersions. At the intermediate state (pre-phase transition) at pH 4.5, the lipid membrane exhibited a heterogeneous state. Laurdan, DPH, and Raman spectroscopy demonstrated different sensitivities to the physicochemical properties of the lipid membranes.

(A)

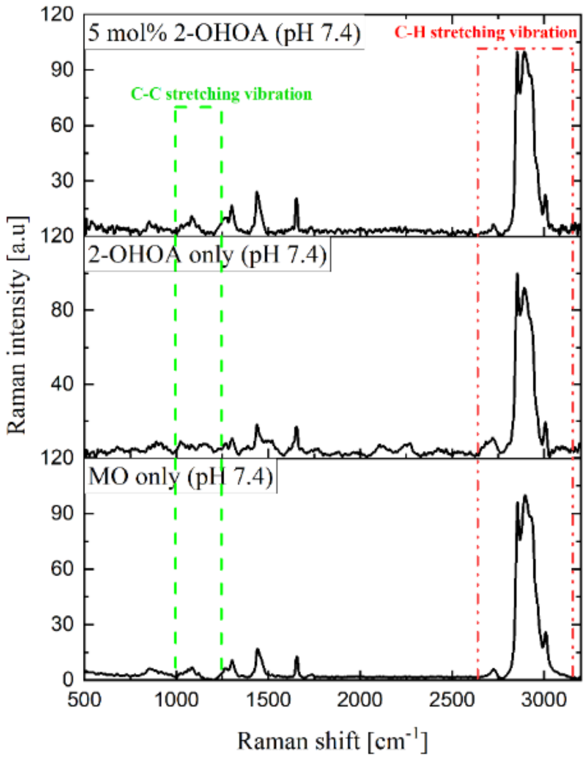
5 mol% 2-OHOA (pH 7.4)
C-H stretching vibration
C-C stretching vibration
2-OHOA only (pH 7.4)
MO only (pH 7.4)
Raman intensity [a.u]
120
90
60
30
120
80
40
120
90
60
30
0
500
1000
1500
2000
2500
3000
Raman shift [cm^{-1}]

(B)

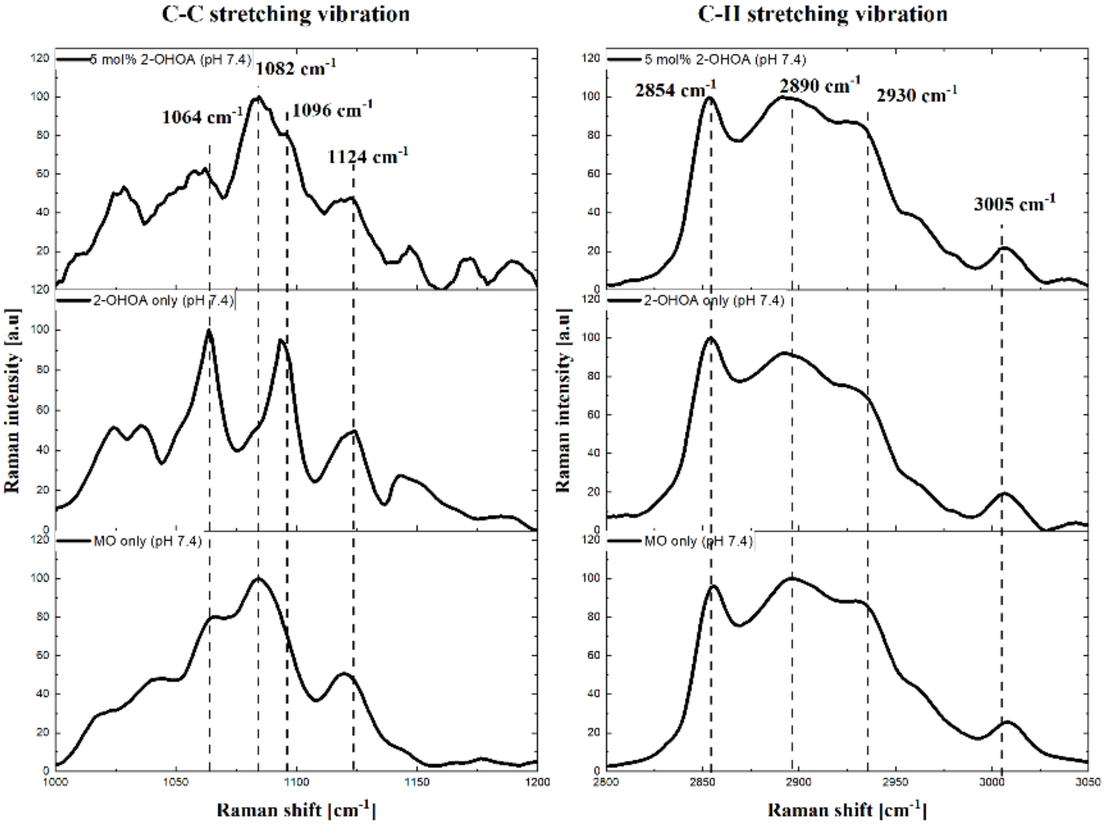
C-C stretching vibration
C-H stretching vibration
5 mol% 2-OHOA (pH 7.4)
2-OHOA only (pH 7.4)
MO only (pH 7.4)
1064 cm^{-1}
1082 cm^{-1}
1096 cm^{-1}
1124 cm^{-1}
2854 cm^{-1}
2890 cm^{-1}
2930 cm^{-1}
3005 cm^{-1}
Raman intensity [a.u]
120
100
80
60
40
20
0
1000
1050
1100
1150
1200
2800
2850
2900
2950
3000
3050
Raman shift [cm^{-1}]

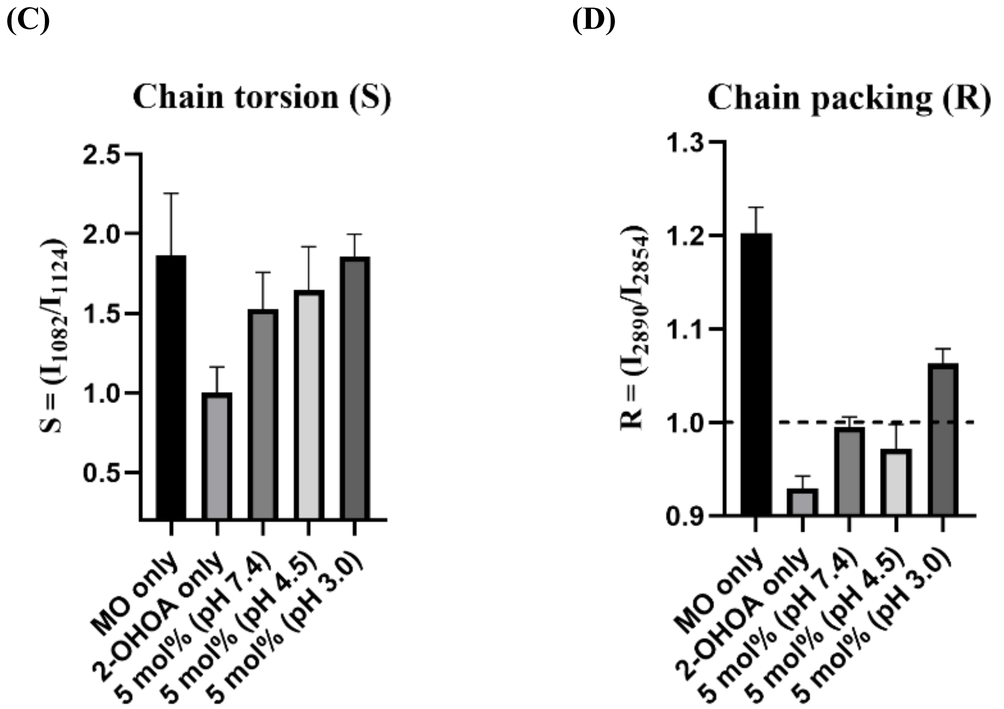

Figure 3-3. Raman Spectra of Different Dispersions and Calculated *R*, *S* Values of Different Samples. (A) Representative Raman spectra of MO only, 2-OHOA and 5 mol% 2-OHOA in MO. **(B)** C-C stretching vibration region and C-H stretching vibration region respectively. The dominant peaks are marked by the dashed lines. **(C)** Calculated chain torsion *S* (I_{1082}/I_{1124}) values. **(D)** Calculated chain packing *R* (I_{2850}/I_{2930}) values. Sample concentration is 50 mM and all measurements are carried out at 25 °C. Error bars represent ± *s.d*, *n* = 3~5.

Table 3-1. Raman Peak Assignments and Peak Intensity Ratios in This Study

Assignment	**Wavenumber [cm^{-1}]**
$\nu_{as}(CH_2)$	2890
$\nu_{s}(CH_2)$	2854
ν(C-C) gauche	1082
ν(C-C) trans	1124

Intensity ratio	Indication
R (I_{2890}/I_{2854})	Lipid chain packing
S (I_{1082}/I_{1124})	Lipid chain torsion

4. Summary

The pH-triggered transition from the lamellar (*Lα*) phase to the cubic (Q_{II}) phase in 2-OHOA/MO nano-dispersions was confirmed through SAXS characterization, demonstrating a clear structural transformation driven by environmental pH changes. The physicochemical properties of the lipid membranes in these nano-dispersions were further analyzed using fluorescence probes such as DPH and Laurdan. At neutral pH (7.4), the MO-only nano-dispersion exhibited a distinct cubic *Im3m* phase, while the 2-OHOA-only dispersion remained in the Lα phase. Fluorescent probe studies revealed that both the lipid-water interfacial polarity and lipid membrane fluidity in 2-OHOA/MO nano-dispersions changed in tandem with the observed phase transition.

Raman spectroscopy provided additional insights into the molecular dynamics during the phase transition. The chain torsion (S) and chain packing (R) parameters were found to be maximized at pH 3.0 in the 5 mol% 2-OHOA/MO assemblies, correlating with the formation of the *Im3m* cubic phase. These findings suggest a strong relationship between molecular packing, lipid membrane flexibility, and the structural organization of the nano-dispersions, particularly under acidic conditions.

This chapter highlights the capability to track both the phase behavior and the lipid-membrane physicochemical properties of pH-responsive nano-dispersions in real-time during phase transitions. The synchronous changes in lipid properties with the phase shift provide valuable insights into how structural transformations impact the overall behavior of lipid nanoparticles.

The findings from this work offer promising implications for the design and development of pH-responsive drug delivery systems. By understanding the interplay between lipid composition, phase behavior, and membrane properties, it becomes possible to optimize drug loading efficiency and create systems with controlled release profiles, tailored for a wide range of therapeutic payloads. This research paves the way for more advanced, responsive LNP platforms that can be fine-tuned for specific biomedical applications, particularly in environments where pH fluctuations are critical, such as in the tumor microenvironment.

Chapter 4

Monitor the Impact of LNPs on Cellular Plasma Membrane Polarity/Fluidity using Laurdan Two-Photon Microscopy

1. Introduction

Plasma membrane fluidity is a key factor influencing cancer cell adhesion and migration. One of the hallmark characteristics of cancer cells is altered lipid metabolism, leading to abnormal cell membrane compositions. The composition and fluidity of cancer cell plasma membranes vary across different cell types. For example, glioma cells exhibit higher fluidity compared to normal brain cells. Increased cancer cell membrane fluidity is associated with a higher metastasis rate, while lower fluidity hinders the motility of cancer cells during epithelial–mesenchymal transition (EMT).

Cell membrane fluidity is a dynamic property influenced by multiple interacting factors. The balance of lipid types, including their saturation levels and the presence of cholesterol, plays a crucial role in determining membrane fluidity or rigidity. Cholesterol serves as a critical modulator, impacting fluidity depending on its concentration and interactions with lipids. Temperature and environmental conditions also affect membrane fluidity by altering lipid mobility and phase transitions. Additionally, interactions between membrane proteins, the cytoskeleton, and external factors like the extracellular matrix (ECM) can further modulate fluidity, influencing cellular functions. In pathological conditions, such as cancer or neurodegenerative diseases, changes in membrane fluidity can significantly impact cell behavior, including altered adhesion, migration, and signaling. Understanding these factors and their effects on membrane fluidity is essential for developing therapeutic strategies aimed at modifying membrane properties for disease treatment or improving drug delivery systems.

LNPs can significantly affect the biophysical properties of cell membranes, influencing interactions with cells and the efficacy of drug delivery. LNPs can alter membrane fluidity, which, in turn, affects membrane protein function, lipid dynamics, and processes such as signaling and endocytosis. LNPs can also modify membrane permeability by transiently disrupting the membrane, which may facilitate the entry of therapeutic agents or cause membrane damage if not properly designed. Additionally, LNPs can influence the organization of lipid rafts—microdomains rich in cholesterol and sphingolipids—thereby affecting signal transduction and receptor clustering. LNPs may also impact membrane tension and mechanical properties, which is crucial for gene delivery, where effective membrane crossing is required. The biophysical properties of the cell membrane also influence the endocytic pathways that cells use to internalize LNPs, with different formulations potentially favoring specific endocytic mechanisms. Furthermore, LNPs can interact with and exchange lipids with the cell membrane, potentially altering membrane composition and function, which can impact various cellular processes, including membrane repair and signaling. Understanding these interactions is essential for designing LNPs with optimal properties for targeted therapeutic applications.

In this study, the Laurdan (6-Dodecanoyl-2-Dimethylaminonaphthalene) fluorescence probe was used to examine the heterogeneity and variations in cellular lipid membrane polarity and fluidity through two-photon microscopy imaging and fluorescence photometry. Laurdan is commonly used as a membrane probe due to its large excited-state dipole moment, which enables it to indicate the extent of water penetration into the bilayer surface through dipolar relaxation. When incorporated into a lipid bilayer, Laurdan senses its environment, with its spectrum shifting according to the water content of the bilayer. Water penetration correlates with membrane fluidity and lipid bilayer packing. Compared to other fluorescent probes for cell membrane analysis (e.g., DPH, Nile Red), Laurdan exhibits dual fluorescence spectrum properties, making it sensitive to changes in membrane phase and polarity. By measuring Laurdan's fluorescence spectrum, researchers can distinguish between liquid crystalline and gel phases of membranes, a property not commonly found in many other fluorescent probes. Additionally, Laurdan's fluorescence properties enable quantitative analysis. The generalized polarization (*GP*) value of Laurdan-stained cells was calculated to quantify variations in cell membrane polarity and fluidity. Generally, a high *GP* value indicates low membrane polarity or reduced membrane fluidity, while a low *GP* value suggests the opposite. Microscopy provides a unique tool for studying membrane heterogeneity, and two-photon excitation has the added advantage of inducing less damage to live cells and significantly reducing photobleaching of Laurdan.

Another environment-sensitive fluorescent probe, LipiORDER, was used to corroborate the Laurdan imaging results. LipiORDER is a pyrene-based solvatochromic fluorescent dye that integrates into the lipid bilayer and alters its fluorescence properties in response to environmental changes. Typically, the liquid-ordered (*Lo*) phase represents a highly packed lipid bilayer with low fluidity, while the liquid-disordered (*Ld*) phase is a sparsely packed bilayer with high fluidity. LipiORDER's fluorescence changes from green on the Lo membrane to red on the Ld membrane, providing insights into the lipid packing of the cell membrane. The lipid packing of the cell membrane can be approximated and compared by quantifying the LipiORDER red/green fluorescence intensity ratios (*R/G* ratio).

These methodologies enable the assessment and visualization of alterations in cell membrane polarity, fluidity, and lipid packing status, facilitating the evaluation and monitoring of cellular plasma membrane biophysical properties.

2. Materials and Methods

2.1. Materials

1,2-dipalmitoyl-*sn*-glycero-3-phosphoethanolamine-*N*-(7-nitro-2-1,3-benzoxadiazol-4-yl) (16:0 NBD PE) were purchased from Avanti Polar Lipids. 6-Dodecanoyl-2-Dimethylaminonaphthalene (Laurdan) was purchased from Thermo Fisher Scientific. LipiORDER was purchased from Funakoshi. BD Pharmingen™ FITC Annexin V Apoptosis Detection Kit I was purchased from BD Biosciences. 3-(*N*-Morpholino) propanesulfonic Acid (MOPS free acid), Sodium acetate, Ethylenediamine-*N, N, N', N'*-tetraacetic acid (EDTA-2Na), and Lipi-Red was purchased from Dojindo Laboratories. Chloroform, Dimethyl sulfoxide (DMSO), Fetal bovine serum (FBS), Eagle's Minimum Essential Medium (E-MEM), Dulbecco's Modified Eagle Medium (D-MEM), Trypsin (0.25 w/v%, EDTA solution with Phenol Red), LabAssay Phospholipid kit, MTT (3-(4,5-Dimethylthiazol-2-yl)-2,5-Diphenyltetrazolium Bromide), Penicillin-Streptomycin solution, Anhydrous Cobalt (II) Chloride ($CoCl_2$) and D-PBS were purchased from Fujifilm Wako Pure Chemical.

2.2. Cell Culture

HepG-2, NP-8, 4T1, J774.1 and OUMS-36T cells obtained from the Japanese Collection of Research Bioresources (JCRB) were used in this study. HepG-2, NP-8 and 4T1 cells were cultured in E-MEM media; J774.1 and OUMS-36T cells were cultured in RPMI media. All cell culture media were supplemented with 10% v/v FBS and streptomycin-penicillin. Cells were cultured at 37°C in in a humidified atmosphere containing 5% CO_2.

2.3. Laurdan Staining and Fluorescence photometer Analysis

Laurdan was dissolved in DMSO to create a 1 mM stock solution. To measure the steady-state Laurdan fluorescence spectrum in cell membranes, cells were seeded in 6-well plates. After treatments or non-treatment culture (blank control), cell culture media was carefully removed, and cells were gently washed using D-PBS. Next, fresh pre-warmed media containing 10 μM Laurdan was added to each well, and cells were incubated for 30 minutes in a cell culture incubator, shielded from light. After Laurdan staining, cells were washed, detached using trypsin, and collected. The cells were suspended in D-PBS and analyzed using a fluorescence spectrometer (FP-8500, Jasco, Japan). Steady-state Laurdan spectra were obtained with an excitation wavelength of 340 nm, and emission was collected in the range of 400–600 nm. For the blank control group, cells from three replicate wells were stained with Laurdan and analyzed. For each treatment group (including each liposome formulation and free 2-OHOA treatment), cells from five replicate wells were stained with Laurdan and analyzed. Each replicate was measured three times, and the Laurdan spectra were averaged across the three measurements.

The Laurdan steady-state fluorescence spectra data from fluorescence spectrometer were collected and analyzed. The GP_s value (GP value calculated according to steady-state Laurdan spectra) was calculated according to the following equation:

$$GP_s = \frac{(I_{440} - I_{490})}{(I_{440} + I_{490})} \qquad Eq.(4-1)$$

Where I_{440} and I_{490} represent the fluorescence intensity at 440 and 490 nm, respectively.

2.4. Laurdan Staining and Two-Photon Microscopy (TPM) Imaging

For two-photon microscopy observations, cells were initially cultured in 35 mm Φ glass-bottom dishes. The Laurdan staining procedure was performed as described previously. After staining, the samples were observed under a two-photon microscope. To maintain the temperature and CO_2 concentration of the cell samples during imaging, the glass-bottom dishes were placed in a live cell imaging chamber equipped with a stage-top incubator (INUB-PPZI, Tokai Hit, Japan), which maintained a 37°C and 5% CO_2 environment. Two-photon fluorescence images of the Laurdan-labeled cells were acquired using an inverted microscope (Eclipse TE2000-U, Nikon, Japan) with a ×60 water-immersion objective (Plan Apo VC 60×, NA = 1.2, Nikon, Japan). A Ti-sapphire laser (Chameleon Vision II, Coherent, USA) with a repetition rate of 80 MHz and a pulse width of 140 femtoseconds (fs) was used as the excitation source. The laser wavelength was optimized and tuned to a peak of 780 nm, and the power was adjusted to 100-200 mW. The group delay dispersion (GDD) was set to 14,000 femtosecond squared (fs^2). Laurdan emission from the cell samples was filtered through 436/20 nm (blue) and 495/25 nm (cyan) bandpass filters. The fluorescence intensity from the two channels was detected using a laser-scanning fluorescence detector (D-Eclipse C1, Nikon, Japan). Two-photon microscopy images of the Laurdan-stained cell membranes were analyzed using ImageJ software (ImageJ 1.53t). Laurdan *GP* images were generated by calculating the *GP* value for each pixel. The *GP* value (GP_m) for each pixel was calculated according to the following equation:

$$GP_m = \frac{I_{blue} - \left(G_{Laurdan} \times I_{cyan}\right)}{I_{blue} + \left(G_{Laurdan} \times I_{cyan}\right)} \qquad Eq.(4-2)$$

In this equation, I_{blue} is the fluorescence intensity of the blue channel and I_{cyan} is the fluorescence intensity of the cyan channel; $G_{Laurdan}$ is the Laurdan calibration factor (*G* factor).

The $G_{Laurdan}$ is mainly influence by the relative sensitivities of the photomultiplier tubes (PMTs) of two channels. In this study, Laurdan (100 μM) in DMSO was used as the reference solution for calibration. Laurdan (100 μM in DMSO) fluorescence spectrum in reference solution was measured using fluorescence spectrometer (FP-8500, Jasco, Japan) with an excitation light of 345 nm wavelength. and the calibration factor (G-factor) was calculated according to the following equation:

$$GP_r = \frac{(I_{440} - I_{490})}{(I_{440} + I_{490})} \qquad Eq.(4-3)$$

where I_{440} and I_{490} represent the Laurdan fluorescence intensity at wavelengths of 440 nm and 490 nm, respectively.

The reference solution was imaged using two-photon microscopy, and the fluorescence images of the blue and cyan channels were obtained, and the Laurdan calibration factor ($G_{Laurdan}$) was calculated according to the following equation:

$$G_{Laurdan} = \frac{I_{blue} \times (1 - GP_r)}{I_{cyan} \times (1 + GP_r)} \qquad Eq.(4-4)$$

Where I_{blue} is the is the Laurdan fluorescence intensity of the blue channel and I_{cyan} is the Laurdan fluorescence intensity of the cyan channel;

The *GP* values of pixels were obtained using image J software and the *GP* histograms were deconvoluted using Origin software (Origin 2023 v.10.0.). For blank control group and each treatment group (including each liposome formulation and free 2-OHOA), 3 replicate plates of cell samples were stained with Laurdan and imaged. 3 to 5 images were obtained from each plate of cells, with each image generated by averaging 4 scanning frames.

2.5. LipiORDER Staining and Imaging

LipiORDER was dissolved in DMSO to a concentration of 10 μM as a stock solution. Cells cultured in 35 mm Φ glass-bottom dishes were carefully washed with D-PBS, followed by incubation with 300 nM LipiORDER in D-PBS for 15 minutes. After the staining period, the cells were rinsed with D-PBS and subsequently examined using fluorescence microscopy (BX53, Olympus, Japan) equipped with image-splitting optics (W-View Gemini A12801-01, Hamamatsu, Japan). For excitation, a light filter with a wavelength of 388/38 nm was used. The emitted light was directed through a dichroic mirror, separating it into green and red channels: green (510/84 nm) and red (>570 nm). Images from both the green and red channels were captured with an exposure time of 200 ms. The ratiometric analysis of LipiORDER fluorescence images was performed using ImageJ software (ImageJ 1.53t). The backgrounds of the green and red channel images were first subtracted, and the R/G ratio images were generated by calculating the fluorescence intensity ratio between the red channel image and the green channel image, according to the following equation:

$$R/G\ ratio = \frac{I_{Red}}{I_{Green}} \qquad Eq(4-5)$$

In this equation, the I_{Red} is the LipiORDER fluorescence intensity from red channel, the I_{Green} is the LipiORDER fluorescence intensity from green channel. For blank control group and each treatment group, 3 plates of cell samples were stained with Laurdan for fluorescence microscopy imaging. 3 to 5 images were obtained from each plate of cells (exposure time of 200 ms).

3. Results and Discussion

3.1. TPM Visualization of the Heterogeneity in Cellular Plasma Membrane Polarity

Different cell types exhibit distinct membrane fluidity characteristics, which can be effectively analyzed using Laurdan generalized polarization (*GP*) quantification. The *GP* value serves as an indicator of membrane fluidity, with higher values reflecting more ordered lipid regions and lower values indicating increased fluidity. As shown in **Fig. 4-1**, all cell lines exhibited heterogeneous *GP* distributions, reflecting a combination of ordered (higher *GP* values) and fluidic (lower *GP* values) membrane regions. For example, the average *GP* value for HepG-2 cell membranes was approximately 0.32, whereas NP-8 cell membranes had a lower average *GP* value of about 0.2, indicating greater overall membrane fluidity. Notably, regions with higher *GP* values, associated with more ordered membrane structures, were predominantly observed at cell-cell junctions and along the cell periphery, suggesting membrane condensation in these areas.

Laurdan fluorescence signals acquired through two-photon microscopy revealed a variety of pixel populations, corresponding to distinct membrane environments. To facilitate quantitative analysis and comparison, the *GP* values of individual pixels were normalized and represented as histograms, termed *GP* histograms. The pixel count at each specific *GP* value reflects the relative area of membrane regions with corresponding fluidity. These histograms provided a comparative overview of membrane polarity variations across different cell types. In most cases, the *GP* histograms displayed a peak distribution resembling a Gaussian curve.

To further investigate membrane heterogeneity, the *GP* histograms were deconvoluted to separate overlapping pixel populations. This analysis provided a more detailed understanding of the distinct lipid environments within the cell membrane, as reported by Gaus et al. (2003). The deconvoluted *GP* histograms revealed two Gaussian distributions (**Fig. 4-1**): one low-*GP* peak (red curve) corresponding to more fluidic membrane regions (depicted in green in the *GP* images), and one high-*GP* peak (blue curve) corresponding to more ordered, rigid membrane regions (depicted in orange). This deconvolution approach offers a clearer view of the membrane's structural complexity, enabling precise interpretation of lipid phase behavior variations across different cellular environments.

Typically, the *GP* histogram of NP-8 cells (ranging approximately from −0.5 to 0.8) displayed a broader distribution compared to HepG-2 cells (around −0.1 to 0.8). This broader range of pixel *GP* values in NP-8 cells indicates greater diversity in cell membrane fluidity relative to HepG-2 cells. Both NP-8 and HepG-2 cells exhibited a similar distribution at low-GP peaks (when comparing the full width at half maximum, FWHM), suggesting the presence of predominantly fluidic membranes, as indicated by the high coverage of green pseudo-color regions in the *GP* images. The low-*GP* peaks of NP-8 cell membranes were centered at 0.116 ± 0.015, whereas those of HepG-2 cells were centered at 0.279 ± 0.030. Concerning the high-*GP* peaks, NP-8 showed a center at 0.481 ± 0.24, and HepG-2 cells showed a center at 0.500 ± 0.058, with no significant difference between the two. Furthermore, no statistically significant difference in high-*GP* region coverage (calculated based on the area under the curve, AUC) was observed between NP-8 (20.54 ± 6.98%) and HepG-2 (22.32 ± 7.20%) cells. These findings suggest that the difference in membrane fluidity between NP-8 and HepG-2 cells is primarily attributed to variations in the fluidic membrane (*Ld*) regions, rather than in the ordered membrane (*Lo*) regions.

Laurdan two-photon microscopy revealed heterogeneous membrane fluidity among cell membranes, and distinct characteristics between NP-8 and HepG-2 cells. The higher membrane fluidity and heterogenicity observed in the NP-8 cell membrane can be attributed to a significantly lower sphingomyelin (SM) content in glioma cell membranes, as reported in previous studies. SM interacts favorably with cholesterol and establishes the co-localization of SM and cholesterol in cell plasma membranes. The formed SM/cholesterol-rich domains are more ordered than the surrounding phase in biological membranes. SM could also reduce the lateral heterogeneity in cholesterol-containing membranes. Specifically, unsaturated SM is able to accommodate both phosphorylcholine and cholesterol, forming a single phase, and maintaining membrane lipids in a homogeneous phase. The reduced level of SM in glioma cells is considered be associated with its higher membrane fluidity and lateral heterogenicity.

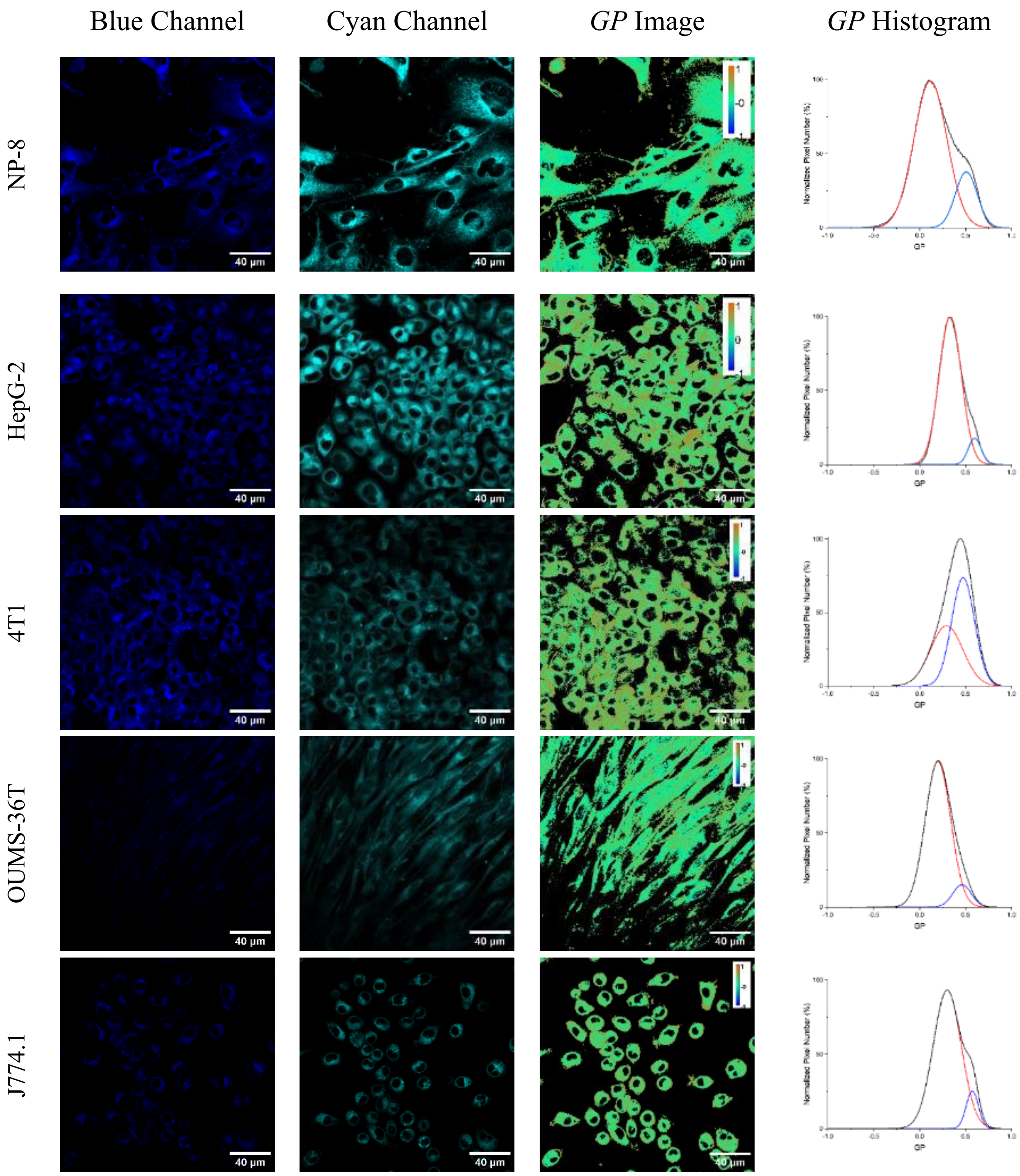

Figure 4-1. Two-Photon Microscopy Laurdan *GP* Images and *GP Hi*stograms of Different Cells. From left to right, the first column displayed the Laurdan fluorescence images of blue channel (436/20 nm); the second column displayed the Laurdan fluorescence images of cyan channel (495/25 nm); the third columns display the pseudo-colored *GP* images; and, the fourth column displayed the pixel *GP* histograms obtained from the corresponding *GP* images. In the *GP* images, the orange represents maximum *GP* (1.0) and pure blue represents minimum *GP* (−1.0). Scale bars represent 40 μm. In the *GP* histograms, the distribution of pixel-*GP* was deconvoluted by fitting two Gaussian distributions (blue and red lines) to the experimental data (black line).

3.2. Investigating the Impact of 2-OHOA-embedded LNPs on Cell Membranes

2-OHOA has attracted considerable attention as a membrane lipid therapy (MLT) agent for cancer treatment due to its ability to modulate membrane lipid composition. However, in the context of anti-cancer drug development, 2-OHOA faces two critical challenges: poor water solubility and suboptimal therapeutic efficacy. To address these limitations, this study aimed to enhance the solubility and therapeutic potential of 2-OHOA by incorporating it into a LNP drug delivery system. While 2-OHOA's broader potential in MLT is recognized, its specific effects on the biophysical properties of cancer cell membranes, particularly membrane fluidity and lipid packing, have not been sufficiently explored. Therefore, this study focused on investigating how 2-OHOA alters cancer cell membrane characteristics before and after treatment. Considering the clinical application focus of 2-OHOA on glioma, also, most LNPs would be accumulated in liver organ post injection, this study utilized both glioma cell (NP-8) and liver cancer cell (HepG-2) as model cells.

To develop an effective delivery vehicle, LNP formulations were designed using DOPC lipids. Before attributing any observed membrane changes to 2-OHOA, it was necessary to rule out potential confounding effects from DOPC itself. HepG-2 and NP-8 cells were treated with varying concentrations of DOPC-only LNPs, and their membrane fluidity was monitored over a 48-hour period using Laurdan GP measurements and fluorescence spectrometry, as shown in **Fig. 4-2-A**. Even at concentrations as high as 500 μM and treatment durations extending to 48 hours, DOPC-only LNPs induced no significant changes in the *GP* values of either HepG-2 or NP-8 cell membranes. These findings were further supported by two-photon microscopy images of Laurdan-stained cells (**Fig. 4-2-B, C**), which showed no detectable alterations in membrane fluidity.

These results confirmed that DOPC lipids, as the structural components of the LNP formulation, had minimal impact on membrane fluidity in the tested cancer cell lines. Consequently, the observed changes in membrane properties during subsequent experiments could be confidently attributed to 2-OHOA rather than the DOPC vehicle. Thus, 2-OHOA was considered the primary factor influencing cancer cell membrane fluidity in this study.

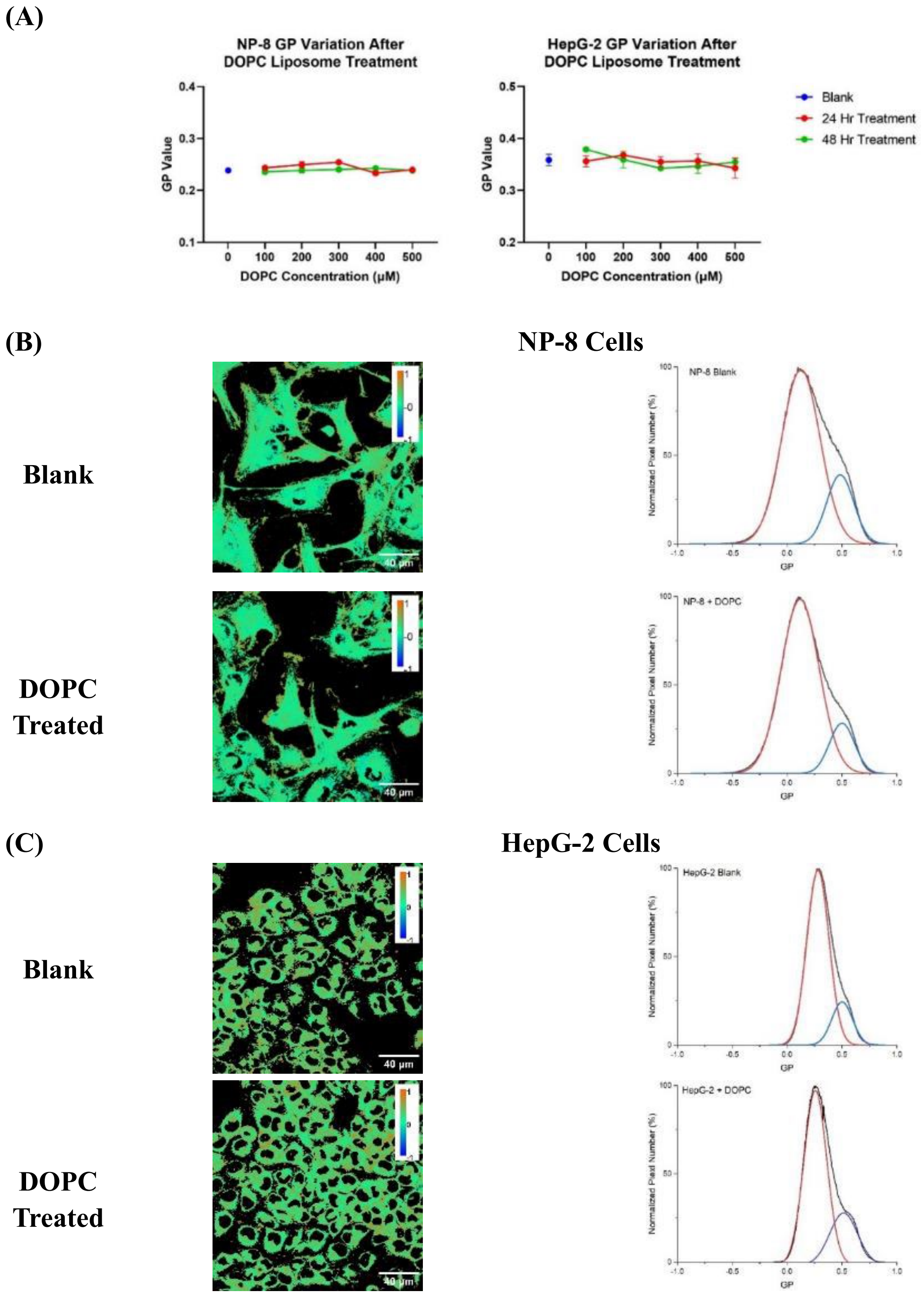

Figure 4-2. Influence of DOPC LNPs treatment on the HepG-2 and NP-8 cell membrane *GP* variations. (A) NP-8 and HepG-2 Laurdan *GP* variations after DOPC LNPs treatments for 24/48 h, *GP* values were obtained from fluorescence spectrometer. Error bars represent ± standard deviations, *n*=3. (B) *GP* images and *GP* histograms of NP-8 cells with and without DOPC LNPs treatments. (C) *GP* images and *GP* histograms of HepG-2 cells with and without DOPC LNPs treatments. Cells were treated with 100 μM DOPC LNPs for 24 h. Images were obtained at 37 ℃. Scale bars represent 40 μm.

Following a 24-hour treatment with 2-OHOA-embedded LNPs (containing 100 µM 2-OHOA) or free 2-OHOA (100 µM), distinct regions with high *GP* values (depicted in orange) appeared in both NP-8 and HepG-2 cell membranes, as shown in **Fig. 4-3-A**. The average *GP* values for cell membranes are summarized in **Fig. 4-3-B**. Notably, NP-8 cells exhibited a more pronounced increase in average *GP* values compared to HepG-2 cells, indicating a greater impact of 2-OHOA on the NP-8 cell membrane. Analysis of normalized pixel GP histograms revealed distinct patterns of *GP* value elevation in the membranes of HepG-2 and NP-8 cells. As shown in **Fig. 4-3-C**, the *GP* histograms of NP-8 cells displayed a significant rightward shift after treatment, while the *GP* histograms of HepG-2 cells showed a more subtle shift.

After deconvolving the *GP* histograms, the low-*GP* peak centers are summarized in **Fig. 4-3-D**. The shifting pattern of the low-*GP* peak reflects variations in high-fluidity membrane regions. In NP-8 cells, the *GP* histograms exhibited a marked rightward shift after treatment. Additionally, as shown in **Table 4-1**, the high-GP peak centers increased slightly, accompanied by a significant rise in high-*GP* coverage, indicating an abundance of ordered membrane regions. These findings suggest that 2-OHOA-embedded LNPs treatment led to a notable reduction in fluidity within the high-fluidity (*Ld*) membrane regions of NP-8 cells and an increase in membrane areas with liquid-ordered (*Lo*) characteristics. In contrast, after 2-OHOA-embedded LNPs treatment, HepG-2 cells exhibited a subtle rightward shift in both low-*GP* and high-*GP* peaks, but without a significant increase in high-*GP* coverage. The variations in *GP* values were more moderate in HepG-2 cells compared to NP-8 cells. When comparing the effects of different LNPs formulations, the 9-1 LNPs induced the most significant increase in average *GP* values (from ~0.2 to ~0.43) and the most pronounced shift in the low-*GP* peak center (from ~0.12 to ~0.32) in NP-8 cells. The 5-5 LNPs, on the other hand, induced a slightly higher average *GP* increase in HepG-2 cells compared to other formulations.

(A)

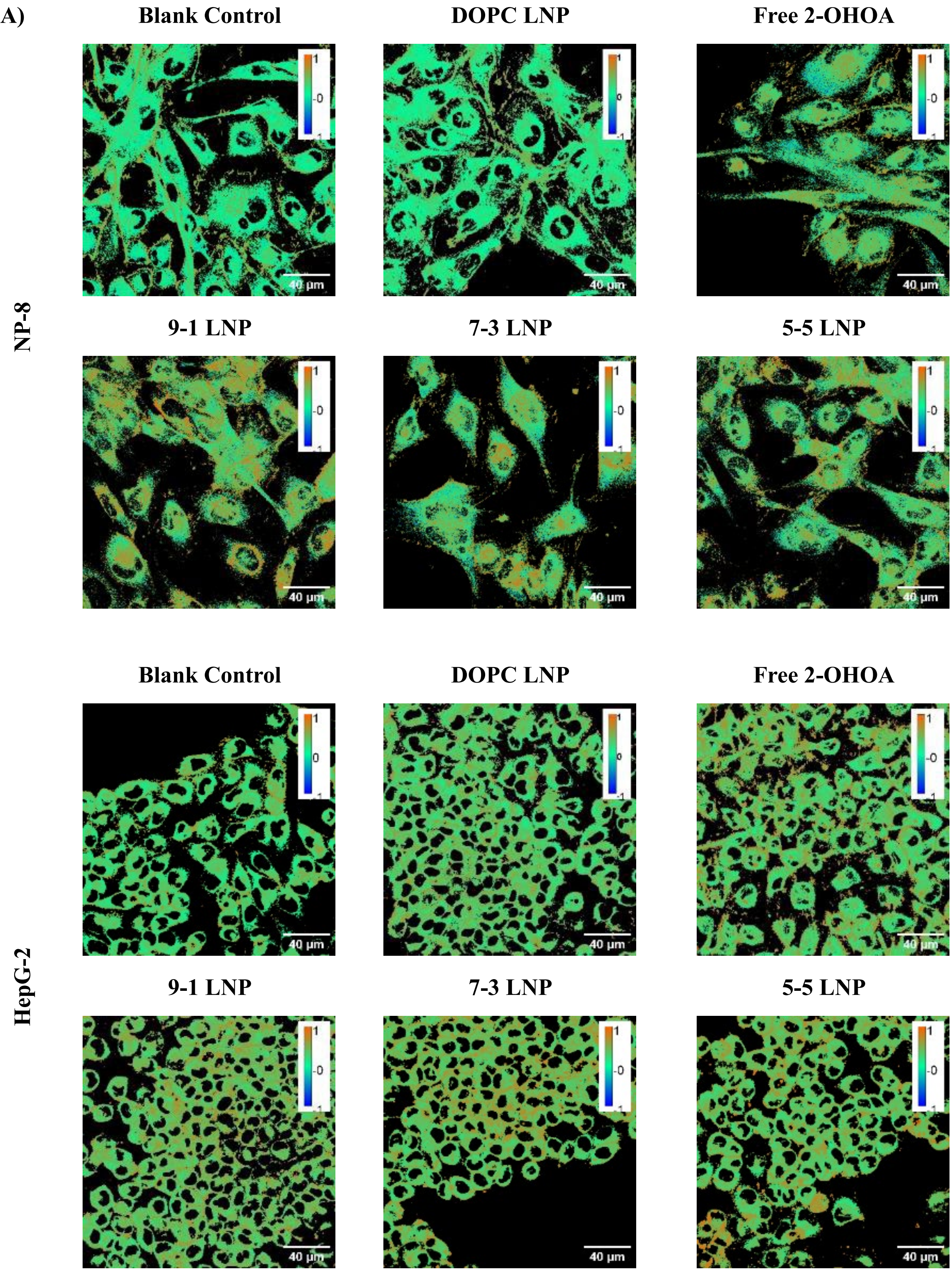

Blank Control

DOPC LNP

Free 2-OHOA

9-1 LNP

7-3 LNP

5-5 LNP

Blank Control

DOPC LNP

Free 2-OHOA

9-1 LNP

7-3 LNP

5-5 LNP

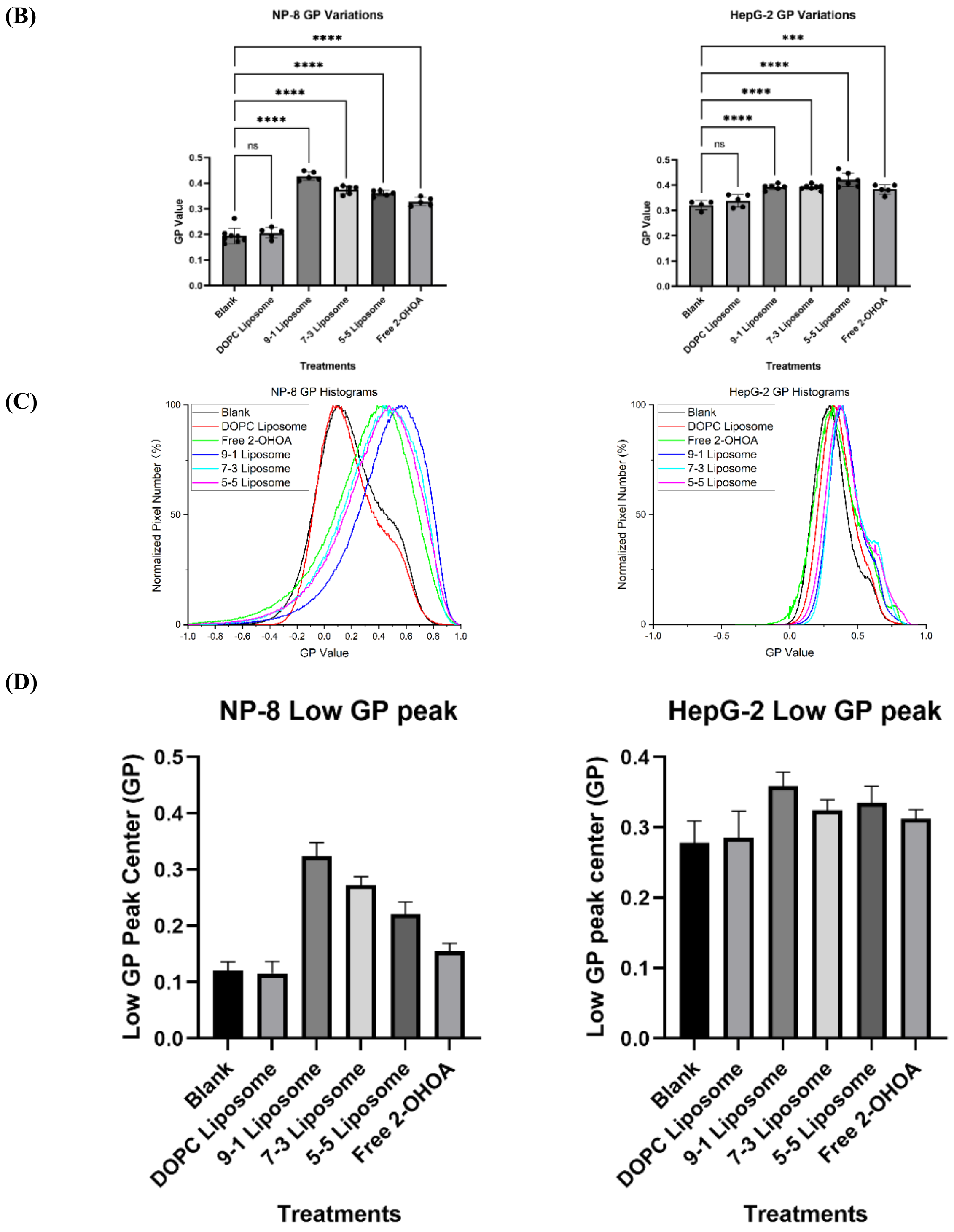

Figure 4-3. Laurdan Two-Photon Microscopy Imaging Results of 2-OHOA/DOPC LNP Treated Cells: (A) *GP* images of NP-8 cells and HepG-2 cells with and without treatments. Scale bars represent 40 μm. **(B)** Average *GP* values calculated from the *GP* images. **(C)** *GP* histograms obtained from the *GP* images. **(D)** Summarized low-*GP* peak centers of deconvoluted results before and after treatment. In treatment groups, cells were incubated for 24 h with either 100 μM DOPC, 2-OHOA-embedded LNPs containing 100 μM 2-OHOA or 100 μM free 2-OHOA. Error bars represent ± *s.d*, (n = 4–8). *ns*: no significant difference; ***: $p < 0.001$; ****: $p < 0.0001$.

Table 4-1. Two Gauss Distributions of Deconvoluted *GP* Histograms

Cell	Treatment	Low *GP* Peak center	FWHM 1	High *GP* Peak center	FWHM 2	High *GP* coverage (%)
NP-8	Blank	0.116 ± 0.015	0.394 ± 0.048	0.481 ± 0.024	0.291 ± 0.023	20.54 ± 6.98
	DOPC LNP	0.128 ± 0.041	0.427 ± 0.112	0.476 ± 0.043	0.336 ± 0.044	24.25 ± 9.18
	9-1 LNP	0.310 ± 0.037	0.630 ± 0.021	0.596 ± 0.028	0.406 ± 0.027	50.49 ± 6.43
	7-3 LNP	0.266 ± 0.022	0.679 ± 0.018	0.578 ± 0.021	0.414 ± 0.027	45.27 ± 2.68
	5-5 LNP	0.223 ± 0.023	0.678 ± 0.014	0.531 ± 0.026	0.447 ± 0.016	52.95 ± 3.00
	Free 2-OHOA	0.155 ± 0.015	0.710 ± 0.019	0.475 ± 0.008	0.487 ± 0.012	58.93 ± 1.88
HepG-2	Blank	0.279 ± 0.030	0.237 ± 0.011	0.500 ± 0.058	0.277 ± 0.060	22.32 ± 7.20
	DOPC LNP	0.285 ± 0.038	0.244 ± 0.016	0.524 ± 0.058	0.251 ± 0.063	21.67 ± 10.11
	9-1 LNP	0.359 ± 0.020	0.295 ± 0.027	0.593 ± 0.007	0.217 ± 0.015	27.80 ± 7.01
	7-3 LNP	0.325 ± 0.015	0.323 ± 0.056	0.609 ± 0.026	0.261 ± 0.022	22.63 ± 2.13
	5-5 LNP	0.335 ± 0.024	0.297 ± 0.021	0.589 ± 0.003	0.221 ± 0.019	26.07 ± 4.08
	Free 2-OHOA	0.313 ± 0.013	0.296 ± 0.019	0.594 ± 0.022	0.243 ± 0.019	25.03 ± 4.71

NP-8 and HepG-2 cells were imaged at 37°C. For the treatment groups, cells were incubated for 24 h with media containing DOPC LNPs (100 μM), 2-OHOA-embedded LNPs (containing 100 μM 2-OHOA) or free 2-OHOA (100 μM). For blank control group and each treatment group, 3 replicate plates of cell samples were stained with Laurdan and imaged. 3 to 5 images were obtained from each plate of cells, with each image generated by averaging 4 scanning frames. The obtained *GP* histograms of *GP* images, were deconvoluted into two Gauss distributions. The peak center, full width at half maximum (FWHM), and percentage of pixels associated with high *GP* peak (High *GP* coverage) were averaged over 5-8 images.

To assess the enhancement of LNP formulations, variations in the Laurdan *GP* of cell membranes after formulated and non-formulated 2-OHOA treatments were measured using a fluorescence spectrometer. The 9-1 LNP was selected as the optimized formulation for NP-8 cells, and the 5-5 LNP was selected for HepG-2 cells. Cells were incubated with varying concentrations of 2-OHOA-embedded LNPs or free 2-OHOA for 24 hours, and the *GP* variation results are shown in **Fig. 4-4**. Generally, the *GP* elevation in cell membranes followed a 2-OHOA dose-dependent pattern. The LNPs formulations induced a more pronounced *GP* increase in both NP-8 and HepG-2 cells, consistent with the two-photon microscopy results, reaffirming the enhancement of 2-OHOA performance after LNP formulation.

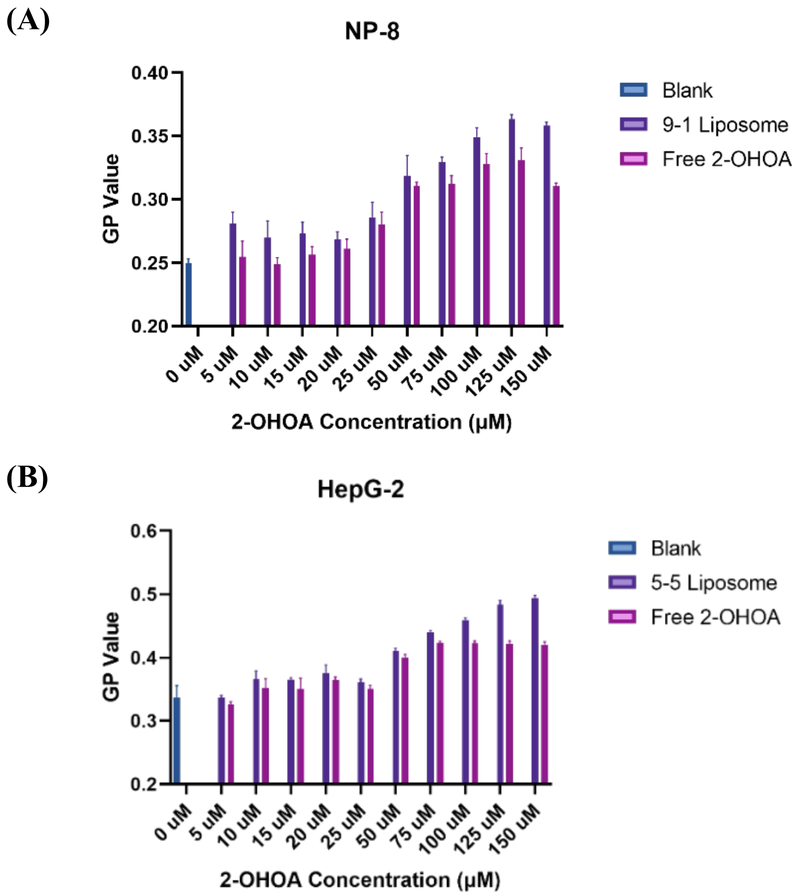

Figure 4-4. Comparation of the influence of LNP formulation and free 2-OHOA on the cell membrane *GP* value variations. **(A)** NP-8 cell *GP* values after 24 h treatment using 9-1 LNPs and free 2-OHOA at different concentrations; **(B)** HepG-2 cell *GP* values after 24 hours treatment using 5-5 LNPs and free 2-OHOA at different concentrations. the *GP* values were obtained using fluorescence spectrometer (measured at 37°C, excitation wavelength was set at 340 nm, emission spectra were collected from 400 to 600 nm), *GP* values were calculated according to the equation described in experimental section. Error bars represent ± *s.d.* (*n*=3–5)

It is noteworthy that lipid droplets (LDs) were abundant in HepG-2 cells following treatment with 2-OHOA-embedded LNPs or free 2-OHOA. The LDs were stained with Lipi-Red, a fluorescence probe designed for lipid droplet visualization, and observed using fluorescence microscopy (**Fig. 4-5-A**). A marked accumulation of LDs was observed in HepG-2 cells after 2-OHOA treatment, a phenomenon not observed in NP-8 cells. Similar observations have been reported in specific cell lines exposed to 2-OHOA (Terés, S et al., 2012). This may be attributed to the structural similarity between 2-OHOA and oleic acid (OA), both of which belong to the monounsaturated omega-9 fatty acid class. Excessive influx of OA into HepG-2 cells appears to trigger interactions between LDs and mitochondria, promoting LD growth, a similar effect observed with 2-OHOA. Notably, the lipid droplets attached to the plasma membranes of HepG-2 cells exhibited very high *GP* values (ranging from 0.5 to 0.8), contributing to the elevated *GP* values seen in HepG-2 cells after treatment (**Fig. 4-3-C**). This explains the observed increase in the GP histograms of HepG-2 cells around a GP value of ~0.6 after 2-OHOA treatment (**Fig. 4-5-B**), which is attributed to the abundance of LDs.

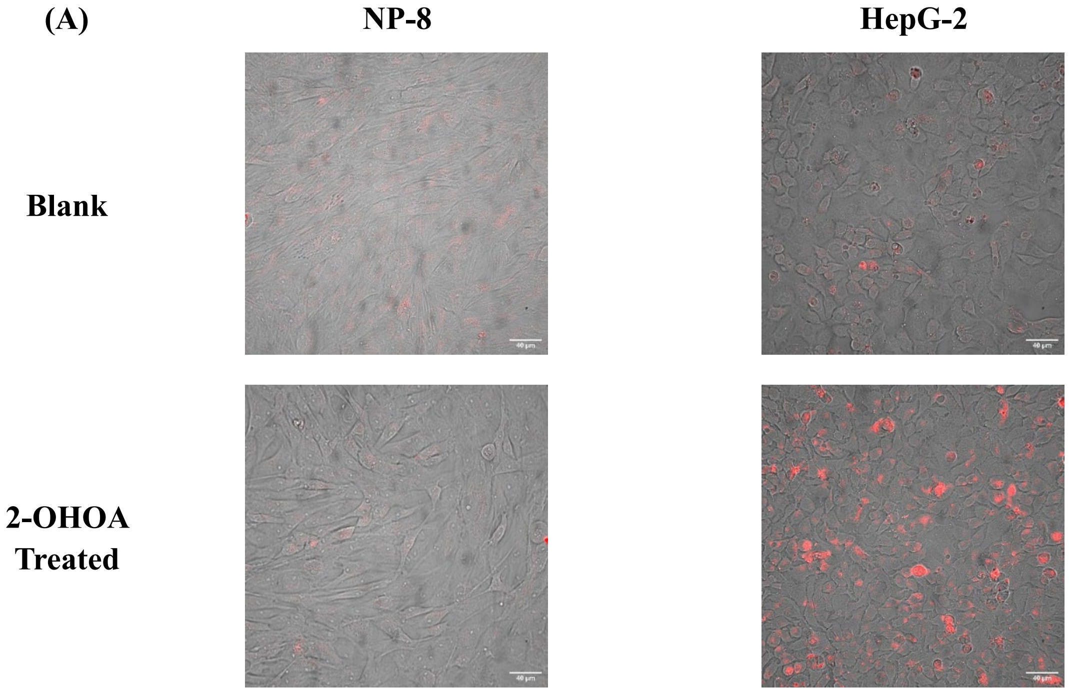

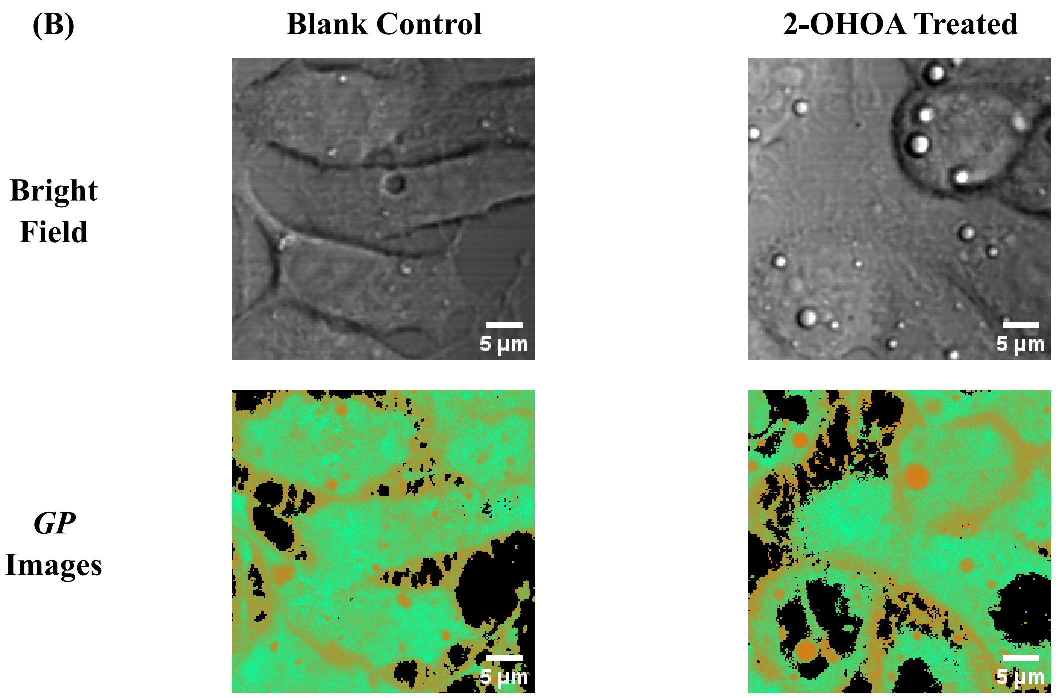

Figure 4-5. Lipid Droplets Images. (A) Fluorescence microscopy images of Lipi-Red stained NP-8 and HepG-2 cells. The shown images are merged from bright field image and red channel image. Magnification was 40 times. Scarle bars represent 40 µm. **(B)** Bright field and *GP* images of HepG-2 with and without 2-OHOA treatments, scale bars represent 5 µm. For the treatment group, cells were incubated with 100 µM 2-OHOA for 24 h before staining and imaging.

In conclusion, Laurdan two-photon microscopy proves to be a valuable tool for visualizing changes in cell membrane fluidity. Treatment with 2-OHOA significantly increased Laurdan *GP* values in both NP-8 and HepG-2 cells, with NP-8 cells displaying greater sensitivity. The distinct patterns of GP value elevation highlight the differential responses of NP-8 and HepG-2 cells to 2-OHOA treatment. The reduction in NP-8 membrane fluidity is associated with an overall decrease in plasma membrane fluidity, while HepG-2 cells exhibited a reduction in fluidity along with an accumulation of lipid droplets. Furthermore, LNP formulation enhanced the effects of 2-OHOA on both NP-8 and HepG-2 cells, leading to more pronounced alterations in *GP* values.

3.3. LipiORDER staining and investigation

To further validate alterations in cell membrane lipid packing following treatment, this study used another solvatochromic fluorescence probe, LipiORDER, to visualize changes in lipid packing states. LipiORDER, when incorporated into the cell membrane, senses lipid packing and exhibits a fluorescent color shift, transitioning from green in liquid-ordered (*Lo*) membrane regions to red in liquid-disordered (*Ld*) regions. The lipid packing status of the cell membrane can be quantified and compared by calculating the LipiORDER red/green fluorescence intensity (R/G) ratio. **Fig. 4-6-A, B** show the pseudo-colored R/G ratio images of NP-8 and HepG-2 cells before and after treatment. The average R/G ratios are summarized in **Fig. 4-6-C**.

While both Laurdan *GP* values and LipiORDER R/G ratios provide insights into membrane properties, they measure complementary aspects rather than the same characteristic. By understanding both the *GP* value and R/G ratio, this study gains a more comprehensive view of membrane characteristics, including fluidity and lipid packing order. Correlation analysis between the variations in *GP* values and R/G ratios before and after 2-OHOA treatments (summarized in **Fig. 4-6-D**) revealed a linear relationship, confirming the proportional connection between cell membrane fluidity/polarity and lipid packing.

Initially, both HepG-2 and NP-8 cells displayed heterogeneous plasma membrane lipid packing (**Fig. 4-6-A, B**), with *Lo* (green) and *Ld* (red) phases present. NP-8 cells exhibited generally more disordered lipid packing than HepG-2 cells. Treatment with DOPC-only LNPs did not induce noticeable changes in average R/G ratios. However, following 2-OHOA treatment (formulated or non-formulated), significant decreases in R/G ratios were observed in both cell types, indicating an increase in membrane lipid packing. NP-8 cells showed an abundance of *Lo* phase at the plasma membrane after 2-OHOA treatment (**Fig. 4-6-A**), while HepG-2 cells displayed a reduced R/G ratio in the plasma membrane, accompanied by a marked green region in the cytoplasm (**Fig. 4-6-B**), associated with abundant lipid droplets stained by LipiORDER. As previously mentioned, 2-OHOA treatment induced significant lipid droplet accumulation in HepG-2 cells, but not in NP-8 cells. These lipid droplets exhibit intense green fluorescence when stained with LipiORDER (Sot, J. et al., 2021). Notably, fluorescence microscopy captures a thicker section than two-photon microscopy, allowing for detection of more cytoplasmic lipid droplets and resulting in a pronounced decrease in the average R/G ratio.

Analysis of the R/G ratio across various groups (**Fig. 4-6-C**) revealed that LNP-formulated 2-OHOA treatment induced a more significant decrease in R/G ratio compared to non-formulated 2-OHOA. Specifically, the 9-1 LNP induced the most pronounced decrease in NP-8 cells, while the 5-5 LNP induced the greatest reduction in HepG-2 cells. This trend closely aligns with the Laurdan GP results, further confirming that LNP formulation significantly enhanced the effects of 2-OHOA on cancer cells.

In summary, the LipiORDER R/G ratio results complement the Laurdan GP value findings. Treatment with 2-OHOA-embedded LNPs, as well as free 2-OHOA, notably improved lipid packing in cancer cell membranes, effectively reducing cell membrane fluidity. However, distinct patterns of R/G ratio variation were observed in NP-8 and HepG-2 cells. The abundant lipid droplets induced by 2-OHOA treatment significantly contributed to the decreased R/G ratio in HepG-2 cells. Furthermore, different LNP formulations resulted in varying degrees of R/G ratio reduction in both NP-8 and HepG-2 cells. These findings underscore the impact of 2-OHOA on cancer cell membrane lipid packing and suggest that LNP formulations, despite containing the same amount of 2-OHOA, can exert diverse effects on cancer cell membrane properties. In a subsequent study, this study will explore the factors influencing the performance differences among various 2-OHOA-embedded LNP formulations.

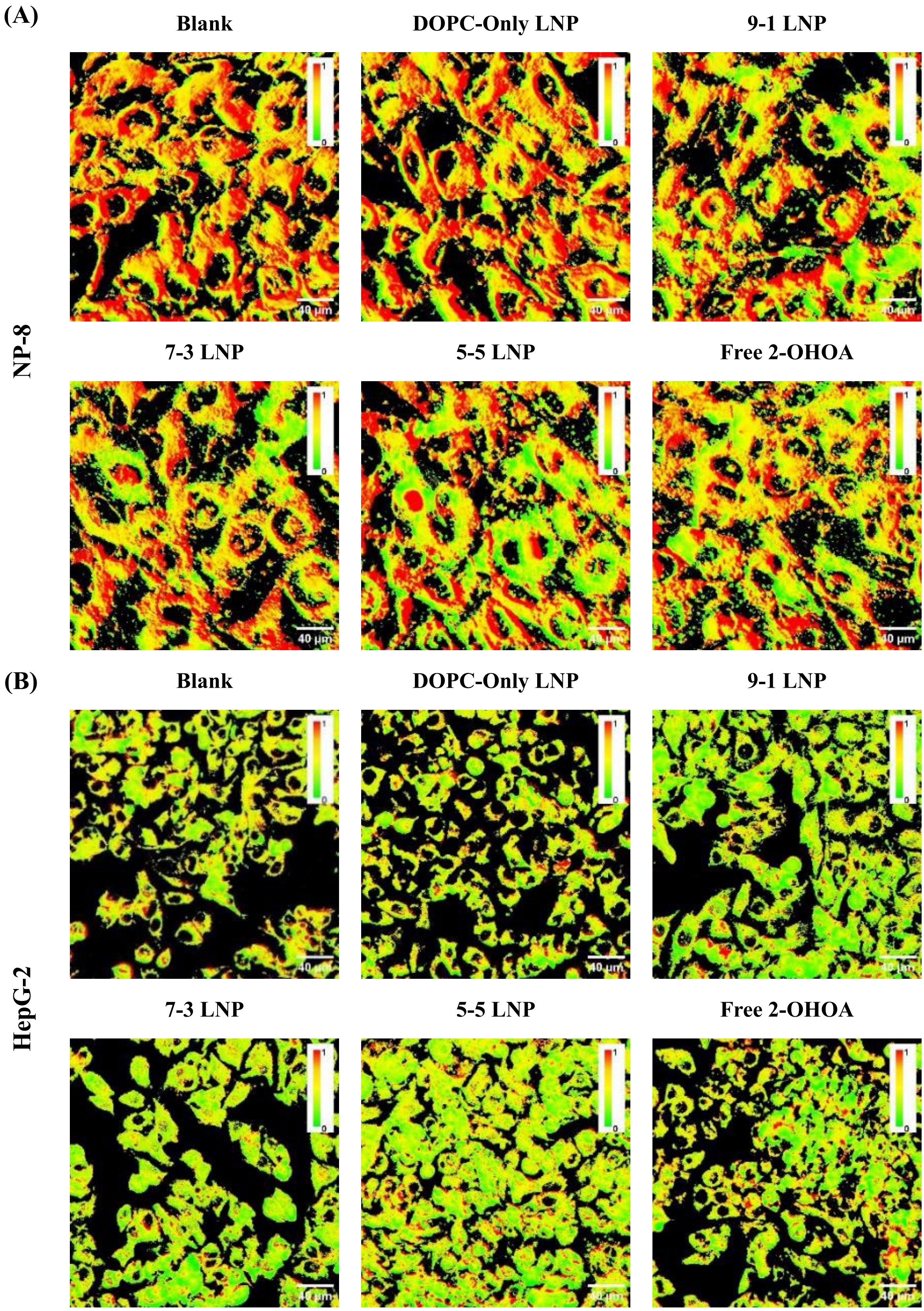
(A)
Blank
DOPC-Only LNP
9-1 LNP
NP-8
7-3 LNP
5-5 LNP
Free 2-OHOA
(B)
Blank
DOPC-Only LNP
9-1 LNP
HepG-2
7-3 LNP
5-5 LNP
Free 2-OHOA
1
0
40 μm

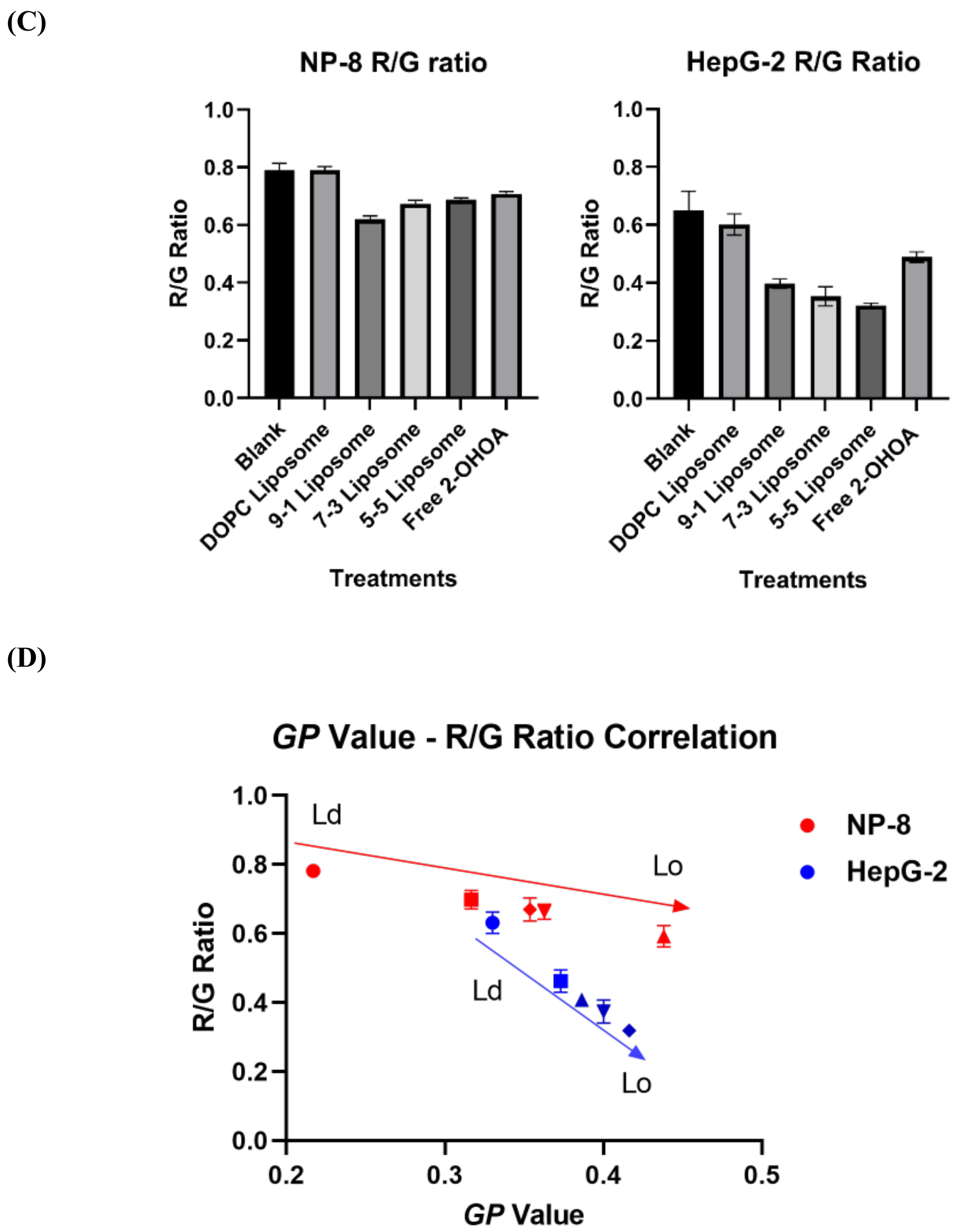

Figure 4-6. LipiORDER R/G Ratio Images of **(A)** NP-8 cells and **(B)** HepG-2 cells before and after treatments, green color represents *Lo* phase (low fluidity), and red color represents *Ld* phase (high fluidity), magnification is 40 times; Scar bar = 40 µm. **(C)** Summarized R/G ratio results of acquired images, error bars represent ± *s.d*, *n*=5. **(D)** The *GP* value - R/G ratio correlations of NP-8 and HepG-2 cells with or without treatments. (●): Blank control; (■): freee-2-OHOA treated; (▲): 9-1 LNP treated; (▼): 7-3 LNP treated; (♦): 5-5 LNP treated. Error bars represent ± *s.d*, *n*=3. In treatment groups, cells were incubated for 24 h with 100 µM DOPC, 2-OHOA-embedded LNPs containing 100 µM 2-OHOA or 100 µM free 2-OHOA.

3.4. Cellular internalization efficacy and endocytic mechanism

Considering the diverse effects induced by various LNP formulations on cell membrane fluidity, this study hypothesizes that differences in cellular internalization efficacy and uptake mechanisms may contribute to the variations observed in 2-OHOA performance (as illustrated in **Fig. 4-7**). The efficiency of nanoparticle (NP) internalization and endocytic mechanisms depends on several factors, including the physicochemical and surface properties of the nanoparticles (Behzadi, S. et al., 2017). Importantly, different cell types may employ distinct endocytic pathways for internalizing the same nanoparticles (Xia, T., et al., 2007). Therefore, to enhance the drug delivery efficacy of 2-OHOA, it is crucial to evaluate both the cellular internalization efficiency and the underlying endocytic mechanisms.

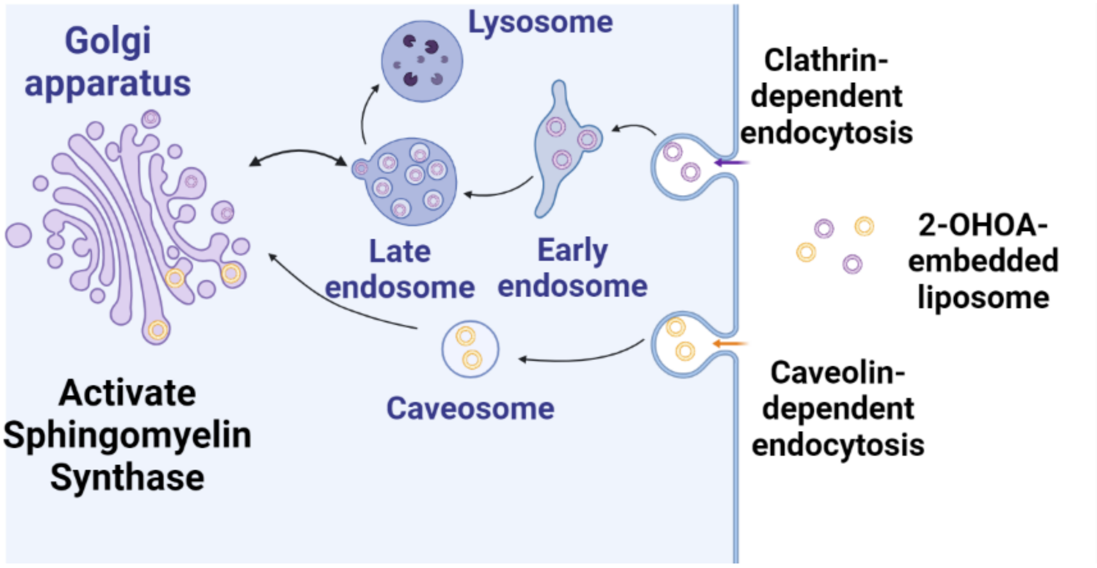

Figure 4-7. Schematic illustration depicts a hypothetical scenario of the endocytosis process of 2-OHOA-embedded LNPs, enhancing the impact of 2-OHOA on cancer cells.

The results of cellular internalization efficiency are shown in **Fig. 4-8-A, B**. After 6 hours of incubation, LNPs of different formulations did not exhibit significant differences in cellular internalization efficiency in NP-8 cells. However, in HepG-2 cells, the 5-5 LNPs showed slightly enhanced internalization efficacy, which may contribute to the slightly greater impact of the 5-5 LNPs on these cells. To investigate the endocytic mechanisms of 2-OHOA-embedded LNPs, methyl-β-cyclodextrin (MβCD) was used to inhibit caveolin-mediated endocytosis, and chlorpromazine was used to block clathrin-mediated endocytosis (Un, K., et al., 2012). As shown in **Fig. 4-8-C, D**, the cellular endocytic pathway of LNPs varied depending on the cell type and LNP formulation. In NP-8 cells, LNP internalization was primarily caveolae-dependent. Inhibition of clathrin reduced the internalization of DOPC-only and 9-1 LNPs, but did not affect the uptake of 7-3 and 5-5 LNPs, suggesting that these formulations are not internalized via the clathrin-mediated endocytosis pathway in NP-8 cells. In HepG-2 cells, both DOPC-only and 9-1 LNPs showed a clathrin-dependent internalization pathway. Furthermore, as the ratio of 2-OHOA increased in the LNP formulations, endocytosis-dependent internalization by HepG-2 cells was heightened.

The summarized results, including LNP endocytic ratios and cell membrane GP variations, are presented in **Table 4-2**. Interestingly, despite the previously observed variations in cell membrane fluidity after treatment, the 9-1 LNP induced a more pronounced reduction in membrane fluidity in NP-8 cells compared to the 7-3 and 5-5 LNPs. Meanwhile, the 5-5 LNPs had a stronger impact on HepG-2 cells. Notably, cell GP variations were more significant with an increase in the liposome endocytic ratio. These findings suggest that the endocytosis of 2-OHOA-embedded LNPs enhances the effect of 2-OHOA on cancer cells, leading to a more substantial reduction in cell membrane fluidity.

In the case of caveolae-mediated endocytosis, nanoparticles typically do not fuse with lysosomes upon entering cells; instead, they are directed to the endoplasmic reticulum (ER) or Golgi apparatus, leading to increased drug accumulation in these regions (Kou, L., et al., 2013). 2-OHOA has been identified as a sphingomyelin synthase (SMS) activator, with SMS1 and SMS2 subtypes. While SMS2 is partially localized to the plasma membrane, the majority of SMS enzymes are found in the trans-Golgi network (TGN) rather than in the cytoplasm (Gault, C. R., et al., 2010). The endocytic pathway associated with 2-OHOA-embedded LNPs is thought to facilitate interactions between 2-OHOA and SMS, leading to enhanced sphingomyelin (SM) synthesis and ultimately reducing cell membrane fluidity (GP increase).

These results support the hypothesis that the varying effects of different LNP formulations on cancer cells are related to diverse cellular uptake mechanisms. The endocytic pathway is believed to amplify the impact of 2-OHOA-embedded LNPs on cancer cells.

.

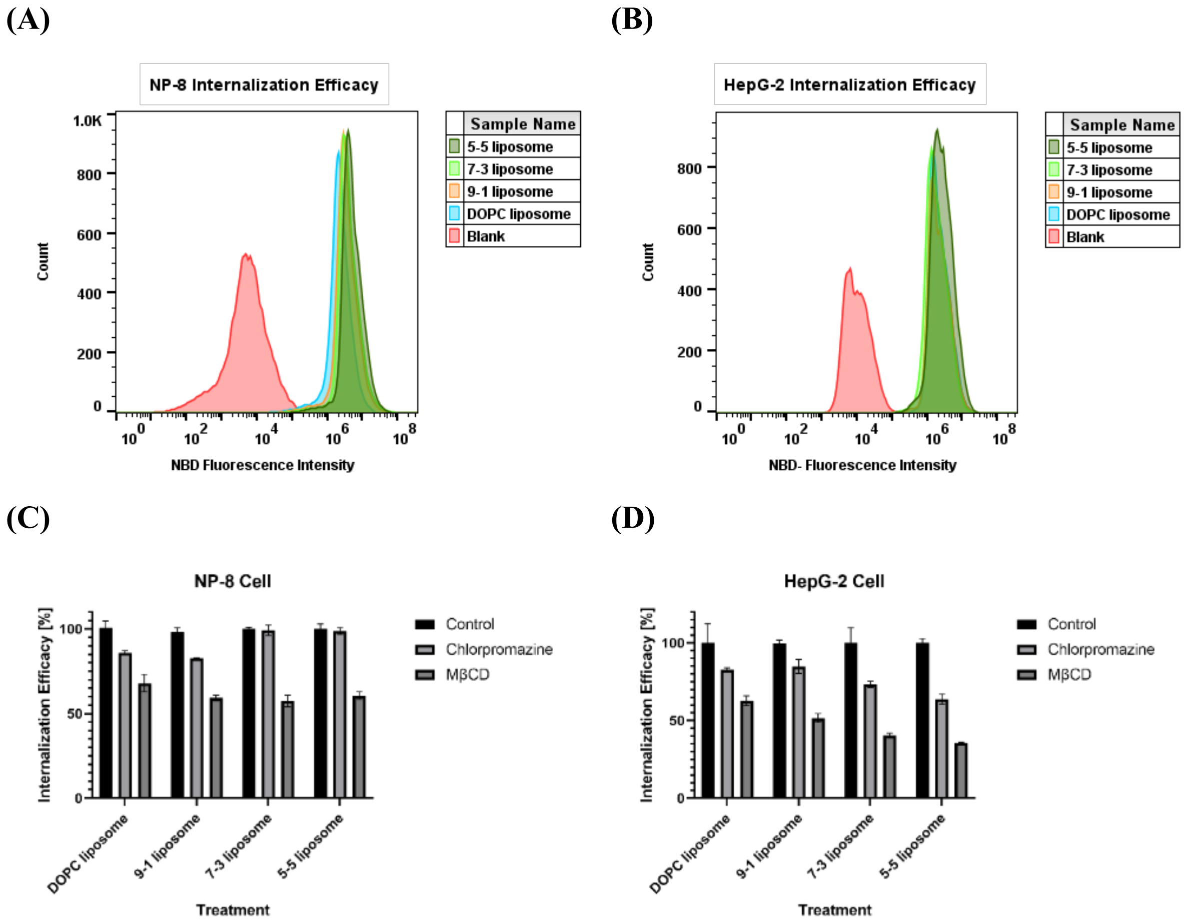

Figure 4-8. Liposome internalization characterization results. (**A, B**) Histograms of NP-8 and HepG-2 cellular internalization efficacy; (**C, D**) NP-8 and HepG-2 internalization efficacy with and without endocytosis inhibitions. Error bars represent ± *s.d* (*n*=3).

Table 4-2. Cell endocytosis ratio and *GP* variations (*n*=3)

Cell Line	Liposome Formulations	Clathrin-mediated endocytosis ratio (%)	Caveolin-mediated endocytosis ratio (%)	*GP* variation (%)
NP-8	9-1	17.3 ± 0.4	40.8 ± 1.69	95.6 ± 2.1
	7-3	0.8 ± 3.1	42.6 ± 3.5	85.6 ± 5.1
	5-5	1.3 ± 2.0	39.3 ± 2.1	65.7 ± 6.1
HepG-2	9-1	15.1 ± 4.4	48.2 ± 2.7	22.7 ± 3.6
	7-3	26.7 ± 1.9	59.7 ± 1.5	23.1 ± 1.6
	5-5	36.1 ± 3.3	64.2± 0.4	35.6 ± 4.7

3.5. Impact of Cubosomes on Macrophage Membrane

Cubosomes have been reported to be internalized by macrophage cells through the phagocytosis mechanism. To track the impact of cubosome internalization on macrophage cell membrane properties, this study aimed to monitor the variation in the membrane GP values of J774.1 cells during a 1-hour incubation with cubosomes.

Figure 4-9 summarizes the time-lapse GP imaging results of J774.1 cells over the 1-hour incubation period. During this time, DOPC LNPs (*La*) did not induce significant changes in the macrophage cell membrane mean-GP values. However, both MO-only cubosomes and cationic cubosomes induced a rapid and significant reduction in mean-GP values on the macrophage membranes, with a dose-dependent effect observed (200-500 μM). This suggests that cubosome internalization alters the macrophage plasma membrane, as cubosomes enter the cells via both phagocytosis and membrane fusion pathways. Based on these results, the membrane fusion pathway is likely the primary mechanism responsible for the observed changes in membrane properties.

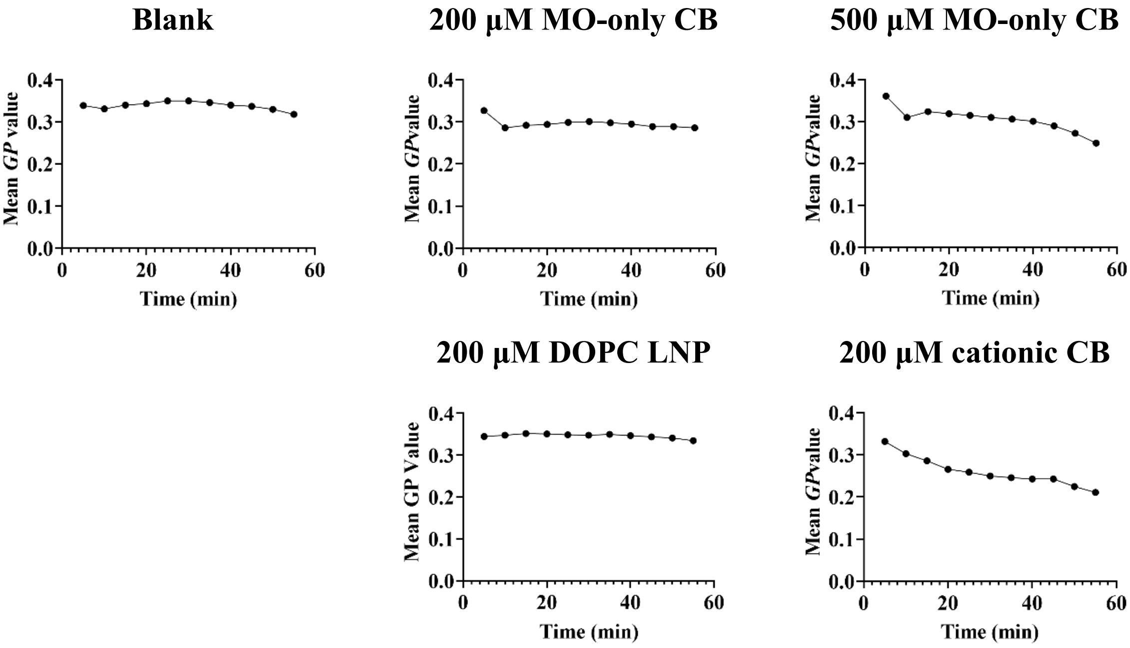

Blank

200 μM MO-only CB

500 μM MO-only CB

200 μM DOPC LNP

200 μM cationic CB

Figure 4-9. Laurdan TPM Time-lapse Results. J774.1 cells were incubated with or without LNPs for 1 hour. Images were acquired at 5-minute intervals. The calculated mean-*GP* values were summarized and plotted as mean *GP*-time plots.

4. Summary

Using Laurdan two-photon microscopy, this study demonstrated that both 2-OHOA and 2-OHOA-embedded LNPs effectively reduced the fluidity of NP-8 and HepG-2 cell membranes. The LNP formulation enhanced the effect of 2-OHOA on membrane fluidity in both cell lines, although distinct patterns of fluidity reduction were observed. These findings were further supported by LipiORDER fluorescence microscopy, which confirmed significant changes in lipid packing within the cell membranes after treatment with 2-OHOA-embedded LNPs.

In this chapter, the investigation extended to cellular internalization and endocytic mechanisms, revealing that the improved performance of 2-OHOA-embedded LNP was dependent on endocytosis. The LNP formulation not only facilitated better cellular uptake of 2-OHOA but also exhibited superior anticancer efficacy compared to the free drug. This suggests that encapsulation enhances its therapeutic potential as a membrane lipid therapy. These results strongly support the hypothesis that the LNP formulation addresses the solubility limitations of 2-OHOA while also amplifying its biological activity. The ability of LNPs to modulate cell membrane properties and improve drug delivery via endocytosis highlights the potential of lipid-based delivery systems to enhance therapeutic outcomes. In addition, this study conducted preliminary research on the impact of cubosomes on macrophage membrane properties, revealing a decrease in membrane polarity upon contact with cubosomes. This phenomenon may be attributed to membrane fusion between cubosomes and the macrophage membrane, highlighting how differences in the internalization mechanisms of LNPs trigger distinct cellular responses.

Future research should focus on optimizing lipid-based nano-drug delivery systems, with particular emphasis on LNP phase behavior, and explore various formulations to enhance efficacy and stability. Additionally, further in vivo studies, especially in animal models, are crucial to understanding the specific endocytic and fusogenic pathways involved, as well as assessing the clinical potential of different LNP formulations.

Chapter 5

Development of Cubosome-Based Biomimetic nano-DDS

1. Introduction

As observed in Chapter 4, MO-based cubosomes (CBs) significantly impacted macrophage cell membrane fluidity, likely due to the rapid fusion between CBs and the cell plasma membrane. Another key challenge with CBs in drug delivery is their structural instability. Upon *in vivo* injection, CBs quickly interact with plasma, leading to their collapse and a burst release of the drug payload. This destabilization severely limits the effective use of CBs for drug delivery.

Nanoparticle recognition by the mononuclear phagocyte system is a major hurdle in nano-drug delivery systems (nano-DDS). To address this, surface modification of CBs is necessary to extend their circulation time and reduce immunogenicity. **Table 5-1** summarizes representative studies on CB surface modifications. Currently, PEGylation is the most commonly used strategy for NP surface modification. PEG coatings shield the nanoparticle surface from aggregation, opsonization, and phagocytosis, thus prolonging systemic circulation time. However, some studies suggest that PEGylation can induce immune responses in animals, highlighting the need for alternative surface modification strategies to improve the efficacy and safety of CB-based nano-DDS.

In recent years, the cell membrane coating strategy has emerged as a promising surface modification platform for nano-DDS. Red blood cell (RBC) membrane-camouflaged nanoparticles, benefiting from the long circulation time of RBCs, have superior circulation half-lives and reduced immunogenicity compared to traditional PEGylated nanoparticles. Similarly, macrophage membrane coatings have been extensively explored for nano-DDS development. These coatings can enhance circulation time, control drug release, promote immune evasion, and reduce immunogenicity due to the inherited membrane proteins. Furthermore, applying a cell membrane layer to nanoparticles has been shown to improve their stability and safety profile over time.

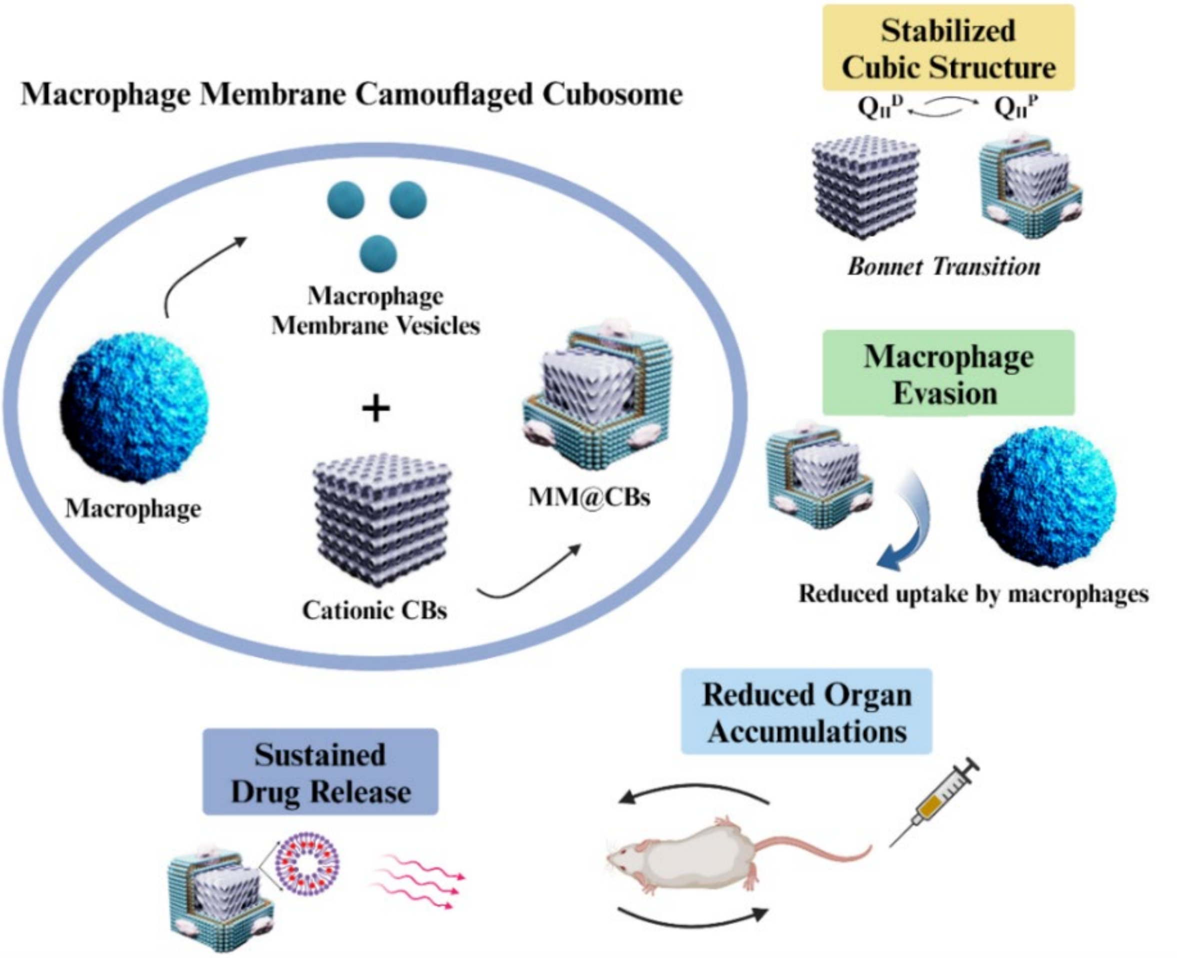

Schematic 5-1. Illustration of this work.

Given the tunable surface of CBs and the multifunctionality of macrophage cell membranes, this study hypothesizes that coating CBs with macrophage cell membranes presents a promising method for enhancing drug delivery performance. The cell membrane coating not only stabilizes the CBs *in vivo*, but also provides stealth properties to evade immune detection, potentially leading to improved therapeutic efficacy and reduced side effects. In this work, the cationic CBs were firstly fabricated by doping 1 mol% DOTAP into monoolein (MO). The positively charged surface of the CBs would facilitate the coating of the negatively charged cell membrane via electrostatic interaction. After the macrophage membrane coating, this nano-DDS was systematically characterized using DLS, cryo-TEM and SAXS. The cell internalization efficacy was investigated using flow cytometry (FCM) and confocal laser scanning fluorescence microscopy (CLSM). The *in vivo* distributions of CBs were investigated. Doxorubicin (DOX) was harnessed as model drug and the anti-cancer efficacy was investigated via apoptosis assay. Our outcomes demonstrated that the prepared cationic CBs could successfully be camouflaged by macrophage membrane and inherit the membrane proteins from macrophages to realize an immune escape without hindering cancer cell uptake efficacy. Furthermore, the macrophage membrane stabilized the CBs in vivo and exhibited reduced accumulations in mice organs including heart, kidney and lungs, indicating a prolonged circulation time span *in vivo*.

Table 5-1. Previous studies about CBs surface modification

Surface Modifier	Modification Material	Function	Ref
Polymer	PEG	Stabilize CBs; Extend the circulation timespan *in vivo*.	B. Angelov et al., 2012 K. L. Von Eckardstein et al., 2005 H. Kim et al., 2018 J. Zhai et al., 2020
	Poly-ε-lysine	Stabilize CBs in serum; Sustain drug release.	S. Deshpande et al., 2014
	Chitosan	Sustain drug release; Enhance bioavailability.	Y. Wei et al., 2019
		Enhancing the immune response for vaccines.	T. Qiu et al., 2021
	Hyaluronic acid	CD44 targeting ability	R. Nisha et al., 2022
	Biotin-based block copolymer	Active targeting	S. Aleandri et al., 2015
Protein/Peptides	Antimicrobial peptides	Antibacterial	M. Zabara et al., 2021
	Affimer	Cancer cell targeting	Pramanik et al., 2022
	Lactoferrin	Cancer cell targeting	R. Nisha et al., 2020
	Cell-Penetrating Peptides	Skin penetration	R. Petrilli et al., 2016
	Odorranalectin	Improve brain drug delivery	H. Wu et al., 2012
Other	Folate	Tumor targeting	Y. Tian et al., 2017 F. Hou et al., 2020

2. Materials and Methods

2.1. Materials

Monoolein (≥99%,1-Oleoyl-*rac*-glycerol), Pluronic F127 (Poly (ethylene oxide)-poly-(propylene oxide)-poly (ethylene oxide)) were purchased from Sigma-Aldrich. DOTAP (1,2-dipalmitoyl-3-trimethylammonium-propane (chloride salt)), 18:1 NBD-PE (1,2-dioleoyl-*sn*-glycero-3-phosphoethanolamine-*N*-(7-nitro-2-1,3-benzoxadiazol-4-yl) (ammonium salt)) were purchased from Avanti Polar Lipids. Doxorubicin Hydrochloride (DOX), D-PBS, D-MEM (with L-Glutamine and Phenol Red), RPMI-1640 cell culture media (with L-Glutamine and Phenol Red), RPMI-1640 (with L-Glutamine, without Phenol Red), trypsin (0.25 w/v%, EDTA solution with Phenol Red), methanol (99.7%, Methyl Alcohol), MTT (3-(4,5-Dimethylthiazol-2-yl)-2,5-Diphenyltetrazolium Bromide), penicillin-streptomycin solution, protease inhibitor cocktail set V (EDTA free), and LabAssay™ Phospholipid Kit were purchased from Fujifilm. FITC Annexin V Apoptosis Detection Kit I was purchased from BD Pharmingen. Pierce® BCA (Bicinchoninic acid) Protein Assay Kit was purchased from Thermo Fisher Scientific. DiR near-IR membrane probe (1,1'-Dioctadecyl-3,3,3',3'-tetramethylindotricarbocyanine iodide) was purchased from Abcam.

2.2. Cell line and cell culture

J774.1 (a BALB/c mouse derived macrophage cell line), Colon26 (a BALB/c mouse derived colon cancer cell line) and HEK293 cells (a human fetal kidney-derived cell line) were obtained from JCRB Cell Bank. J774.1 and Colon26 cells were cultured using RPMI 1640 cell culture media, HEK293 cells were cultured in D-MEM media. All cell culture media were supplemented with 10% (v/v) fetal bovine serum and 1% (v/v) of penicillin/streptomycin. Cells were maintained at 37°C in a humidified atmosphere with 5% CO_2.

2.3. Cubosomes preparation and macrophage membrane camouflaging

MO-only CBs and cationic CBs were prepared via the method described in Chapter 2. The macrophage cell membrane vesicles were obtained from J774.1 cells through a sucrose gradient ultracentrifugation method. Briefly, J774.1 cells were cultured in 100 mm cell culture dishes. Once the cells reached 90% confluency, they were detached using pipetting and collected in D-PBS without using trypsin. After washing using D-PBS and centrifugation, the cell sediment was resuspended in cold Tris-magnesium buffer (TM buffer, pH 7.4, 0.01 M Tris and 0.001 M $MgCl_2$) containing protease inhibitor and incubated for 15 min at 4℃. The cell-TM buffer suspension was then extruded 20 times through a mini-extruder without polycarbonate membrane to rupture the cells. Sucrose solution was added to the cell homogenate to a final concentration of 0.25 M and the homogenate was centrifuged at 2000 g and 4°C for 15 min. The resulting supernatant was collected and extruded through 200 nm and 100 nm pore-sized polycarbonate membranes in sequence followed by ultra-centrifugation (50000 rpm, 4°C) for 120 min to collect the cell membrane vesicles. The extracted cell membrane vesicles were stored at 4℃ for immediate use and at −80℃ for long-term storage.

Sonification method was utilized for the cell membrane coating on CBs. The extracted cell membranes were resuspended in D-PBS and sonicated to disperse the cell membrane vesicles, The protein content and phospholipid concentration in the extracted macrophage membrane were determined using a BCA assay kit and a LabAssay phospholipid kit, respectively. Then, the cell membrane vesicles were mixed with CBs at different ratios (MO to protein weight ratio). The mixed samples were shaken and then vortexed for 5 min. After the vortex, samples were sonicated on ice in a sonification bath for 15 min.

For the cell internalization efficacy assay, 0.5wt% of 18:1 NBD-PE (dye to MO ratio) was added to the MO or MO/DOTAP solution before vacuuming to prepare fluorescence dye-labeled CBs. For DOX-loaded CBs preparation, DOX was dissolved in methanol and then added to MO/DOTAP solution at a final ratio of 0.5wt% (DOX to MO ratio) before vacuuming. For *in vivo* imaging research, 0.1mol% of DiR was added to the MO/DOTAP solution before vacuuming to prepare DiR-labelled CBs.

In the following sections, cubosomes prepared solely from monoolein are referred as MO-only CBs; the DOTAP-doped cubosomes as cationic CBs; the extracted macrophage membrane vesicles as MMVs; and the macrophage membrane camouflaged CBs as MM@CBs.

2.4. DOX loading efficacy and drug release pattern

The DOX drug encapsulation efficacy investigation was carried out using ultrafiltration units (USY-5, MWCO 50 kD, Advantec, Japan). To determine the amount of free DOX, 1 mL of DOX-loaded CBs was added to the ultrafiltration tube and pressurized with air for 10 min. The eluted solution was collected and analyzed using a fluorescence spectrometer (FP-8500 Spectrofluorometer, JASCO, Japan) at 25 °C, with an excitation wavelength of 485 nm and emission wavelength of 556.5 nm.

The DOX encapsulation efficacy (EE) was calculated according to the following equation:

$$\mathrm{EE}(\%) = \frac{[\text{Total DOX} - \text{Eluted DOX}]}{[\text{Total DOX}]} \times 100\% \qquad Eq.(5-1)$$

The dialysis method was employed to investigate the *in vitro* release of DOX. Specifically, 1 mL of DOX-loaded CBs was added to a dialysis tubing with a molecular weight cut-off of 12-14 kD and dialyzed against 20 mL of D-PBS in a brown vial at room temperature. At predetermined time intervals, 1 mL of the dialysis buffer was withdrawn from the vial and replaced with 1 mL of fresh buffer. The DOX concentrations in the collected samples were determined using a spectrofluorometer as previously described.

2.5. Small-angle X-ray scattering (SAXS) investigation

Described in Chapter 2.

2.6. Cryogenic transmission electron microscopy (cryo-TEM)

Described in Chapter 2.

2.7. Biodistribution investigation

CBs were labeled with 0.1 mol% DiR during the preparation procedure for *in vivo* biodistribution studies. Male BALB/c mice (6 weeks old) were purchased from Japan SLC (Shizuoka, Japan). The animals had unrestricted access to water and mouse chow and were housed under controlled environmental conditions, including a constant temperature, humidity, and a 12-hour light/dark cycle. All animal experiments were approved by the Ethics Review Committee for Animal Experimentation at Osaka University (BIKEN-AP-R01-15-3).

For the in vivo distribution study, two samples (DiR-MM@CB, DiR-CB) were injected into the tail vein: concentration, 2 mg/mL (calculated based on MO amount); injection volume, 100 μL. The control group received 100 μL of PBS via tail vein injection. Whole-body and organ fluorescence images were captured using an IVIS imaging system (excitation: 720 nm; emission: 790 nm) with a 5s exposure time. Whole-body images were taken at selected time points (0.5, 1, 3, 6, 9, and 24 hours). After the final imaging at 9 and 24 hours, the mice were anesthetized with isoflurane inhalation and euthanized. Organs (liver, lungs, spleen, heart, kidneys) were then collected and imaged using IVIS.

2.8. Mouse plasma preparation

Blood samples were collected from BALB/c mice via the inferior vena cava under anesthesia. Whole blood was centrifuged at 1800 g for 15 minutes at 4°C. The supernatant was then ultracentrifuged at 50,000 g for 30 minutes at 4°C. The resulting plasma was collected for further analysis. For DLS and ζ-potential measurements, 50 μL of plasma was diluted in 1 mL of ultrapure water. Hydrodynamic diameter and ζ-potential were measured in triplicate at 25°C. The mean hydrodynamic diameter of the plasma was 35.42 ± 0.63 nm, with a polydispersity index (PDI) of 0.53 ± 0.01. The ζ-potential was –19.50 ± 2.92 mV.

2.9. Cell membrane protein/phospholipid quantification

Extracted cell membranes were further analyzed and quantified by the membrane-associated proteins and membrane-associated phospholipids, respectively using a Pierce® BCA Protein Assay Kit and, LabAssay™ Phospholipid Kit (Fuji Film). Generally, cell membrane vesicles extracted from 1×10^8 J774.1 contain ~1.53 mg cell membrane-related protein and ~0.21 mg phospholipid. The protein to phospholipid ratio was ~7.29.

3. Results and Discussion

3.1. Cubosome preparation and characterization

For brevity, the monoolein-only cubosomes, DOTAP-doped cubosomes, and macrophage membrane-camouflaged cationic cubosomes fabricated in this study are referred to as MO-only CBs, cationic CBs, and MM@CBs, respectively. The preparation procedure for MM@CBs is illustrated in **Fig. 5-1-A**. Hydrodynamic diameter and ζ-potential of the different CB formulations were investigated, and the results are shown in **Fig. 5-1-B**. The average hydrodynamic diameters of the fabricated MO-only CBs and cationic CBs were 205.4 ± 1.8 nm and 200.9 ± 2.2 nm, respectively. It should be noted that the size of CBs is highly dependent on the preparation procedure, especially factors such as F127 concentration, water content, sonication power, and duration. In this study, F127 concentration was set to 2 mg/mL, and sonication was performed at 100 W for 20 minutes. Additionally, heat treatment was applied to enhance the stability of the CBs' structure (J. Barauskas et al., 2005). The coating efficacy of cell membrane vesicles on core nanoparticles (core-NPs) is influenced by the curvature and size differences between the vesicles and core-NPs (L. Liu et al., 2021). Therefore, the size difference between the cell membrane vesicles and core materials is a crucial parameter for the integrity of the cell membrane camouflaging. To reduce the particle size, the extracted cell membrane vesicles were extruded through a 100 nm pore-sized polycarbonate membrane. The average hydrodynamic particle size of MM@CBs (1:1 MO-to-protein weight ratio) was measured as 256.4 ± 16.6 nm, approximately 27.6% larger compared to the non-coated cationic CBs.

Regarding ζ-potential in ultrapure water, MO-only CBs exhibited a negative ζ-potential (−15.7 ± 0.3 mV), while cationic CBs displayed a high positive ζ-potential (45.4 ± 0.5 mV). After cell membrane coating (1:1 MO-to-protein weight ratio), the ζ-potential shifted to −26.7 ± 0.4 mV, which closely resembled that of the extracted macrophage membrane vesicles (−29.5 ± 1.9 mV). DLS and ζ-potential analysis showed that the cell membrane coating resulted in an increase in the particle size and a significant shift in ζ-potential, indicating successful macrophage membrane coating on cationic CBs.

SDS-PAGE was used to assess the presence of macrophage membrane proteins on MM@CBs. **Fig. 5-1-C** shows distinct and consistent protein bands in MM@CBs, comparable to those in macrophages, confirming that MM@CBs inherited membrane proteins from macrophages.

Electron microscopy (EM) and cryo-transmission electron microscopy (cryo-TEM) were performed to further investigate the morphological changes of CBs before and after membrane camouflaging. As shown in **Fig. 5-1-D**, TEM images revealed that cationic CBs exhibited round or square morphologies. After cell membrane camouflaging, clear surface modifications were observed, likely due to the attachment or fusion of the macrophage membrane onto the cationic CBs. The fast Fourier transforms (FFT) derived from the cryo-TEM images confirmed the presence of internal cubic phases. For cationic CBs, FFT analysis revealed characteristic motifs and reflections of the Q_{II}^{P} phase. For MM@CBs (1:1 MO-to-protein weight ratio), a coexistence of Q_{II}^{D} and Q_{II}^{P} phases was observed.

These DLS, SDS-PAGE, TEM, and cryo-TEM results collectively confirm the successful coating of the cationic CBs with macrophage membranes, validating the feasibility of the camouflaging strategy.

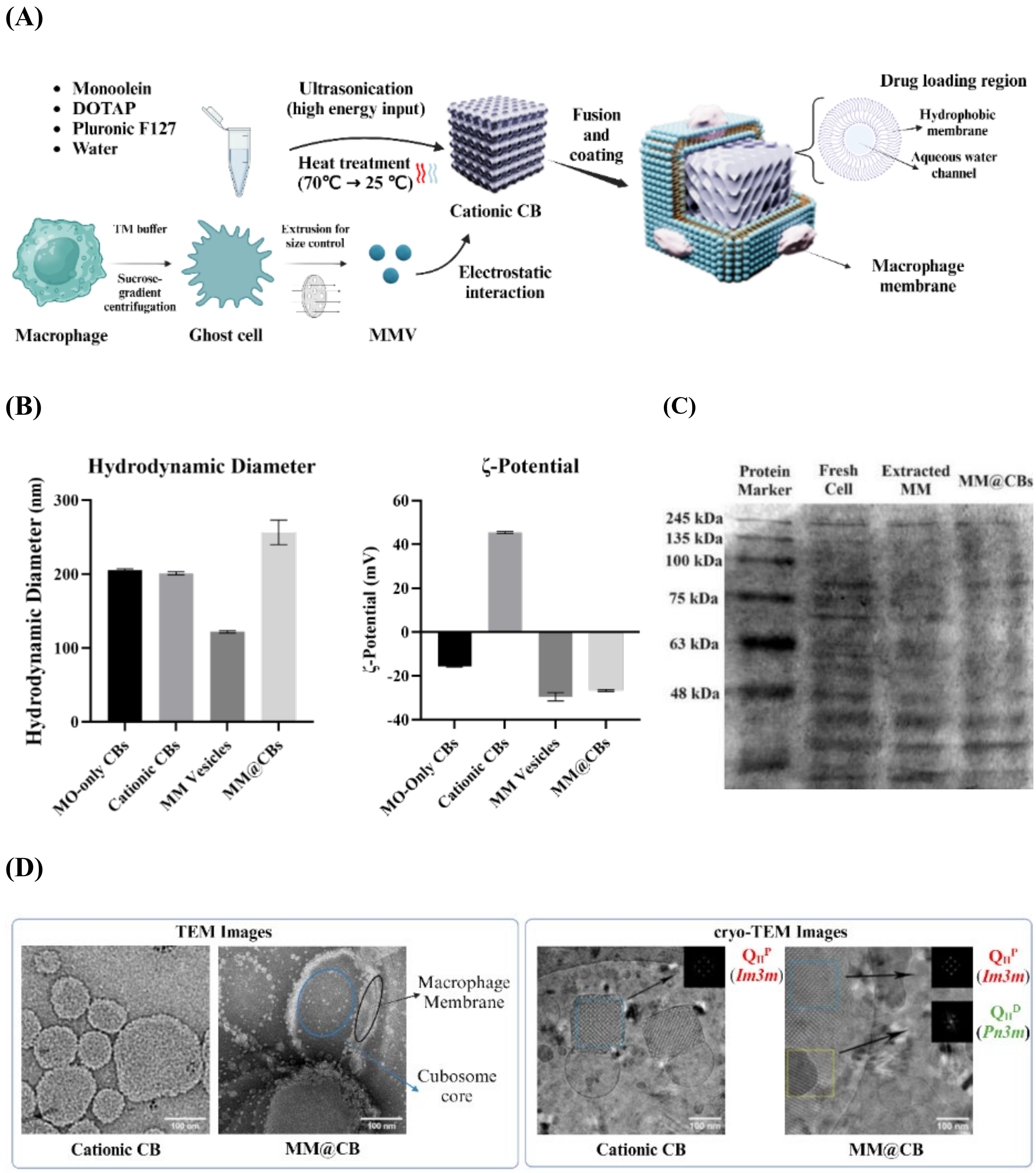

Figure 5-1. Schematic Illustration of MM@CBs Preparation Procedure and Results of Characterizations. (A) Preparation procedure of MM@CBs. **(B)** Hydrodynamic particle size and ζ-potential of fabricated MO-only CBs, cationic CBs, extracted macrophage membrane vesicles (MM vesicles) and MM@CBs (MO to cell membrane protein =1:1 weight ratio) in ultrapure water. All measurements were carried out at 25 °C. Error bars represent ± *s.d.* (*n* = 3). **(C)** SDS-PAGE result of fresh J774.1 cell lysis, extracted J774.1 membrane vesicles and the MM@CBs. **(D)** TEM and cryo-TEM images of cationic CBs and MM@CBs. The upper-right corner of cryo-TEM images show the fast Fourier transform (FFT) of the corresponding squared regions. Scale bar = 100 nm.

Abbreviations: CB, cubosome; MMV, macrophage membrane vesicle; MM@CB, macrophage membrane camouflaged cubosome.

3.2. Cubosome phase changes after cell membrane camouflaging

As illustrated in **Fig. 5-2-A**, MO-based CBs can adopt various cubic phases, including the primitive cubic phase (Q_{II}^{P}), diamond cubic phase (Q_{II}^{D}), and gyroid cubic phase (Q_{II}^{G}). Phase transitions in CBs were observed from cryo-TEM images (**Fig. 5-1-D**) after cell membrane coating. To investigate the effect of membrane camouflaging on the CB structure, small-angle X-ray scattering (SAXS) was conducted to analyze the internal nanostructure of the CBs before and after coating. MM@CBs were fabricated at different MO-to-cell membrane ratios, and the representative SAXS patterns are shown in **Fig. 5-2-B**. The calculated lattice parameters (a) and water channel radius (r_w) of different CB formulations are presented in **Table 5-1**.

At 37°C, SAXS patterns of MO-only CBs exhibited prominent peaks at ~0.681, 0.965, and 1.176 nm^{-1}, while the cationic CBs showed peaks at ~0.615, 0.870, and 1.074 nm^{-1}. Both MO-only and cationic CBs exhibited distinct Bragg peaks at the space ratios of $\sqrt{2}$: $\sqrt{4}$: $\sqrt{6}$, corresponding to Miller indices [h, k, l]: [1, 1, 0], [2, 0, 0], and [2, 1, 1], respectively, indicative of a Q_{II}^{P} phase (space group *Im3m*). The lattice parameters for MO-only and cationic CBs were measured as 13.05 nm and 14.46 nm, respectively. The incorporation of the DOTAP cationic lipid slightly increased the lattice parameter while maintaining the Q_{II}^{P} nanostructure. This is consistent with previous reports indicating that lipid membrane charge repulsion leads to larger water channels in CBs (B. Angelov et al., 2015).

Following macrophage membrane coating, the scattering intensity of the peaks in the CB dispersions slightly decreased, likely due to dilution or changes in ionic strength (A. Yaghmur et al., 2008). To minimize the effects of dilution and ionic strength variations, a consistent dilution factor and ionic strength (same PBS volume) were maintained for all MM@CB formulations. For the MM@CBs with a 1:1 MO-to-cell membrane protein weight ratio, Bragg peaks appeared at ~0.775, 1.088, and 1.329 nm^{-1}, corresponding to a space ratio of $\sqrt{2}$: $\sqrt{4}$: $\sqrt{6}$, indicating the retention of the Q_{II}^{P} phase. Additional peaks at ~1.023, 1.220 and 1.424 nm^{-1}, with a space ratio of $\sqrt{2}$: $\sqrt{3}$: $\sqrt{4}$, indicated the presence of a Q_{II}^{D} phase (*Pn3m*), signifying the coexistence of both Q_{II}^{D} and Q_{II}^{P} phases. Notably, the Q_{II}^{D} phase was observed even at a low membrane protein ratio (10:1 MO-to-protein). As the cell membrane vesicle ratio increased, both the lattice parameters of the Q_{II}^{D} and Q_{II}^{P} phases decreased, suggesting an increase in negative membrane curvature following membrane coating (T. G. Meikle et al., 2017).

The relative intensity of the Bragg peaks corresponding to the Q_{II}^{D} phase increased as the protein-to-MO ratio increased, suggesting that the cell membrane coating promoted the phase transition of cationic CBs. These findings highlight the sensitivity of CBs' structure to membrane protein ratios, offering the intriguing potential to manipulate nanoscale structures through controlled membrane protein content.

A mathematical relationship between the coexisting Q_{II}^{D} and Q_{II}^{P} phases exists, defined by the Bonnet transformation (L. Han et al., 2018). Previous research suggests that both Q_{II}^{D} and Q_{II}^{P} phases consist of minimal surfaces, and under equilibrium conditions, the average Gaussian curvatures of these coexisting cubic phases are expected to be identical. The ratio of lattice parameters between the Q_{II}^{P} and Q_{II}^{D} phases (a_{Im3m}/a_{Pn3m}) should approach the theoretical value of 1.28, known as the Bonnet relation (K. Larsson et al., 2005). To examine the relationship between the coexisting phases in MM@CBs, the lattice parameter ratio (aIm3m/aPn3m) was calculated, and the results are shown in Table 5-2. The lattice parameter ratios of various MM@CB formulations ranged from 1.31 to 1.35 at 37°C, closely aligning with the theoretical value and consistent with the previously reported ratio of 1.33 for MO-based CBs exhibiting both Q_{II}^{D} and Q_{II}^{P} phases (T. Abraham et al., 2008). The Bonnet relation indicates that Q_{II}^{D} and Q_{II}^{P} phases can interconvert through bending while maintaining constant Gaussian curvature.

The transition of CBs from Q_{II}^{P} to Q_{II}^{D} phases ultimately forms a biphasic system, likely due to the fusion of cell membrane proteins and lipids with the CB surface, inducing phase transitions. The various molecules in the cell membrane, such as proteins, peptides, phospholipids, and cholesterol, are thought to influence the phase changes in CBs (C. E. Conn et al., 2013). For example, Thomas G. Meikle et al. observed phase transitions from Q_{II}^{P} to Q_{II}^{D} in MO-based CBs after loading antimicrobial peptides (AMPs), with a decrease in lattice parameters (T. G. Meikle et al., 2017). Sampa Sarkar et al. investigated phase behavior in lipid-water systems and found that the incorporation of cholesterol and phospholipids in MO-based

CBs drives phase transitions in the sequence $Q_{II}^{D} \rightarrow Q_{II}^{P} \rightarrow L\alpha$, the reverse of what was observed in this study (S. Sarkar et al., 2018).

The protein-to-phospholipid ratio of the extracted macrophage membrane vesicles was measured to be approximately 7.29:1 (wt/wt). This suggests that the phase change from Q_{II}^{P} to Q_{II}^{D} in CBs after macrophage membrane coating is primarily driven by the fusion of proteins and peptides from the membrane with the CBs. A high density of membrane proteins on the CB surface induces higher curvature in the interfacial membrane, favoring the Q_{II}^{D} phase (B. Angelov et al., 2014). The high positive charge density of cationic CBs facilitates the recruitment and fusion of negatively charged macrophage membranes, leading to increased interfacial curvature and the formation of Q_{II}^{D} phases. Furthermore, a higher membrane protein-to-MO ratio promotes this phase transition, as evidenced by the increased Bragg peak intensities of the Q_{II}^{D} phase in SAXS patterns (**Fig. 5-2-B**). Given that a low protein ratio may not achieve sufficient camouflaging, the 1:1 MO-to-protein weight ratio was chosen as the optimal ratio for subsequent studies to ensure effective membrane camouflaging on CBs

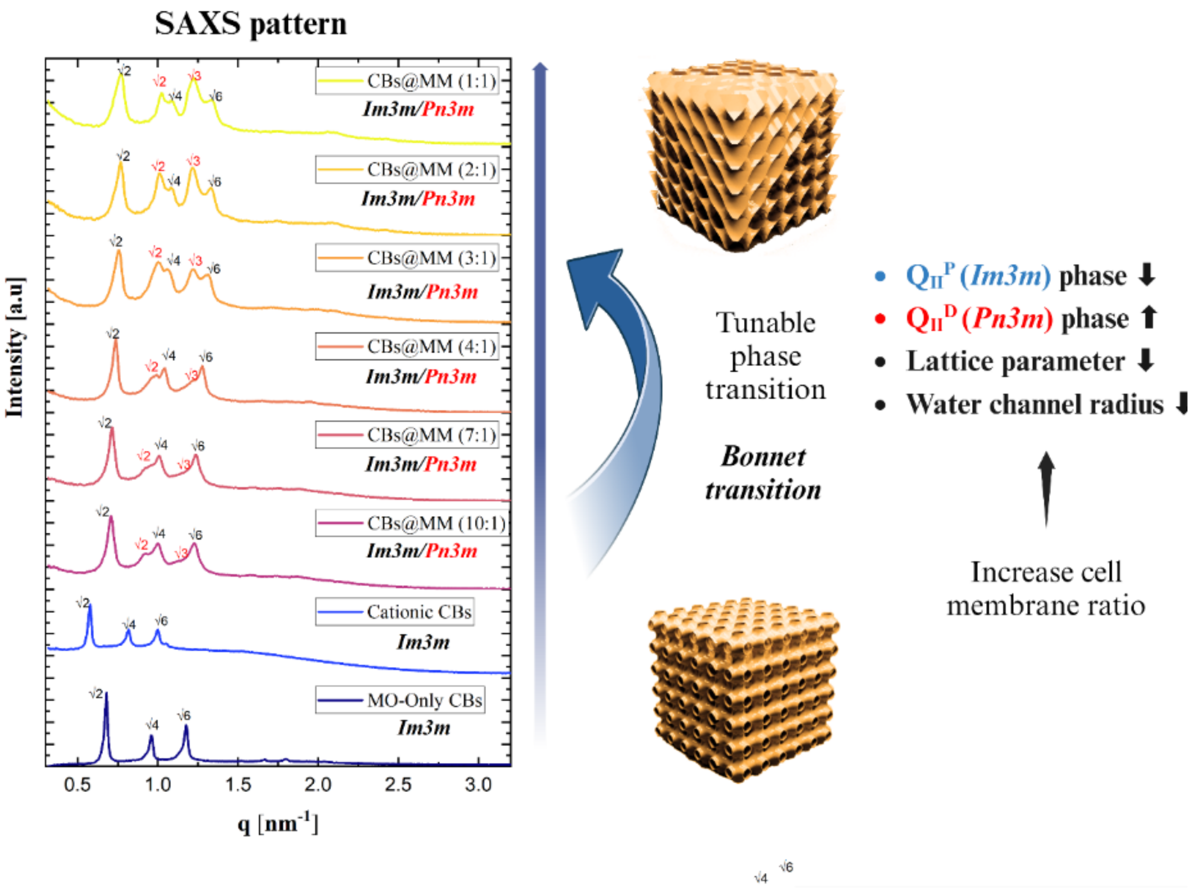

Figure 5-2 SAXS investigation results. (A) The one-dimensional SAXS patterns of different CBs and the cubic phase transition illustration. From bottom to top: MO-only CBs (20 mg/mL MO), cationic CBs (20 mg/mL MO + 1 mol% DOTAP), and MM@CBs with varying compositions (10 mg/mL MO + 1 mol% DOTAP; MO to cell membrane protein weight ratios are 10:1, 7:1, 4:1, 3:1, 2:1 and 1:1). All measurements were conducted at 37°C. Bragg peak spacing ratios identifying *Im3m* and *Pn3m* space group are represented in black and red, respectively.

Table 5-1. Calculated Phase Lattice Parameters of Different CBs.

CB Type	Formulation	Space Group	Lattice Parameter (a) [nm]	Water Channel radius (r_w) [nm]
MO-only CBs	MO	*Im3m*	13.05	2.72
Cationic CBs	MO+ 1 mol% DOTAP	*Im3m*	14.46	2.29
MM@CBs	MO+ 1 mol% DOTAP+ MM (10:1 wt ratio)	*Im3m/Pn3m*	12.53/9.57	2.13/2.04
	MO+ 1 mol% DOTAP+ MM (7:1 wt ratio)	*Im3m/Pn3m*	12.40/9.35	2.09/1.96
	MO+ 1 mol% DOTAP+ MM (4:1 wt ratio)	*Im3m/Pn3m*	12.03/8.94	1.98/1.80
	MO+ 1 mol% DOTAP+ MM (3:1 wt ratio)	*Im3m/Pn3m*	11.68/8.81	1.88/1.75
	MO+ 1 mol% DOTAP+ MM (2:1 wt ratio)	*Im3m/Pn3m*	11.57/8.75	1.84/1.72
	MO+ 1 mol% DOTAP+ MM (1:1 wt ratio)	*Im3m/Pn3m*	11.57/8.69	1.84/1.70

The ratios represent MO: cell membrane protein weight ratio.

Table 5-2. Calculated Bonnet Ratios of Different MM@CBs.

MO to Cell membrane protein weight ratio	Q_{II}^{P} Lattice Parameter (a_{Im3m}) [nm]	Q_{II}^{D} Lattice Parameter (a_{Pn3m}) [nm]	Bonnet Ratio ($a_{Im3m}/\ a_{Pn3m}$)
10:1	12.53	9.57	1.31
7:1	12.40	9.37	1.35
4:1	12.03	8.94	1.35
3:1	11.68	8.81	1.32
2:1	11.57	8.75	1.32
1:1	11.57	8.69	1.33

3.3. Stability of cubosomes *in vitro*

To assess the stability of the prepared CBs, different formulations were incubated in PBS, RPMI cell culture media, and mouse blood plasma. The ζ-potential of the CBs was measured after 0.5 hours of incubation, and the mean hydrodynamic diameter was monitored over a 24-hour period.

The ζ-potential of various CB formulations after 0.5 hours of incubation at 37°C is shown in **Fig. 5-3-A**. Both MO-only CBs and MM@CBs exhibited negative ζ-potentials after incubation in PBS, RPMI media, and mouse plasma. For cationic CBs, a positive ζ-potential was observed after incubation with PBS. However, upon incubation with RPMI media and mouse plasma, the ζ-potential of the cationic CBs shifted dramatically from positive to negative. At physiological pH, the acidic amino acids in the cell culture media, which carry a negative charge, attach to the positively charged surface of the cationic CBs, resulting in a net negative ζ-potential. Similarly, serum proteins such as albumin and globulin in mouse plasma bind to or fuse with the CBs, contributing to the negative ζ-potential (C. C. Fleischer et al., 2012).

The changes in mean hydrodynamic diameter and polydispersity index (PDI) of the different CB formulations after incubation in PBS, RPMI media, and mouse plasma are shown in **Figs. 5-3-B and C**. When incubated with PBS and RPMI media, all CBs maintained stable particle sizes without significant variations. However, after incubation in mouse plasma, the size of MO-only CBs and cationic CBs decreased sharply from ~200 nm to ~100 nm, accompanied by an increase in PDI. These results suggest that non-camouflaged CBs collapsed in plasma. In contrast, the size and PDI of MM@CBs remained stable during the first 4 hours of incubation in mouse plasma, with only a slight decrease in particle size observed after 6 hours. These findings demonstrate the enhanced stability of CBs following cell membrane camouflaging.

Previous studies have shown that MO-based CBs interact rapidly with plasma upon contact, leading to partial destabilization and collapse of the particles. Warunee et al. investigated the disintegration of MO-based CBs in plasma by incubating them with whole plasma and specific plasma components such as HDL (high-density lipoprotein), LDL (low-density lipoprotein), and albumin (W. Leesajakul et al., 2004). Their study found that HDL compromised the integrity of CBs, forming smaller particles containing both CB and HDL components. When incubated with LDL, CBs fused with LDL, while albumin extracted monoolein from the CB particles. J.C. Bode et al. also studied the interaction between MO-based CBs and blood components, using cryo-TEM to show that the surface of CBs decomposed upon plasma incubation, leading to a decrease in particle size. Additionally, the

F127 stabilizer failed to protect CBs from interactions with blood components (J. C. Bode et al., 2013).

Our results, consistent with previous studies, confirm that MO-based CBs disintegrate upon contact with blood plasma. However, macrophage membrane camouflaging significantly enhances the stability of CBs during plasma incubation. The core-shell structure of MM@CBs is believed to shield the CB core from direct interaction with plasma components, preventing disintegration and maintaining particle integrity.

(A)

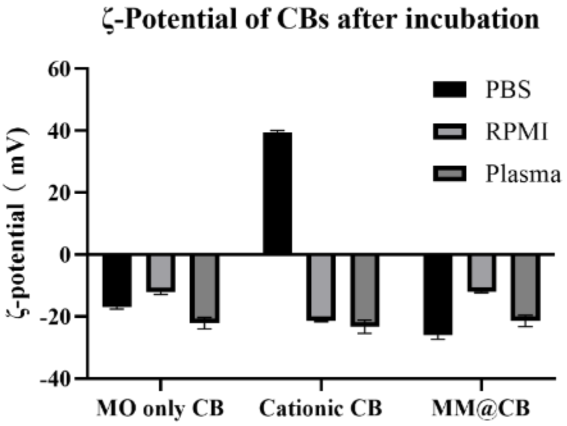

(B)

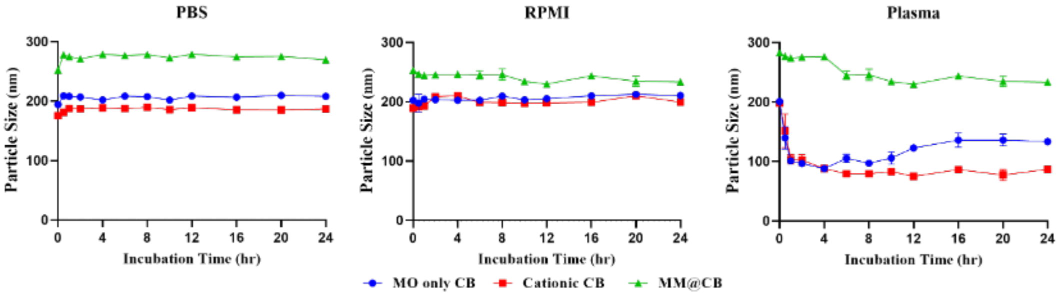

(C)

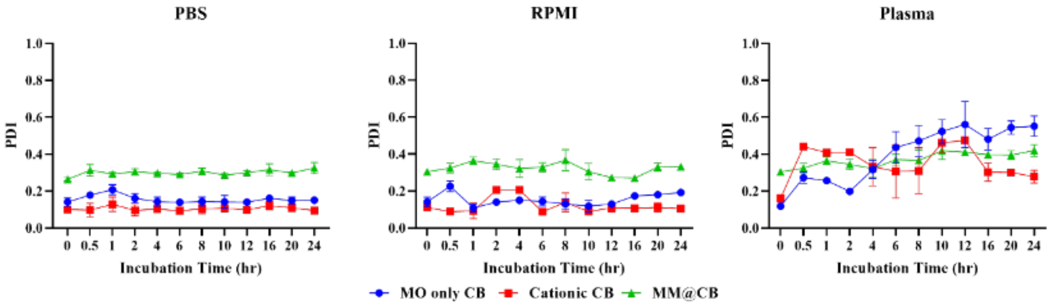

Figure 5-3. Cubosome Stability Characterization. (**A**) ζ-potential of different CBs after 0.5 hr incubation with PBS, RPMI media and mouse plasma respectively. (**B**) Mean hydrodynamic diameters of different CBs during 24 hr incubation with PBS, RPMI media and mouse plasma. **(C)** Polydispersity index (PDI) of different CBs during 24 hr incubation with PBS, RPMI media and mouse plasma. Different CB samples were added into PBS, RPMI media and mouse plasma respectively to a final MO concentration at 5 mg/mL and incubated at 37 °C. For DLS and ζ-potential measurements, 50 μL of samples were diluted in 1mL ultrapure water and measured. All measurements were carried out at 25 °C in triplicate. Error bars represent ± *s.d.* (*n* = 3).

3.4. Macrophage evasion and organ accumulation reduction of MM@CBs

Macrophage cell membrane proteins play a crucial role in preventing the engulfment of foreign nanoparticles by macrophages and other mononuclear phagocytes (Y. Wu et al., 2022). Phagocytosis is the primary mechanism for nanoparticle uptake by macrophages (H. H. Gustafson et al., 2015). While macrophages can easily phagocytize non-coated nanoparticles, those coated with macrophage membranes are better able to evade recognition (A. Parodi et al., 2012). Functional membrane proteins from macrophages can inhibit uptake by macrophages themselves.

To evaluate the *in vitro* macrophage evasion performance of MM@CBs, a cellular internalization study was conducted on J774.1 and Colon26 cells using flow cytometry (FCM) and confocal laser microscopy (CLMS). CBs were doped with 0.5 wt% NBD-PE during preparation to facilitate investigation by FCM and CLMS. SAXS results indicated that the doping of NBD-PE did not induce phase changes in the CBs, except for a slight increase in the lattice parameter compared to non-doped CBs.

Cellular internalization efficacy was evaluated over various incubation times (2, 4, 6, 8, and 12 hours) using FCM. It was noted that individual macrophages show heterogeneity in their phagocytosis capacity (K. Sachdeva et al., 2020). As shown in FCM dot plots (Fig. 5-4-A), after a 4-hour treatment with cationic CBs, J774.1 macrophages were divided into two populations: a low NBD fluorescence group (upper left) and a high NBD fluorescence group (lower right), indicating heterogeneity in internalization. However, after 4 hours of treatment with MM@CBs, the cell population did not show such separation. The NBD fluorescence intensity of MM@CB-treated J774.1 cells was generally lower than that of cationic CBs-treated cells, suggesting a reduced internalization of nanoparticles by macrophages and supporting the macrophage evasion capability of MM@CBs.

The internalization efficacy was monitored for 12 hours using FCM (**Fig. 5-4-B**). During the 2~6 hr period, MM@CBs showed significantly lower internalization than cationic CBs. The mean fluorescence intensity (MFI) increase was reduced by 40.1 ± 13.8% (2 hours), 43.8 ± 12.1% (4 hours), and 36.6 ± 3.8% (6 hours) in the MM@CB group compared to the cationic CB group. After 8 hours, the internalization efficacy of cationic CBs and MM@CBs gradually converged. CLSM images of J774.1 cells after CB treatments (**Fig. 5-4-C**) also showed a lower NBD fluorescence intensity in MM@CB-treated cells after 4 hours, consistent with the FCM results, indicating a reduction in MM@CB internalization by macrophages and demonstrating in vitro immune escape capability.

However, no significant difference in internalization was observed between MM@CBs and cationic CBs when interacting with Colon26 cancer cells. Since both CB formulations exhibited negative ζ-potentials upon contact with cell culture media (**Fig. 5-3-A**), surface charge does not appear to be the primary factor influencing cellular internalization efficacy. The membrane-source macrophages (J774.1) used in this study are non-polarized (M0) and may not display selective internalization capacity towards cancer cells (A. Parodi et al., 2012). Macrophages can be polarized into M1 (pro-inflammatory) or M2 (anti-inflammatory) phenotypes, which influence their internalization properties. A study by C. Hu et al. (2020) showed that both M0 and M1 macrophage membrane-coated nanoparticles exhibited macrophage evasion in vitro, with comparable internalization efficacy in cancer cells. Tumor-associated macrophages (TAMs), present in the solid tumor microenvironment, may exhibit enhanced tumor targeting due to specific surface markers (C. Chen et al., 2021; R. Noy et al., 2014). However, the role of macrophage polarization in cancer targeting remains an area for further investigation.

Overall, MM@CBs demonstrated significant macrophage evasion compared to non-coated CBs, although they did not significantly alter internalization efficacy in Colon26 cancer cells.

Building on the observed stability and macrophage evasion capabilities of MM@CBs in vitro, this study next investigated their biodistribution in mice. In vivo biodistribution images of BALB/c mice following intravenous (*i.v.*) injection of different CB formulations at 9 and 24 hours are shown in **Fig. 5-4-D**. Cationic CBs exhibited widespread distribution throughout the body, whereas MM@CBs showed more localized distribution. As noted earlier, MO-based CBs rapidly interact with plasma upon contact, leading to partial destabilization and collapse (**Fig. 5-3-B**), resulting in widespread DiR distribution. In contrast, MM@CBs appeared more stable, leading to moderate interactions with plasma components and reduced CB collapse.

The accumulation of CBs in major organs (liver, spleen, kidneys, heart, and lungs) was assessed at 9 and 24 hr post-injection. Cationic CBs and MM@CBs exhibited comparable accumulation in the liver and spleen, likely due to the filtration by these organs (E. Blanco et al., 2015). However, MM@CBs showed lower accumulation in the lungs, kidneys, and heart, with a significant reduction in lung accumulation (9 and 24 hr post-injection, $p<0.0001$). Previous studies have shown higher accumulation of MO-based CBs in the heart, kidneys, and lungs (M. Dawoud et al., 2023). The collapse of cationic CBs upon contact with plasma (**Fig. 5-3-B**) results in widespread DiR signals in these organs. Additionally, the serum protein corona that forms on cationic CBs upon plasma contact, as evidenced by the ζ-potential shift (**Fig. 5-3-A**), could trigger recognition by macrophages (K. Saha et al., 2016) and influence their in vivo fate (M. Qiu et al., 2021). Distinct serum proteins formed on the nanoparticle surface may promote accumulation in the lungs (M. Qiu et al., 2022). In contrast, membrane coating reduces serum protein corona formation and limits accumulation in certain organs (D. Zou et al., 2022). Overall, reduced accumulation in the heart, kidneys, and lungs likely extends CB circulation time in vivo, potentially reducing off-target effects and enhancing therapeutic efficacy.

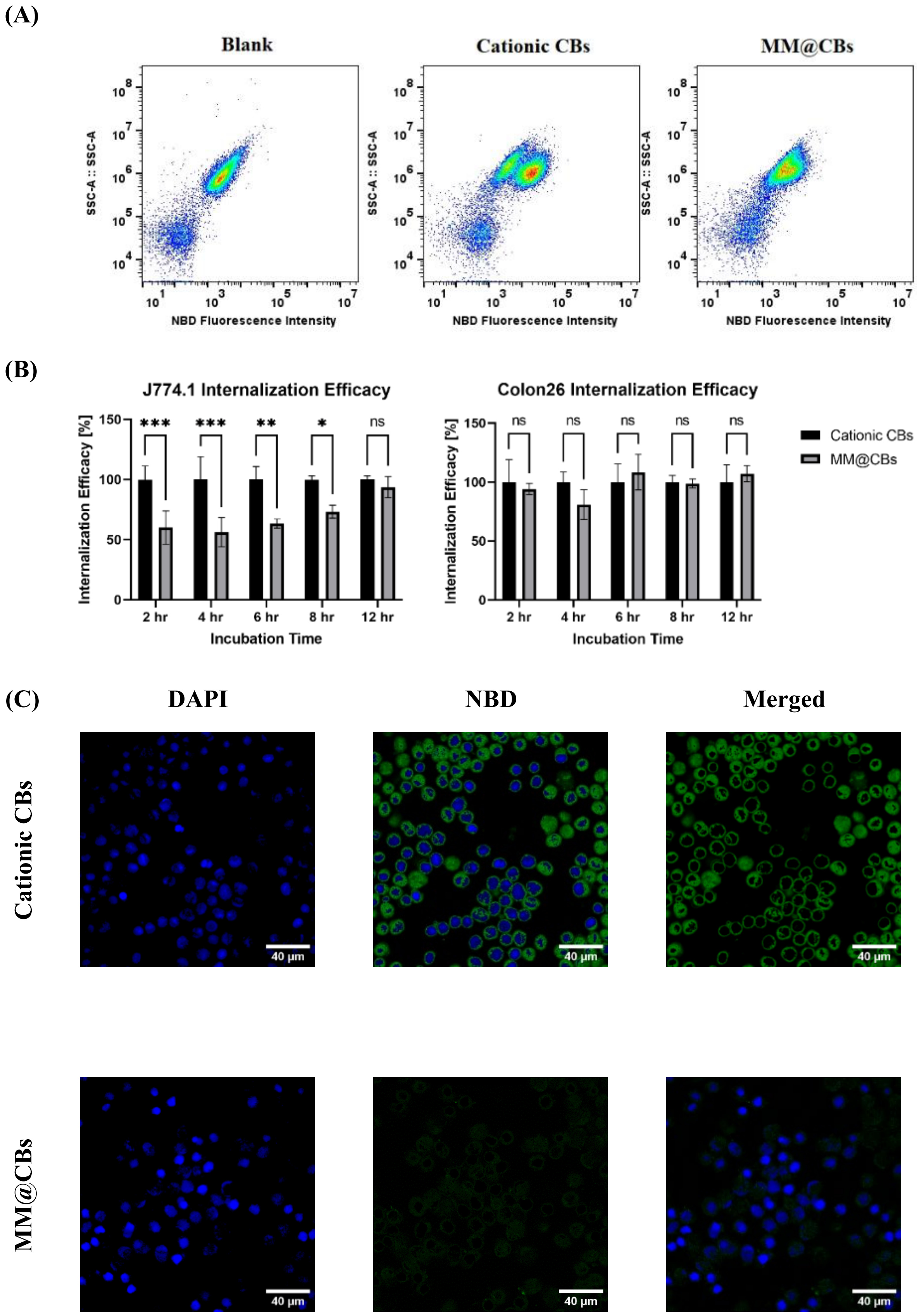
(A)
Blank
Cationic CBs
MM@CBs
SSC-A :: SSC-A
NBD Fluorescence Intensity
(B)
J774.1 Internalization Efficacy
Colon26 Internalization Efficacy
Internalization Efficacy [%]
Incubation Time
2 hr
4 hr
6 hr
8 hr
12 hr
***
***
**
*
ns
Cationic CBs
MM@CBs
(C)
DAPI
NBD
Merged
Cationic CBs
MM@CBs
40 μm

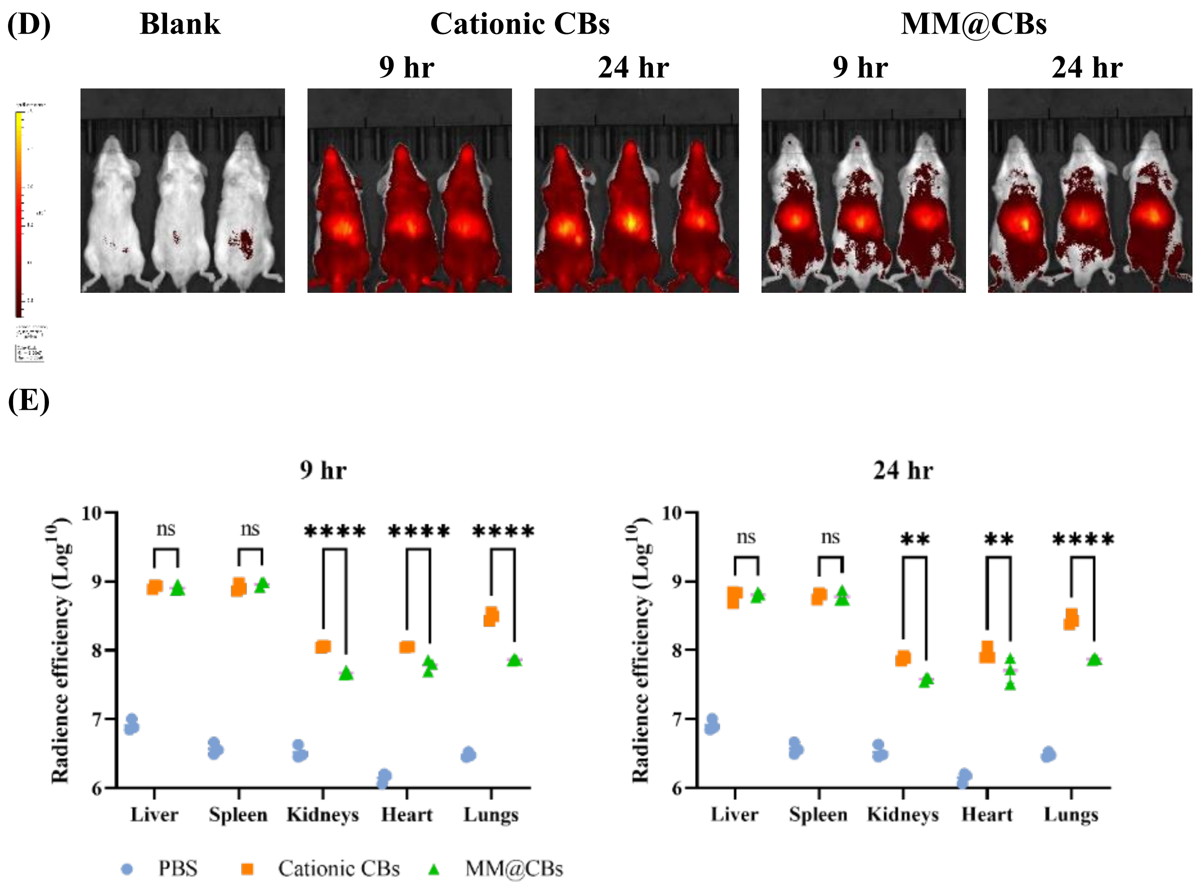

Figure 5-4. ***In vitro*** **Immune-Escape Performance and** ***in vivo*** **Distribution Investigation Results**. **(A)** Dot plot of J774.1 internalization efficacy after 4 hr treatment with 0.15 mg/mL of NBD-PE doped cationic CBs and MM@CBs (calculated according to MO concentration). **(B)** J774.1 and Colon26 cell internalization efficacies on cationic CBs and MM@CBs after different incubation time periods. Cells were incubated with 0.15 mg/mL CBs (calculated according to MO concentration) doped with NBD-PE. The black bars represent the cationic CBs group and the gray bars represent the MM@CBs group. Error bars represent ± *s.d.* *n*=3. **(C)** Confocal laser scanning microscopy (CLSM) images of J774.1 cells after 4 hr treatment with NBD-PE doped cationic CBs and MM@CBs (0.15 mg/mL CBs, calculated according to MO). The three columns are corresponding to DAPI channel, NBD channel and merged pictures respectively. Scale bar = 40 μm. **(D)** Whole body fluorescence imaging of mice after *i.v* injection of DiR-labeled cubosome samples for 9 and 24 h. Color scale ranges from $3^{\times}10^{7}$ to $3\ ^{\times}10^{8}$ ($\frac{p/sec/cm^2/sr}{\mu W/cm^2}$). (E) DiR radiance efficiency in the main organs after *i.v* injection. Error bars = ± *s.d*, *n*=3. *ns*: not significant; *p<0.05; **p<0.01; ***p<0.001; ****p<0.0001.

3.5. DOX loading and anticancer performance *in vitro*

DOX was selected as the model drug to evaluate the drug loading capacity and anti-cancer efficacy of cationic CBs and MM@CBs in this study. During preparation, 0.5 wt% DOX was loaded into the cationic CBs. Characterization results for DOX-loaded cationic CBs and MM@CBs are presented in **Table 5-3**. The drug encapsulation efficiency (EE) results showed a high DOX EE of approximately 91.93%, which can be attributed to the presence of a hydrophilic inner water channel and the large surface area between the bilayer and internal water channels of the CBs, facilitating DOX embedding. After macrophage membrane camouflaging, the EE slightly decreased to approximately 86.29%.

The biocompatibility of the prepared CBs was evaluated using MTT assays on HEK293 cells. The MTT results **(Fig. 5-5**) indicated that 0.2 mg/mL of MO did not significantly inhibit normal cell proliferation after 24 hours of incubation.

Table 5-3. DOX loaded CBs characterization results

CB Formulation	Size [nm]	PDI	Zeta Potential [nm]	Space Group	Lattice Parameter [nm]	Encapsulation Efficacy (%)
Cationic CBs + DOX	228.2 ± 3.5	0.14 ± 0.03	29.9 ± 1.5	*Im3m*	14.46	91.93 ± 0.16
MM@CBs + DOX	270.7 ± 5.9	0.28 ± 0.01	-27.5 ± 1.9	*Im3m/Pn3m*	14.28/10.95	86.29 ± 0.08

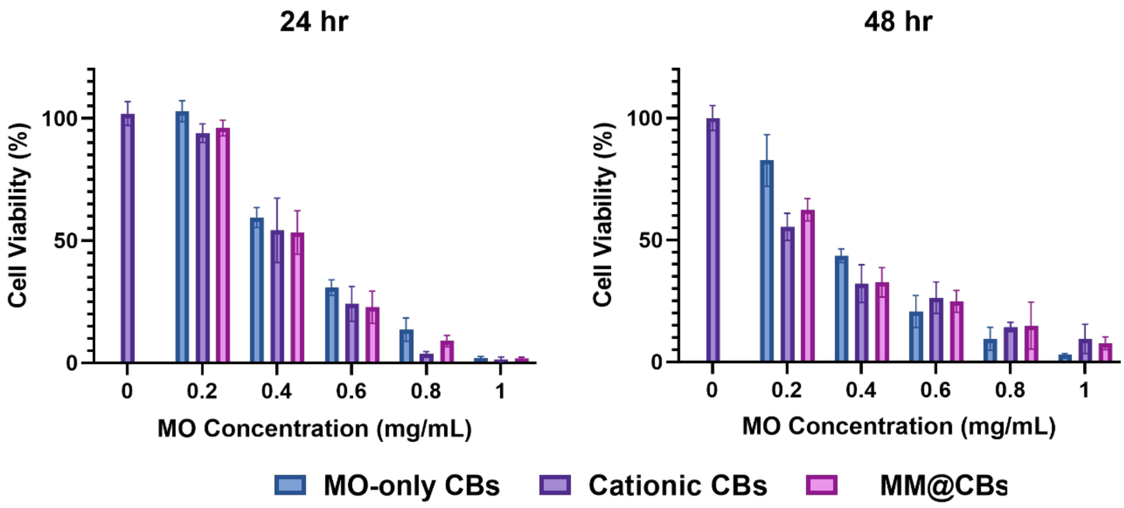

Figure 5-5. MTT Assay Results. HEK293 cells were treated for 24/48 hours with MO-only CBs, cationic CBs, and MM@CBs at different concentrations (calculated according to the MO concentration). Error bars represent ± *s.d.* *n*=3.

The *in vitro* DOX release patterns are shown in **Fig. 5-6-A**. Both cationic CBs and MM@CBs demonstrated comparable drug release profiles. However, the release rate from MM@CBs was slightly higher than that from cationic CBs. The reduction in DOX EE and the differences in drug release rates can be attributed to structural and phase changes in CBs during the macrophage membrane coating. Specifically, the cubic lipid phase transition (from *Im3m* to *Pn3m*) and the reduction in the water channel radius during cell membrane coating leads to partial DOX leakage, resulting in a slightly higher release rate from MM@CBs. These findings highlight the importance of considering the impact of cell membrane coating and phase transitions on drug release behavior, which is crucial for developing controlled drug release systems. Further research is needed to better understand these mechanisms and optimize the drug release properties of MM@CBs for specific therapeutic applications.

The anti-cancer performance was assessed using Colon26 cell lines. Free DOX and different DOX-loaded CB formulations were introduced to Colon26 cells at a final DOX concentration of 1 μg/mL (MO concentration 0.2 mg/mL) and incubated for 12 and 24 hours. For comparison, cationic CBs (without DOX) and MM@CBs (without DOX) were introduced to Colon26 cells at a final concentration of 0.2 mg/mL (based on MO concentration). As shown in **Fig. 5-6-B, C**, both cationic CBs and MM@CBs induced mild and comparable apoptosis in

Colon26 cells. After 12 hours, both the cationic CBs+DOX and MM@CBs+DOX groups showed slightly enhanced anti-cancer effects compared to the free DOX group, with no significant difference between the two. However, after 24 hours, both cationic CBs+DOX and MM@CBs+DOX exhibited significantly improved performance compared to the free DOX group. Notably, the late apoptotic cell ratio was higher in the MM@CBs+DOX group than in the free DOX and cationic CBs+DOX groups. This is likely due to the faster release of DOX from MM@CBs after cellular uptake, leading to higher intracellular DOX concentrations and triggering earlier apoptosis. Thus, while cationic CBs and MM@CBs showed similar internalization efficiency by Colon26 cells, the faster DOX release from MM@CBs may result in a more rapid onset of apoptosis, accelerating the late apoptotic phase in Colon26 cells.

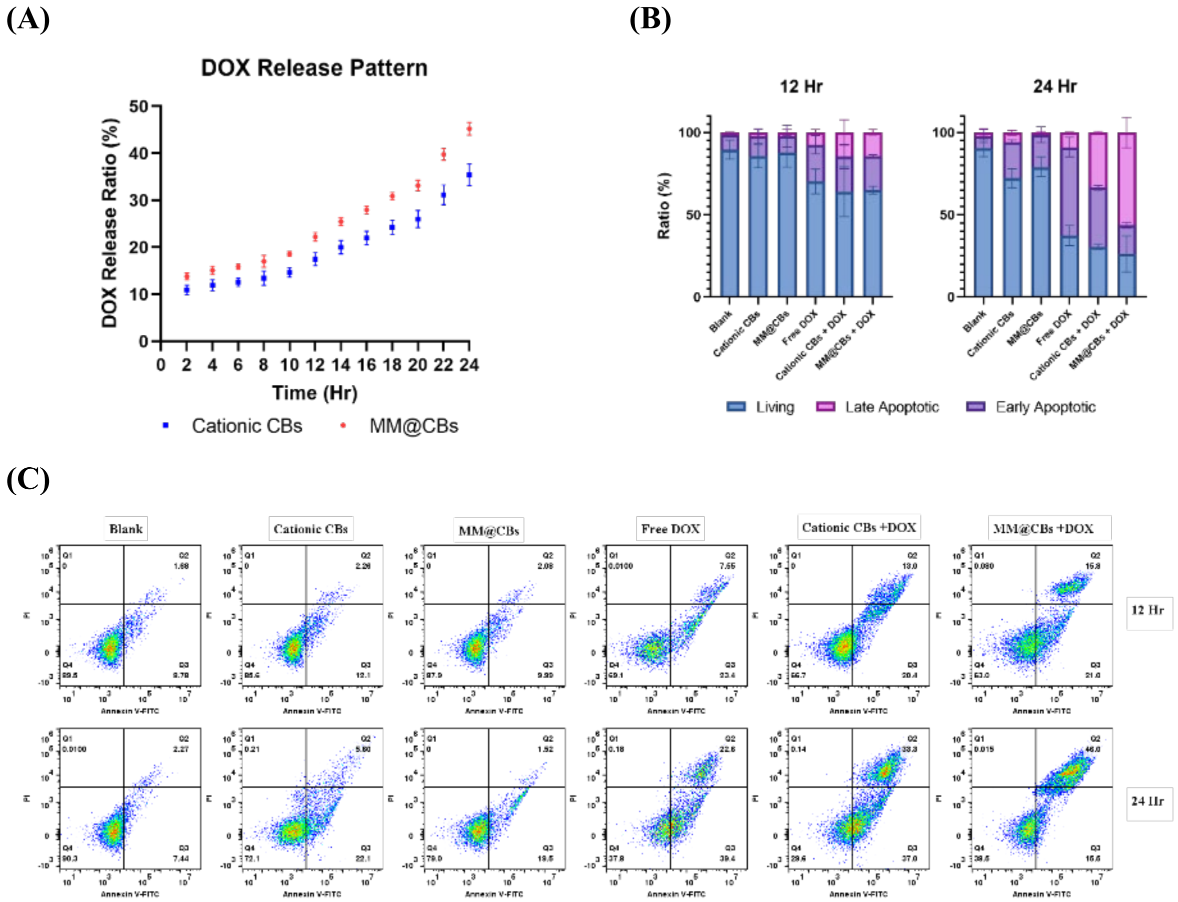

Figure 5-6. DOX release pattern and Colon26 Annexin-V/PI assay results. (**A**) Release pattern of DOX-loaded cationic CBs (blue) and MM@CBs (red) *in vitro*. (**B**) The stack bar graphs showing the percentage of living cells, early apoptotic cells and late apoptotic Colon26 cells (**C**) the dot graph of the Colon26 cells Annexin-V/PI assay results after cationic CBs, MM@CBs, free DOX, DOX-loaded cationic CBs and DOX-loaded MM@CBs treatments for 12/24 hr. The operation is detailed in Experimental section 2-10. Error bars represent ± *s.d.* (*n* = 3)

4. Summary

The objective of this study was to explore a strategy for stabilizing cubosomes (CBs) and enhancing their immune escape capabilities by using macrophage cell membranes for surface modification, as an alternative to the conventional PEGylation approach. Our systematic characterization results revealed that the CB structure slightly shifted from a Q_{II}^{P} phase to a coexistence of Q_{II}^{P} and Q_{II}^{D} phases following macrophage membrane camouflaging. The MM@CBs exhibited delayed internalization by macrophages (J774.1 cells), while cancer cell uptake remained unaffected. Additionally, macrophage membrane camouflaging stabilized the CBs in vivo, reducing their accumulation in the heart, kidneys, and lungs.

These findings suggest that cell membrane camouflaging is a promising strategy for modifying the surface properties of CBs, effectively combining the physical characteristics of CBs with the biofunctional advantages of cell membranes. Overall, our results indicate that this approach holds great potential for enhancing the performance of CB-based nanomedicines, leveraging the immune escape properties of macrophage membrane coatings and facilitating the delivery of a wide range of therapeutic drugs. Furthermore, further engineering of membrane source cells could improve the cancer-targeting capabilities of these formulations.

In conclusion, the study demonstrates the feasibility of using macrophage cell membrane camouflaging as a surface modification strategy for CBs. The successful integration of both physical and biofunctional properties shows promise for future applications in drug delivery research and development.

Chapter 6

General Conclusion

The research provides comprehensive insights into the self-assembly of amphiphilic molecules into diverse lyotropic phases, and characterizes their structural behaviors under varying environmental conditions. Phase transitions from lamellar to cubic structures are driven by lipid membrane curvature changes, which are influenced by the critical packing parameter (*CPP*) and the protonation states of lipid molecules. Techniques like small-angle X-ray scattering (SAXS), dynamic light scattering (DLS), and cryo-TEM show that the composition of lipid nanoparticles (LNPs) can be strategically manipulated to fine-tune their physicochemical properties. These findings have significant implications for advanced drug delivery systems, where stability and targeted release are critical, particularly in applications such as cancer treatment and gene therapy.

Chapter 1 introduces the fundamental concepts of lipid-based self-assembling nanoparticles and key properties related to the biophysical properties of cytoplasmic membranes. It also reviews studies on LNP internalization pathway by cells, providing insights into the interactions between LNPs and cell membranes. Lipid self-assembling refer to the process by which lipids spontaneously organize into ordered structures in aqueous environments due to their amphiphilic nature. A key concept in understanding lipid self-assembly's phase behavior is the critical packing parameter (*CPP*), which predicts how the molecular geometry of lipids influences their self-assembled morphology. Lipid molecular shape is an important consideration in lipid membrane modeling. Based on the physical dimensions of a lipid component, its phase presence upon hydration and its location in the membrane can often be predicted. Another crucial factor in engineering lipid self-assembly systems is the ionization state of the lipids, commonly described by their apparent acid dissociation constant (pKa). Changes in ionic strength and pH can significantly influence the CPP value of lipids and induce changes in electrostatic interactions between lipid molecules, changing their packing status. For another thing, lipid-membrane fluidity and lipid-water interfacial polarity are pivotal factors could indicate the LNP lyotropic phase status to some extent. Also, the LNP membrane polarity and fluidity influence the functions of LNPs. Specifically, lipid-membrane fluidity is a fundamental physicochemical property of LNPs formulations, reflecting the dynamics, micro-viscosity, and organization of lipids within the membrane bilayer. This fluidity is crucial for determining the stability and functionality of liposomes, impacting both their in vitro and in vivo properties, which ultimately influences the therapeutic efficiency of encapsulated cargo molecules. This study investigated LNPs with various internal lyotropic phases and their direct or indirect interactions with cell membranes. This study further examined the lyotropic phase behavior of LNPs, the properties of the cellular plasma membrane, and the mechanisms of LNP-cell membrane interactions. This approach aims to provide deeper insights into how LNP phase behavior influences their *in vitro* and *in vivo* fate.

Chapter 2 focuses on the preparation and characterization of LNPs in different lyotropic phases. Several factors would impact the lyotropic phases of the lipid self-assemblies. Those factors including lipid composition (type of lipids, saturation degree and lipid ratios etc.), preparation method (thin film hydration, ethanol injection, microfluidics etc.), hydration level, temperature, pH and ionic strength etc. Typically, LNPs prepared using phospholipid via the thing-film hydration method exhibit a lamellar ($L\alpha$) vesicle structure. In contrast, the formation of cubic-phase LNPs generally relies on lipids such as monoolein (MO) or phytantriol (PYT). The top-down method, one of the most widely used techniques for preparing cubic-phase LNPs, involves the mechanical fragmentation of a bulk cubic liquid crystalline phase (formed by MO or PYT in water) into nanoparticles. This fragmentation is achieved using techniques like ultrasonication or high-pressure homogenization. To accurately analyze the phase behavior and morphologies of these LNPs, a variety of advanced characterization techniques were employed. Small-Angle X-Ray Scattering (SAXS), Transmission Electron Microscopy (TEM), and Cryo-TEM provided detailed insights into the internal structures and morphologies of LNPs across different phases. Typically, SAXS is a powerful analytical technique for characterizing LNPs at the nanometer scale. It provides detailed insights into the internal structures of LNPs, including their size, shape, and organization. In this chapter, LNPs were prepared using a variety of lipid compositions, including DOPC, 2-hydroxyoleic acid (2-OHOA), MO, and

DOTAP. By manipulating lipid formulations or adjusting environmental conditions, a wide range of lyotropic phases was achieved. Representative SAXS patterns revealed distinct structural organizations, including lamellar vesicles (Lα) and cubic-phase nanoparticles (Im3m and Pn3m). Cryo-TEM provided further morphological details, while DLS offered insights into their physicochemical properties. this chapter provides a detailed exploration of the lyotropic phase behavior of LNPs, emphasizing the versatility of lipid-based systems. The combination of characterization techniques like SAXS, DLS, and Cryo-TEM enabled a thorough understanding of the phase transitions and structural characteristics of LNPs, with comparisons drawn between key parameters across different phases.

Chapter 3 investigates the properties of lipid membranes across different LNP phases, focusing on their structural and physicochemical transformations. These properties were characterized using fluorescence probes (Laurdan and DPH) and Raman spectroscopy, which provided insights into lipid packing, membrane-water interfacial polarity, and phase transitions. A binary system composed of 2-OHOA and MO was used as a model for studying pH-triggered phase transitions from lamellar (Lα) to cubic (Im3m/Pn3m), allowing a detailed examination of how lipid membrane properties change during these transitions. SAXS characterization confirmed the phase behavior of the 2-OHOA/MO LNPs, revealing lamellar phase structures (Lα) at neutral and mildly acidic pH (7.4 and 4.5). At pH 3.0, the system transitioned to cubic phase structures (Im3m and Pn3m). DLS analysis showed an unstable state for the 2-OHOA/MO nano-dispersions at pH 4.5, indicating a transitional phase status. On the other hand, at neutral pH (7.4), MO-only dispersions exhibited a cubic Im3m phase, while 2-OHOA-only dispersions showed multilamellar (*Lα*) phase. The physicochemical properties of lipid-membranes of these LNPs were further explored using Laurdand and DPH fluorescence probes. Fluorescent probe studies highlighted that the lipid-water interfacial polarity and membrane fluidity changed in tandem with the phase transition in 2-OHOA/MO dispersions. Specifically, as the system transitioned to the cubic phase at lower pH, both polarity and membrane dynamics shifted significantly. Raman spectroscopy provided additional insights into lipid chain dynamics. The chain torsion (S) and chain packing (R) parameters were found to peak at pH 3.0 in the 5 mol% 2-OHOA/MO system, correlating with the formation of the Im3m cubic phase. These results indicate a strong relationship between lipid molecular packing, lipid membrane polarity/fluidity, and phase organization of LNPs. This chapter highlights the ability to track both phase behavior and lipid membrane properties during pH-induced phase transitions. The synchronous changes in membrane properties with phase shifts provide insights into how structural transformations affect overall nanoparticle behavior. The findings have potential implications for the design of pH-responsive drug delivery systems. By understanding the interplay between lipid composition, phase transitions, and membrane characteristics, it becomes possible to optimize drug loading and release profiles, tailoring them to specific therapeutic needs. In particular, it holds promise for targeting environments where pH fluctuations are critical, such as the tumor microenvironment, offering potential for more precise and controlled drug delivery systems.

Chapter 4 explores the biophysical properties of cell plasma membranes using imaging techniques, including Laurdan two-photon microscopy (TPM) and LipiORDER fluorescence microscopy. Laurdan-TPM provided insights into cell membrane fluidity and polarity, revealing distinct lipid membrane polarities across different cell types. This technique also allowed for the visualization of heterogeneity in cell membrane polarity with a high-resolution. LipiORDER microscopy further complemented these findings by assessing lipid packing within cell membranes. Building on these methods, the chapter investigates how LNPs modulate the biophysical properties of cell membranes during internalization. Specifically, the focus was on 2-OHOA, a known sphingomyelin synthase (SMS) activator that increases sphingomyelin (SM) abundance in cell membranes. To explore this, 2-OHOA/DOPC LNPs were used as the model system to study their effects on the plasma membranes of NP-8 and HepG-2 cells. Laurdan-TPM demonstrated that both free 2-OHOA and 2-OHOA-embedded liposomes significantly reduced membrane fluidity in these cell lines. Interestingly, the liposome formulation enhanced the impact of 2-OHOA on cell membrane polarity/fluidity, with distinct patterns observed in the two cell types. LipiORDER microscopy corroborated these results, showing substantial changes in lipid packing after treatment with 2-OHOA-embedded liposomes. The investigation was further extended to examine the cellular internalization mechanisms, revealing that the enhanced performance of 2-OHOA-embedded liposomes was largely dependent on endocytosis. This suggests that the liposome formulation not only improved cellular uptake of 2-OHOA but also enhanced its therapeutic potential. The encapsulated form of 2-OHOA demonstrated superior anticancer efficacy compared to the free drug, highlighting the benefits of using liposomal delivery to enhance solubility and biological activity. These findings illustrated that LNP formulations can overcome the solubility limitations of 2-OHOA while amplifying its therapeutic effects. The ability of these LNPs to modulate cell membrane properties, particularly through endocytosis, highlights the importance of investigating LNP-cell interactions to optimize LNP formulations for enhanced drug delivery applications.

Chapter 5 introduces a strategy for stabilizing cubic-phase lyotropic liquid crystalline nanoparticles (Cubosomes) by coating them with macrophage cell membranes, instead of the conventional PEGylation method. The goal of this approach is to improve the immune escape capabilities of cubosomes (CBs) while maintaining their structural integrity and functionality. Systematic characterization revealed that the structure of the cubosomes slightly shifted from a Q_{II}^{P} (*Im3m*) phase to a coexistence of Q_{II}^{P} (*Im3m*) and Q_{II}^{D} (*Pn3m*) phases after the macrophage membrane coating. Importantly, the macrophage membrane-coated cubosomes (MM@CBs) exhibited delayed internalization by macrophage cells (J774.1), indicating improved immune evasion. At the same time, the coating did not significantly impact the uptake of the cubosomes by cancer cells, maintaining their efficacy in targeting tumors. The macrophage membrane camouflage not only enhanced the stability of the cubosomes in vivo but also reduced their unwanted accumulation in major organs like the heart, kidneys, and lungs. This suggests that the cell membrane coating effectively combines the structural advantages of cubosomes with the bio-functional properties of macrophage membranes, enhancing their potential for therapeutic applications. These findings highlight the potential of macrophage cell membrane camouflaging as an innovative surface modification strategy for cubosomes. By leveraging the immune escape properties of macrophage membranes and the ability of cubosomes to carry a wide range of therapeutic molecules, this approach shows promise in improving the performance of CB-based nanomedicine delivery systems. Furthermore, future engineering of the source cells for the membrane coating could enhance cancer-targeting capabilities, opening new avenues for more precise and effective drug delivery platforms.

Chapter 6 presents the general conclusions of this work, which deepen our understanding of how lipid nanoparticles interact with cell plasma membranes. Based on these findings, this study proposes a cell membrane camouflage strategy to stabilize cubic-phase LNPs and confer immune evasion capabilities. These insights hold potential for advancing LNP design and optimization for more effective drug delivery performance.

Reference

Abdel-Bar, H. M.; el Basset Sanad, R. A. Endocytic Pathways of Optimized Resveratrol Cubosomes Capturing into Human Hepatoma Cells. *Biomedicine & Pharmacotherapy* 2017, *93*, 561–569.

Aguilar, L. F.; Pino, J. A.; Soto-Arriaza, M. A.; Cuevas, F. J.; Sánchez, S.; Sotomayor, C. P. Differential Dynamic and Structural Behavior of Lipid-Cholesterol Domains in Model Membranes. *PLoS ONE* 2012, 7.

Akbarzadeh, A.; Rezaei-Sadabady, R.; Davaran, S.; Joo, S. W.; Zarghami, N.; Hanifehpour, Y.; Samiei, M.; Kouhi, M.; Nejati-Koshki, K. Liposome: Classification, Preparation, and Applications. *Nanoscale Research Letters* 2013, 8.

Akhlaghi, S. P.; Ribeiro, I. R.; Boyd, B. J.; Loh, W. Impact of Preparation Method and Variables on the Internal Structure, Morphology, and Presence of Liposomes in Phytantriol-Pluronic® F127 Cubosomes. *Colloids and Surfaces B: Biointerfaces* 2016, 145, 845–853.

Alemany, R.; Terés, S.; Baamonde, C.; Benet, M.; Vögler, O.; Escribá, P. V. 2-Hydroxyoleic Acid. *Hypertension* 2004, 43 (2), 249–254.

Ambrosini, A.; Bertoli, E.; Tanfani, F.; Wozniak, M.; Zolese, G. The Effect of N-acyl Ethanolamines on Phosphatidylethanolamine Phase Transitions Studied by Laurdan Generalised Polarization. *Chem. Phys. Lipids* 1994, 72, 127−134.

Angelov, B.; Angelova, A.; Drechsler, M.; Garamus, V. M.; Mutafchieva, R.; Lesieur, S. Identification of Large Channels in Cationic Pegylated Cubosome Nanoparticles by Synchrotron Radiation SAXS and Cryo-TEM Imaging. *Soft Matter* 2015, *11*, 3686–3692.

Angelov, B.; Ollivon, M.; Angelova, A. X-Ray Diffraction Study of the Effect of the Detergent Octyl Glucoside on the Structure of Lamellar and Nonlamellar Lipid/Water Phases of Use for Membrane Protein Reconstitution. *Langmuir* 1999, *15*, 8225–8234.

Antoniou, A. I. et al. 2-hydroxyoleic acid as a self-assembly inducer for anti-cancer drug-centered nanoparticles. *Pharmaceuticals* 16, 722 (2023).

Aota-Nakano, Y.; Li, S. J.; Yamazaki, M. Effects of Electrostatic Interaction on the Phase Stability and Structures of Cubic Phases of Monoolein/Oleic Acid Mixture Membranes. *Biochimica et Biophysica Acta (BBA) - Biomembranes* 1999, 1461 (1), 96–102.

Augustine, R.; Hasan, A.; Primavera, R.; Wilson, R. J.; Thakor, A. S.; Kevadiya, B. D. Cellular Uptake and Retention of Nanoparticles: Insights on Particle Properties and Interaction with Cellular Components. *Materials Today Communications* 2020, *25*, 101692.

Bailey, R. W.; Nguyen, T.; Robertson, L.; Gibbons, E.; Nelson, J.; Christensen, R. E.; Bell, J. P.; Judd, A. M.; Bell, J. D. Sequence of Physical Changes to the Cell Membrane during Glucocorticoid-Induced Apoptosis in S49 Lymphoma Cells. *Biophysical Journal* 2009, *96*, 2709–2718.

Barceló, F.; Prades, J.; Funari, S. S.; Frau, J.; Alemany, R.; Escribá, P. V. The Hypotensive Drug 2-Hydroxyoleic Acid Modifies the Structural Properties of Model Membranes. *Molecular*

Membrane Biology 2004, 21 (4), 261–268.

Barceló-Coblijn, G. et al. Sphingomyelin and sphingomyelin synthase (SMS) in the malignant transformation of glioma cells and in 2-hydroxyoleic acid therapy. *Proceedings of the National Academy of Sciences* 2011 108, 19569–19574.

Batenjany, M. M.; Wang, Z.-Q.; Huang, C.-H.; Levin, I. W. Bilayer packing characteristics of mixed chain phospholipid derivatives: Raman spectroscopic and differential scanning calorimetric studies of 1-stearoyl-2-capryl-sn-glycero-3-phosphocholine (C(18): C(10)PC) and 1-stearoyl-2-capryl-sn-glycero-3-phospho-N-trimethylpropanolamine (C(18): C(10)TMPC). *Biochim. Biophys. Acta, Biomembr.* 1994, 1192, 205−214.

Batta, G.; Soltész, L.; Kovács, T.; Bozó, T.; Mészár, Z.; Kellermayer, M.; Szöllősi, J.; Nagy, P. Alterations in the Properties of the Cell Membrane Due to Glycosphingolipid Accumulation in a Model of Gaucher Disease. *Scientific Reports* 2018, *8*.

Behzadi, S.; Serpooshan, V.; Tao, W.; Hamaly, M. A.; Alkawareek, M. Y.; Dreaden, E. C.; Brown, D.; Alkilany, A. M.; Farokhzad, O. C.; Mahmoudi, M. Cellular Uptake of Nanoparticles: Journey inside the Cell. *Chemical Society Reviews* 2017, *46*, 4218–4244.

Briggs, J.; Chung, H.; Caffrey, M. The Temperature-Composition Phase Diagram and Mesophase Structure Characterization of the monoolein/Water System. *Journal de Physique II* 1996, 6 (5), 723–751.

Brown, K. G.; Peticolas, W. L.; Brown, E. Raman Studies of Conformational Changes in Model Membrane Systems. *Biochem. Biophys. Res. Commun.* 1973, 54, 358−364.

Bui, T. T.; Suga, K.; Umakoshi, H. Roles of Sterol Derivatives in Regulating the Properties of Phospholipid Bilayer Systems. *Langmuir* 2016, 32 (24), 6176−6184.

Calori, I. R.; Pazin, W. M.; Brunaldi, K.; Pellosi, D. S.; Caetano, W.; Tedesco, A. C.; Hioka, N. Laurdan as Fluorescent Probe to Determinate the Critical Micelle Temperature of Polymers from Pluronic®-Coated Fluid Phase Liposomes. J*ournal of Molecular Liquids* 2019, 294, 111562.

Carnie, S.; Israelachvili, J. N.; Pailthorpe, B. A. Lipid Packing and Transbilayer Asymmetries of Mixed Lipid Vesicles. *Biochimica et Biophysica Acta (BBA) - Biomembranes* 1979, *554*, 340–357.

Chen, F.; Bian, M.; Nahmou, M.; Myung, D.; Goldberg, J. L. Fusogenic Liposome-Enhanced Cytosolic Delivery of Magnetic Nanoparticles. *RSC Advances* 2021, *11*, 35796–35805.

Chung, H.; Caffrey, M. The Curvature Elastic-Energy Function of the Lipid–Water Cubic Mesophase. *Nature* 1994, 368 (6468), 224–226.

Cistola, D. P.; Hamilton, J. A.; Jackson, D.; Small, D. M. Ionization and Phase Behavior of Fatty Acids in Water: Application of the Gibbs Phase Rule. *Biochemistry* 1988, 27 (6), 1881−1888.

Costigan, S. C.; Booth, P. J.; Templer, R. H. Estimations of Lipid Bilayer Geometry in Fluid Lamellar Phases. *Biochimica et Biophysica Acta (BBA) - Biomembranes* 2000, *1468*, 41–54.

Cui, C.; Xue, Y.-N.; Wu, M.; Zhang, Y.; Yu, P.; Liu, L.; Zhuo, R.-X.; Huang, S.-W. Cellular Uptake, Intracellular Trafficking, and Antitumor Efficacy of Doxorubicin-Loaded Reduction-Sensitive Micelles. *Biomaterials* 2013, *34*, 3858–3869.

Czamara, K.; Majzner, K.; Pacia, M. Z.; Kochan, K.; Kaczor, A.; Baranska, M. Raman Spectroscopy of Lipids: A Review. *Journal of Raman Spectroscopy* 2014, 46 (1), 4–20.

Czeslik, C.; Winter, R.; Rapp, G.; Bartels, K. Temperature- and Pressure-Dependent Phase Behavior of Monoacylglycerides Monoolein and Monoelaidin. *Biophysical Journal* 1995, 68 (4), 1423–1429.

Demurtas, D.; Guichard, P.; Martiel, I.; Mezzenga, R.; Hébert, C.; Sagalowicz, L. Direct Visualization of Dispersed Lipid Bicontinuous Cubic Phases by Cryo-Electron Tomography. *Nature Communications* 2015, 6.

Deshpande, S.; Singh, N. Influence of Cubosome Surface Architecture on Its Cellular Uptake Mechanism. *Langmuir* 2017, *33*, 3509–3516.

Digiacomo, L.; Cardarelli, F.; Pozzi, D.; Palchetti, S.; Digman, M. A.; Gratton, E.; Capriotti, A. L.; Mahmoudi, M.; Caracciolo, G. An Apolipoprotein-Enriched Biomolecular Corona Switches the Cellular Uptake Mechanism and Trafficking Pathway of Lipid Nanoparticles. *Nanoscale* 2017, *9*, 17254–17262.

Dorrance, A. Increased Membrane Sphingomyelin and Arachidonic Acid in Stroke-Prone Spontaneously Hypertensive Rats. *American Journal of Hypertension* 2001, *14*, 1149–1153.

dos Santos, T.; Varela, J.; Lynch, I.; Salvati, A.; Dawson, K. A. Effects of Transport Inhibitors on the Cellular Uptake of Carboxylated Polystyrene Nanoparticles in Different Cell Lines. *PLoS ONE* 2011, *6*.

Eckardstein, K. L.; Patt, S.; Kratzel, C.; Kiwit, J. C.; Reszka, R. Local Chemotherapy of F98 Rat Glioblastoma with Paclitaxel and Carboplatin Embedded in Liquid Crystalline Cubic Phases. *Journal of Neuro-Oncology* 2005, *72*, 209–215.

Edmond, V.; Dufour, F.; Poiroux, G.; Shoji, K.; Malleter, M.; Fouqué, A.; Tauzin, S.; Rimokh, R.; Sergent, O.; Penna, A.; *et al.* Downregulation of Ceramide Synthase-6 during Epithelial-to-Mesenchymal Transition Reduces Plasma Membrane Fluidity and Cancer Cell Motility. *Oncogene* 2014, *34*, 996–1005.

Eynaudi, A.; Díaz-Castro, F.; Bórquez, J. C.; Bravo-Sagua, R.; Parra, V.; Troncoso, R. Differential Effects of Oleic and Palmitic Acids on Lipid Droplet-Mitochondria Interaction in the Hepatic Cell Line Hepg2. *Frontiers in Nutrition* 2021, *8*.

Farokhzad, O. C.; Langer, R. Impact of Nanotechnology on Drug Delivery. *ACS Nano* 2009, 3, 16–20.

Fox, C. B.; Uibel, R. H.; Harris, J. M. Detecting Phase Transitions in Phosphatidylcholine Vesicles by Raman Microscopy and Self-Modeling Curve Resolution. *J. Phys. Chem. B* 2007, 111, 11428−11436.

Fujimoto, K.; Iwasaki, C.; Kawaguchi, H.; Yasugi, E.; Oshima, M. Cell Membrane Dynamics and the Induction of Apoptosis by Lipid Compounds. *FEBS Letters* 1999, *446*, 113–116.

Garg, G.; Saraf, S.; Saraf, S. Cubosomes: An Overview. *Biological & Pharmaceutical Bulletin* 2007, 30, 350–353.

Gault, C. R.; Obeid, L. M.; Hannun, Y. A. An Overview of Sphingolipid Metabolism: From Synthesis to Breakdown. *Advances in Experimental Medicine and Biology* 2010, 1–23.

Gaus, K.; Gratton, E.; Kable, E. P.; Jones, A. S.; Gelissen, I.; Kritharides, L.; Jessup, W. Visualizing Lipid Structure and Raft Domains in Living Cells with Two-Photon Microscopy. *Proceedings of the National Academy of Sciences* 2003, *100*, 15554–15559.

H. Wu, J. Li, Q. Zhang, X. Yan, L. Guo, X. Gao, M. Qiu, X. Jiang, R. Lai and H. Chen, *European Journal of Pharmaceutics and Biopharmaceutics*, 2012, 80, 368–378.

Harris, F. M.; Best, K. B.; Bell, J. D. Use of Laurdan Fluorescence Intensity and Polarization to Distinguish between Changes in Membrane Fluidity and Phospholipid Order. *Biochimica et Biophysica Acta (BBA) - Biomembranes* 2002, *1565*, 123–128.

Hattori, T.; Andoh, T.; Sakai, N.; Yamada, H.; Kameyama, Y.; Ohki, K.; Nozawa, Y. Membrane Phospholipid Composition and Membrane Fluidity of Human Brain Tumour: A Spin Label Study. *Neurological Research* 1987, *9*, 38–43.

Hirlekar, R.; Jain, S.; Patel, M.; Garse, H.; Kadam, V. Hexosomes: A Novel Drug Delivery System. *Current Drug Delivery* 2010, 7, 28–35.

Hou, F.; Wang, H.; Zhang, Y.; Zhu, N.; Liu, H.; Li, J. Construction and Evaluation of Folic Acid-Modified 3-Bromopyruvate Cubosomes. *Medical Science Monitor* 2020, *26*.

Hou, X.; Zaks, T.; Langer, R.; Dong, Y. Lipid Nanoparticles for Mrna Delivery. *Nature Reviews Materials* 2021, *6*, 1078–1094.

Huang, C.; Mason, J. T.; Levin, I. W. Raman spectroscopic study of saturated mixed-chain phosphatidylcholine multilamellar dispersions. *Biochemistry* 1983, 22 (11), 2775−2780.

Hyde, S. T.; Andersson, S. A Cubic Structure Consisting of a Lipid Bilayer Forming an Infinite Periodic Minimum Surface of the Gyroid Type in the Glycerolmonooleat-Water System. *Zeitschrift für Kristallographie - Crystalline Materials* 1984, 168 (1–4), 213–220.

Israelachvili, J. N.; Mitchell, D. J.; Ninham, B. W. Theory of Self-Assembly of Hydrocarbon Amphiphiles into Micelles and Bilayers. *Journal of the Chemical Society, Faraday Transactions 2* 1976, *72*, 1525.

Jang, E.-J.; Choi, W. R.; Kim, S.-Y.; Hong, S.-S.; Rhee, I.; Lee, S.-J.; Choi, S. W.; Choi, H.-G.; Lim, S.-J. 2-Hydroxyoleic Acid-Inserted Liposomes as a Multifunctional Carrier of Anticancer Drugs. *Drug Delivery* 2017, *24*, 1587–1597.

Jourd'heuil, D.; Aspinall, A.; Reynolds, J. D.; Meddings, J. B. Membrane Fluidity Increases during Apoptosis of Sheep Ileal Peyer's Patch B Cells. *Canadian Journal of Physiology and Pharmacology* 1996, *74*, 706–711.

Kaddah, S.; Khreich, N.; Kaddah, F.; Charcosset, C.; Greige-Gerges, H. Cholesterol Modulates the Liposome Membrane Fluidity and Permeability for a Hydrophilic Molecule. *Food and Chemical Toxicology* 2018, 113, 40–48.

Kim, H.; Sung, J.; Chang, Y.; Alfeche, A.; Leal, C. Microfluidics Synthesis of Gene Silencing Cubosomes. *ACS Nano* 2018, *12*, 9196–9205.

Kim, S.; Shi, Y.; Kim, J. Y.; Park, K.; Cheng, J.-X. Overcoming the Barriers in Micellar Drug Delivery: Loading Efficiency,*in Vivo*Stability, and Micelle–Cell Interaction. *Expert Opinion on Drug Delivery* 2009, 7, 49–62.

Kong, H.; Zheng, C.; Yi, K.; Mintz, R. L.; Lao, Y.-H.; Tao, Y.; Li, M. An Antifouling Membrane-Fusogenic Liposome for Effective Intracellular Delivery in Vivo. *Nature Communications* 2024, *15*.

Kou, L.; Sun, J.; Zhai, Y.; He, Z. The Endocytosis and Intracellular Fate of Nanomedicines: Implication for Rational Design. *Asian Journal of Pharmaceutical Sciences* 2013, *8*, 1–10.

Kube, S.; Hersch, N.; Naumovska, E.; Gensch, T.; Hendriks, J.; Franzen, A.; Landvogt, L.; Siebrasse, J.-P.; Kubitscheck, U.; Hoffmann, B.; *et al.* Fusogenic Liposomes as Nanocarriers for the Delivery of Intracellular Proteins. *Langmuir* 2017, *33*, 1051–1059.

Kulkarni, C. V.; Wachter, W.; Iglesias-Salto, G.; Engelskirchen, S.; Ahualli, S. Monoolein: A Magic Lipid? *Phys. Chem. Chem. Phys*. 2011, 13, 3004–3021.

Kumar, V. V. Complementary Molecular Shapes and Additivity of the Packing Parameter of Lipids. *Proceedings of the National Academy of Sciences* 1991, 88, 444–448.

Lakkaraju, A.; Rahman, Y.-E.; Dubinsky, J. M. Low-Density Lipoprotein Receptor-Related Protein Mediates the Endocytosis of Anionic Liposomes in Neurons. *Journal of Biological Chemistry* 2002, *277*, 15085–15092.

Lakowicz, J. R. *Principles of Fluorescence Spectroscopy*; Springer: New York, NY, 2006.

Lantzch, G.; Binder, H.; Heerklotz, H.; Wendling, M.; Klose, G. Surface Areas and Packing Constraints in Membranes. A Time-Resolved Fluorescence Study. *Biophysical Chemistry* 1996, 58, 289–302.

Larsson, K.; Tiberg, F. Periodic Minimal Surface Structures in Bicontinuous Lipid–Water Phases and Nanoparticles. *Current Opinion in Colloid & Interface Science* 2005, 9, 365–369.

Le, P. U.; Nabi, I. R. Distinct Caveolae-Mediated Endocytic Pathways Target the Golgi Apparatus and the Endoplasmic Reticulum. *Journal of Cell Science* 2003, *116*, 1059–1071.

Levitan, I. Evaluating Membrane Structure by Laurdan Imaging: Disruption of Lipid Packing by Oxidized Lipids. *Current Topics in Membranes* 2021, 235–256.

Li, Y.; Angelova, A.; Hu, F.; Garamus, V. M.; Peng, C.; Li, N.; Liu, J.; Liu, D.; Zou, A. Ph Responsiveness of Hexosomes and Cubosomes for Combined Delivery of Brucea Javanica Oil and Doxorubicin. *Langmuir* 2019, 35, 14532–14542.

Lis, L. J.; Kauffman, J. W.; Shriver, D. F. Raman Spectroscopic Detection and Examination of the Interaction of Amino Acids, Polypeptides and Proteins with the Phosphatidylcholine Lamellar Structure. *Biochimica et Biophysica Acta (BBA) - Biomembranes* 1976, 436 (3), 513–522.

Liu, J.; Huang, Y.; Kumar, A.; Tan, A.; Jin, S.; Mozhi, A.; Liang, X.-J. Ph-Sensitive Nano-Systems for Drug Delivery in Cancer Therapy. *Biotechnology Advances* 2014, 32, 693–710.

Llado, V.; Gutierrez, A.; Martínez, J.; Casas, J.; Terés, S.; Higuera, M.; Galmés, A.; Saus, C.;

Besalduch, J.; Busquets, X.; *et al.* Minerval Induces Apoptosis in Jurkat and Other Cancer Cells. *Journal of Cellular and Molecular Medicine* 2010, *14*, 659–670.

Lopez, J.; Lai-Kwon, J.; Molife, R.; Welsh, L.; Tunariu, N.; Roda, D.; Fernández-García, P.; Lladó, V.; McNicholl, A. G.; Rosselló, C. A.; *et al.* A Phase 1/2A Trial of Idroxioleic Acid: First-in-Class Sphingolipid Regulator and Glioma Cell Autophagy Inducer with Antitumor Activity in Refractory Glioma. *British Journal of Cancer* 2023, *129*, 811–818.

Marcilla-Etxenike, A.; Martín, M. L.; Noguera-Salvà, M. A.; García-Verdugo, J. M.; Soriano-Navarro, M.; Dey, I.; Escribá, P. V.; Busquets, X. 2-Hydroxyoleic Acid Induces ER Stress and Autophagy in Various Human Glioma Cell Lines. *PLoS ONE* 2012, *7*.

Martin, M. L.; Liebisch, G.; Lehneis, S.; Schmitz, G.; Alonso-Sande, M.; Bestard-Escalas, J.; Lopez, D. H.; García-Verdugo, J. M.; Soriano-Navarro, M.; Busquets, X.; *et al.* Sustained Activation of Sphingomyelin Synthase by 2-Hydroxyoleic Acid Induces Sphingolipidosis in Tumor Cells. *Journal of Lipid Research* 2013, *54*, 1457–1465.

Maté, S.; Busto, J. V.; García-Arribas, A. B.; Sot, J.; Vazquez, R.; Herlax, V.; Wolf, C.; Bakás, L.; Goñi, F. M. N-Nervonoylsphingomyelin (C24:1) Prevents Lateral Heterogeneity in Cholesterol-Containing Membranes. *Biophysical Journal* 2014, *106*, 2606–2616.

Mathews, P. D.; Mertins, O.; Angelov, B.; Angelova, A. Cubosomal Lipid Nanoassemblies with Ph-Sensitive Shells Created by Biopolymer Complexes: A Synchrotron Saxs Study. *Journal of Colloid and Interface Science* 2022, 607, 440–450.

Mazzoni, S.; Barbosa, L. R.; Funari, S. S.; Itri, R.; Mariani, P. Cytochrome-C Affects the Monoolein Polymorphism: Consequences for Stability and Loading Efficiency of Drug Delivery Systems. *Langmuir* 2016, 32, 873–881.

Mertins, O.; Mathews, P. D.; Angelova, A. Advances in the Design of Ph-Sensitive Cubosome Liquid Crystalline Nanocarriers for Drug Delivery Applications. *Nanomaterials* 2020, 10, 963.

Mezzenga, R.; Seddon, J. M.; Drummond, C. J.; Boyd, B. J.; Schröder-Turk, G. E.; Sagalowicz, L. Nature-inspired Design and Application of Lipidic Lyotropic Liquid Crystals. *Advanced Materials* 2019, 31, 1900818. Misquitta, Y.; Caffrey, M. Detergents Destabilize the Cubic Phase of Monoolein: Implications for Membrane Protein Crystallization. *Biophysical Journal* 2003, 85, 3084–3096.

Miyaji, M. et al. Role of membrane sphingomyelin and ceramide in platform formation for Fas-mediated apoptosis. *The Journal of Experimental Medicine* 202, 249–259 (2005).

Nagarajan, R. Molecular Packing Parameter and Surfactant Self-Assembly: The Neglected Role of the Surfactant Tail. *Langmuir* 2001, 18 (1), 31–38.

Nakano, M.; Kamo, T.; Sugita, A.; Handa, T. Detection of Bilayer Packing Stress and Its Release in Lamellar-Cubic Phase Transition by Time-Resolved Fluorescence Anisotropy. *The Journal of Physical Chemistry B* 2005, 109, 4754–4760.

Nakano, M.; Teshigawara, T.; Sugita, A.; Leesajakul, W.; Taniguchi, A.; Kamo, T.; Matsuoka, H.; Handa, T. Dispersions of Liquid Crystalline Phases of the Monoolein/Oleic Acid/Pluronic F127 System. *Langmuir* 2002, 18 (24), 9283–9288.

Nakazawa, I.; Iwaizumi, M. A Role of the Cancer Cell Membrane Fluidity in the Cancer

Metastases: An ESR Study. *The Tohoku Journal of Experimental Medicine* 1989, *157*, 193–198.

Notman, R.; Noro, M. G.; Anwar, J. Interaction of Oleic Acid with Dipalmitoylphosphatidylcholine (DPPC) Bilayers Simulated by Molecular Dynamics. *The Journal of Physical Chemistry B* 2007, *111*, 12748–12755.

Noutsi, P.; Gratton, E.; Chaieb, S. Assessment of Membrane Fluidity Fluctuations during Cellular Development Reveals Time and Cell Type Specificity. *PLOS ONE* 2016, *11*.

Okamoto, Y., Hamaguchi, K., Watanabe, M., Watanabe, N. & Umakoshi, H. Characterization of phase separated planar lipid bilayer membrane by fluorescence ratio imaging and scanning probe microscope. *Membranes* 2022, 12, 770.

Okamoto, Y., Kishi, Y., Suga, K. & Umakoshi, H. Induction of chiral recognition with lipid Nanodomains produced by polymerization. *Biomacromolecules* 2017, 18, 1180–1188.

Oku, N., Kendall, D. A. & MacDonald, R. C. A simple procedure for the determination of the trapped volume of liposomes. *Biochimica et Biophysica Acta (BBA) - Biomembranes* 1982, 691, 332–340,

Olechowska, K., Mach, M., Hąc-Wydro, K. & Wydro, P. The influence of 2-hydroxyoleic acid – an anticancer drug – on model membranes of different fluidity modulated by the cholesterol content. *Journal of Molecular Liquids* 2019 283, 756–762.

Oliveira, C.; Ferreira, C. J.; Sousa, M.; Paris, J. L.; Gaspar, R.; Silva, B. F.; Teixeira, J. A.; Ferreira-Santos, P.; Botelho, C. M. A Versatile Nanocarrier—Cubosomes, Characterization, and Applications. *Nanomaterials* 2022, 12, 2224.

Oncul, S. *et al.* Liquid ordered phase in cell membranes evidenced by a hydration-sensitive probe: Effects of cholesterol depletion and apoptosis. *Biochimica et Biophysica Acta (BBA) - Biomembranes* 2010 1798, 1436–1443.

Parasassi, T.; Gratton, E. Packing of phospholipid vesicles studied by oxygen quenching of Laurdan fluorescence. *Journal of Fluorescence* 1992 2, 167–174.

Parasassi, T.; Gratton, E. Membrane Lipid Domains and Dynamics as Detected by Laurdan Fluorescence. *Journal of Fluorescence* 1995, 5 (1), 59–69.

Parasassi, T.; Krasnowska, E. K.; Bagatolli, L.; Gratton, E. Laurdan and Prodan as Polarity-Sensitive Fluorescent Membrane Probes. *J. Fluoresc.* 1998, 8, 365−373.

Pimenta, B. V.; Madrid, R. R. M.; Mathews, P. D.; Riske, K. A.; Loh, W.; Angelov, B.; Angelova, A.; Mertins, O. Interaction of Polyelectrolyte-Shell Cubosomes with Serum Albumin for Triggering Drug Release in Gastrointestinal Cancer. *Journal of Materials Chemistry B* 2023, 11, 2490–2503.

Pokorna, S. *et al.* Laurdan in live cell imaging: Effect of acquisition settings, cell culture conditions and data analysis on generalized polarization measurements. *Journal of Photochemistry and Photobiology B: Biology* 2022 228, 112404.

Prajapati, R.; Gontsarik, M.; Yaghmur, A.; Salentinig, S. PH-Responsive Nano-Self-Assemblies of the Anticancer Drug 2-Hydroxyoleic Acid. *Langmuir* 2019, 35 (24), 7954–7961.

Pramanik, Z. Xu, S. H. Shamsuddin, Y. S. Khaled, N. Ingram, T. Maisey, D. C. Tomlinson, P. L. Coletta, D. Jayne, T. Hughes, A. I. I. Tyler and P. A. Millner, *ACS Applied Materials & Interfaces*, 2022, 14, 11078–11091.

Qiu, T.; Gu, P.; Wusiman, A.; Ni, H.; Xu, S.; Zhang, Y.; Zhu, T.; He, J.; Liu, Z.; Hu, Y.; et al. Immunoenhancement effects of chitosan-modified ginseng stem-leaf saponins-encapsulated cubosomes as an ajuvant. *Colloids Surf. B Biointerfaces* 2021, *204*, 111799.

R. Nisha, P. Kumar, U. Kumar, N. Mishra, P. Maurya, P. Singh, H. Tabassum, Alka, S. Singh, A. Guleria and S. A. Saraf, *International Journal of Pharmaceutics*, 2022, 622, 121848.

R. Nisha, P. Kumar, U. Kumar, N. Mishra, P. Maurya, S. Singh, P. Singh, A. Guleria, S. Saha and S. A. Saraf, *Molecular Pharmaceutics*, 2020, 18, 1102–1120.

R. Petrilli, J. O. Eloy, F. S. G. Praça, J. O. Del Ciampo, M. C. A. Fantini, M. J. V. Fonseca and M. V. L. B. Bentley, *Journal of Biomedical Nanotechnology*, 2016, 12, 1063–1075.

Rajesh, S.; Zhai, J.; Drummond, C. J.; Tran, N. Synthetic Ionizable Aminolipids Induce a Ph Dependent Inverse Hexagonal to Bicontinuous Cubic Lyotropic Liquid Crystalline Phase Transition in Monoolein Nanoparticles. *Journal of Colloid and Interface Science* 2021, 589, 85–95.

Rajesh, S.; Zhai, J.; Drummond, C.; Tran, N. Novel PH-Responsive Cubosome and Hexosome Lipid Nanocarriers of Sn-38 Are Prospective for Cancer Therapy. *Pharmaceutics* 2022, 14, 2175.

Reiss-Husson, F. Structure Des Phases Liquide-Cristallines de Différents Phospholipides, Monoglycérides, Sphingolipides, Anhydres Ou En Présence d'eau. *Journal of Molecular Biology* 1967, 25, 363–382.

Rodrigues, L.; Schneider, F.; Zhang, X.; Larsson, E.; Moodie, L. W. K.; Dietz, H.; Papadakis, C. M.; Winter, G.; Lundmark, R.; Hubert, M. Cellular Uptake of Self-Assembled Phytantriol-Based Hexosomes Is Independent of Major Endocytic Machineries. *Journal of Colloid and Interface Science* 2019, *553*, 820–833.

Rosa, A.; Murgia, S.; Putzu, D.; Meli, V.; Falchi, A. M. Monoolein-Based Cubosomes Affect Lipid Profile in Hela Cells. *Chemistry and Physics of Lipids* 2015, *191*, 96–105.

S. Aleandri, D. Bandera, R. Mezzenga and E. M. Landau. Biotinylated Cubosomes: A Versatile Tool for Active Targeting and Codelivery of Paclitaxel and a Fluorescein-Based Lipid Dye. *Langmuir* 2015, 31, 12770–12776.

S. Deshpande, E. Venugopal, S. V. Ramagiri, J. Bellare, G. Kumaraswamy and N. Singh. Enhancing Cubosome Functionality by Coating with a Single Layer of Poly-ε-lysine, *ACS Applied Materials & Interfaces*, 2014, 6, 17126–17133.

Salentinig, S.; Sagalowicz, L.; Glatter, O. Self-Assembled Structures and PKa Value of Oleic Acid in Systems of Biological Relevance. *Langmuir* 2010, 26 (14), 11670−11679.

Salim, M.; Wan Iskandar, W. F.; Patrick, M.; Zahid, N. I.; Hashim, R. Swelling of Bicontinuous Cubic Phases in Guerbet Glycolipid: Effects of Additives. *Langmuir* 2016, 32 (22), 5552–5561.

Sanchez, S. A., Tricerri, M. A. & Gratton, E. Laurdan generalized polarization fluctuations measures membrane packing micro-heterogeneity in vivo. *Proceedings of the National Academy of Sciences* 2012 109, 7314–7319.

Slotte, J. P. & Ramstedt, B. The functional role of sphingomyelin in cell membranes. *European Journal of Lipid Science and Technology* 2007 109, 977–981.

Sot, J. *et al.* Phase-selective staining of model and cell membranes, lipid droplets and lipoproteins with fluorescent solvatochromic pyrene probes. *Biochimica et Biophysica Acta (BBA) - Biomembranes* 2021 1863, 183470.

St. Clair, J. W., Kakuda, S. & London, E. Induction of ordered lipid raft domain formation by loss of lipid asymmetry. *Biophysical Journal* 119, 483–492 (2020).

Strachan, J. B.; Dyett, B. P.; Nasa, Z.; Valery, C.; Conn, C. E. Toxicity and Cellular Uptake of Lipid Nanoparticles of Different Structure and Composition. *Journal of Colloid and Interface Science* 2020, *576*, 241–251.

Suga, K.; Otsuka, Y.; Okamoto, Y.; Umakoshi, H. Gel-Phase-like Ordered Membrane Properties Observed in Dispersed Oleic Acid/1-Oleoylglycerol Self-Assemblies: Systematic Characterization Using Raman Spectroscopy and a LAURDAN Fluorescent Probe. *Langmuir* 2018, 34 (5), 2081–2088.

Suga, K.; Umakoshi, H. Detection of Nanosized Ordered Domains in DOPC/DPPC and DOPC/CH Binary Lipid Mixture Systems of Large Unilamellar Vesicles Using a Tempo Quenching Method. *Langmuir* 2013, 29 (15), 4830–4838.

Suga, K.; Yoshida, T.; Ishii, H.; Okamoto, Y.; Nagao, D.; Konno, M.; Umakoshi, H. Membrane surface-enhanced Raman spectroscopy for sensitive detection of molecular behavior of lipid assemblies. *Anal. Chem.* 2015, 87, 4772−4780.

Szlasa, W., Zendran, I., Zalesińska, A., Tarek, M. & Kulbacka, J. Lipid composition of the cancer cell membrane. *Journal of Bioenergetics and Biomembranes* 2020 52, 321–342.

Tanford, C. Micelle Shape and Size. *The Journal of Physical Chemistry* 1972, 76, 3020–3024.

Terés, S.; Lladó, V.; Higuera, M.; Barceló-Coblijn, G.; Martin, M. L.; Noguera-Salvà, M. A.; Marcilla-Etxenike, A.; García-Verdugo, J. M.; Soriano-Navarro, M.; Saus, C.; *et al.* 2-Hydroxyoleate, a Nontoxic Membrane Binding Anticancer Drug, Induces Glioma Cell Differentiation and Autophagy. *Proceedings of the National Academy of Sciences* 2012, *109*, 8489–8494.

Terés, S.; Lladó, V.; Higuera, M.; Barceló-Coblijn, G.; Martin, M. L.; Noguera-Salvà, M. A.; Marcilla-Etxenike, A.; García-Verdugo, J. M.; Soriano-Navarro, M.; Saus, C.; *et al.* Normalization of Sphingomyelin Levels by 2-Hydroxyoleic Acid Induces Autophagic Cell Death of SF767 Cancer Cells. *Autophagy* 2012, *8*, 1542–1544.

Tian, Y.; Li, J.; Zhu, J.; Zhu, N.; Zhang, H.; Liang, L.; Sun, L. Folic Acid-Targeted Etoposide Cubosomes for Theranostic Application of Cancer Cell Imaging and Therapy. *Medical Science Monitor* 2017, *23*, 2426–2435.

Tilley, A. J.; Drummond, C. J.; Boyd, B. J. Disposition and Association of the Steric Stabilizer Pluronic® F127 in Lyotropic Liquid Crystalline Nanostructured Particle Dispersions. *Journal of Colloid and Interface Science* 2013, 392, 288–296.

Un, K., Sakai-Kato, K., Oshima, Y., Kawanishi, T. & Okuda, H. Intracellular Trafficking Mechanism, from intracellular uptake to extracellular efflux, for phospholipid/cholesterol liposomes. *Biomaterials* 2012 33, 8131–8141.

Valanciunaite, J.; Kempf, E.; Seki, H.; Danylchuk, D. I.; Peyriéras, N.; Niko, Y.; Klymchenko, A. S. Polarity Mapping of Cells and Embryos by Improved Fluorescent Solvatochromic Pyrene Probe. *Analytical Chemistry* 2020, *92*, 6512–6520.

Wei, Y.; Zhang, J.; Zheng, Y.; Gong, Y.; Fu, M.; Liu, C.; Xu, L.; Sun, C. C.; Gao, Y.; Qian, S. Cubosomes with Surface Cross-Linked Chitosan Exhibit Sustained Release and Bioavailability Enhancement for Vinpocetine. *RSC Advances* 2019, *9*, 6287–6298.

Xia, T.; Kovochich, M.; Liong, M.; Zink, J. I.; Nel, A. E. Cationic Polystyrene Nanosphere Toxicity Depends on Cell-Specific Endocytic and Mitochondrial Injury Pathways. *ACS Nano* 2007, *2*, 85–96.

Yaghmur, A.; Ghayas, S.; Jan, H.; Kalaycioglu, G. D.; Moghimi, S. M. Omega-3 Fatty Acid Nanocarriers: Characterization and Potential Applications. *Current Opinion in Colloid & Interface Science* 2023, 67, 101728.

Yang, M.; Li, J.; Gu, P.; Fan, X. The Application of Nanoparticles in Cancer Immunotherapy: Targeting Tumor Microenvironment. *Bioactive Materials* 2021, 6, 1973–1987.

Yoo, B. K.; Baskaran, R.; Madheswaran, T.; Sundaramoorthy, P.; Kim, H. M. Entrapment of Curcumin into Monoolein-Based Liquid Crystalline Nanoparticle Dispersion for Enhancement of Stability and Anticancer Activity. *International Journal of Nanomedicine* 2014, 3119.

Yu, H.; Angelova, A.; Angelov, B.; Dyett, B.; Matthews, L.; Zhang, Y.; El Mohamad, M.; Cai, X.; Valimehr, S.; Drummond, C. J.; et al. Real-time Ph-dependent Self-assembly of Ionisable Lipids from Covid-19 Vaccines and in Situ Nucleic Acid Complexation. *Angewandte Chemie International Edition* 2023, 62.

Yu, H.; Dyett, B.; Kirby, N.; Cai, X.; Mohamad, M. E.; Bozinovski, S.; Drummond, C. J.; Zhai, J. Ph-dependent Lyotropic Liquid Crystalline Mesophase and Ionization Behavior of Phytantriol-based Ionizable Lipid Nanoparticles. *Small* 2024, 20.

Zabara, M.; Ren, Q.; Amenitsch, H.; Salentinig, S. Bioinspired Antimicrobial Coatings from Peptide-Functionalized Liquid Crystalline Nanostructures. *ACS Applied Bio Materials* 2021, *4*, 5295–5303.

Zhai, J.; Fan, B.; Thang, S. H.; Drummond, C. J. Novel Amphiphilic Block Copolymers for the Formation of Stimuli-Responsive Non-Lamellar Lipid Nanoparticles. *Molecules* 2021, 26 (12), 3648.

Zhai, J.; Tan, F. H.; Luwor, R. B.; Srinivasa Reddy, T.; Ahmed, N.; Drummond, C. J.; Tran, N. *In Vitro* and *in Vivo* Toxicity and Biodistribution of Paclitaxel-Loaded Cubosomes as a Drug Delivery Nanocarrier: A Case Study Using an A431 Skin Cancer Xenograft Model. *ACS Applied Bio Materials* 2020, *3*, 4198–4207.

Zhang, G.; Huang, L.; Wu, J.; Liu, Y.; Zhang, Z.; Guan, Q. Doxorubicin-Loaded Folate-Mediated Ph-Responsive Micelle Based on Bletilla Striata Polysaccharide: Release Mechanism, Cellular Uptake Mechanism, Distribution, Pharmacokinetics, and Antitumor Effects. *International Journal of Biological Macromolecules* 2020, *164*, 566–577.

Zhang, Y.-N., Poon, W., Tavares, A. J., McGilvray, I. D. & Chan, W. C. W. Nanoparticle–Liver Interactions: Cellular uptake and hepatobiliary elimination. *Journal of Controlled Release* 2016 240, 332–348.

Zhang, Z.; Xiong, X.; Wan, J.; Xiao, L.; Gan, L.; Feng, Y.; Xu, H.; Yang, X. Cellular Uptake and Intracellular Trafficking of PEG-B-Pla Polymeric Micelles. *Biomaterials* 2012, *33*, 7233–7240.

Zhao, J.; Mao, S. Tuning the Membrane Fluidity of Liposomes for Desirable in Vivo Fate with Enhanced Drug Delivery. *Advances in Biomembranes and Lipid Self-Assembly* 2021, 67–106.

Zhao, J.; Su, J.; Qin, L.; Zhang, X.; Mao, S. Exploring the Influence of Inhaled Liposome Membrane Fluidity on Its Interaction with Pulmonary Physiological Barriers. *Biomaterials Science* 2020, 8 (23), 6786–6797.

Zhaorigetu, S.; Rodriguez-Aguayo, C.; Sood, A. K.; Lopez-Berestein, G.; Walton, B. L. Delivery of Negatively Charged Liposomes into the Atherosclerotic Plaque of Apolipoprotein E-Deficient Mouse Aortic Tissue. *Journal of Liposome Research* 2014, *24*, 182–190.

Nomenclatures

$1/P$ = membrane fluidity [-]

a_0 = area of hydrophilic headgroup [Å^2]

a = lattice parameter [nm]

a_{Im3m} = lattice parameter of *Im3m* space group [nm]

a_{Pn3m} = lattice parameter of *Pn3m* space group [nm]

CPP = critical packing parameter [-]

d-space = interlamellar distance [nm]

FWHM = the full width at half maximum [-]

G = correction factor [-]

GP = general polarization [-]

I = fluorescence intensity [a.u]

lc = critical length of the hydrocarbon chain [Å]

p*K*a = acidity constent [-]

pH = potential of hydrogen [-]

q = scattering vector [nm^{-1}]

r_w = water channel radius [nm^{-1}]

R = lipid chain packing [-]

S = lipid chain torsion [-]

T = temperature [°C]

ν = hydrophobic tail volume [Å^3]

λ = wavelength [nm]

λ_{ex} = excitation wavelength [nm]

λ_{em} = emission wavelength [nm]

ζ = zeta potential [mV]

Abbreviations

2-OHOA	2-hydroxyoleic acid
CB	Cubosome
Chol	Cholesterol
Cryo-TEM	Cryo-transmission electron microscopy
DLS	Dynamic light scattering
DOPC	1,2-dioleoyl-*sn*-glycero-3-phosphocholine
DOPE	1,2-dioleoyl-*sn*-glycero-3-phosphoethanolamine
DOTAP	1,2-dioleoyl-3-trimethylammonium-propane
DOX	Doxorubicin
DPH	1,6-Diphenyl-1,3,5-hexatriene
H_{II}	Hexagonal phase
Im3m	Primitive cubic phase group space
Ia3d	Gyroid cubic phase group space
$L\alpha$	Lamellar phase
LNP	Lipid nanoparticle
MO	Monoolein, 1-Oleoyl-rac-glycerol
MLV	Multilamellar vesicle
PA	Phosphatidic acid
PC	Phosphatidylcholine
PDI	Polydispersity index
PE	Phosphatidylethanolamine
PEG	Polyethylene glycol
Pn3m	Diamond cubic phase group space
PS	Phosphatidylserine
Pluronic F127	Poly (ethylene oxide)-poly-(propylene oxide)-poly (ethylene oxide)
PYT	Phytantriol
Q_{II}	Cubic phase
Q_{II}^{G}	Gyroid cubic phase

Q_{II}^{D}	Diamond cubic phase
Q_{II}^{P}	Primitive cubic phase
SAXS	Small-angle X-ray scattering
SL	Sphingolipid
TEM	Transmission electron microscopy
ULV	Unilamellar vesicle

List of Publications

[Papers]

1. Xuehui Rui, Yukihiro Okamoto, Shuichiro Fukushima, Nozomi Morishita Watanabe, Hiroshi Umakoshi. Investigating the impact of 2-OHOA-embedded liposomes on biophysical properties of cancer cell membranes via Laurdan two-photon microscopy imaging. *Scientific Reports*, 14 (1), Article number: 15831 (2024).
2. Xuehui Rui, Yukihiro Okamoto, Nozomi Morishita-Watanabe, Taro Shimizu, Ward Wakileh, Kajimura Naoko, Hiroshi Umakoshi. Preparation and characterization of macrophage membrane camouflaged cubosomes as a stabilized and immune evasive biomimetic nano-DDS. *J. Mater. Chem. B*, (2024).
3. Xuehui Rui; Nozomi Watanabe; Yukihiro Okamoto; Ward Wakileh; Hiroshi Umakoshi. Exploring pH-Triggered Lamellar to Cubic Phase Transition in 2-Hydroxyoleic Acid/Monoolein Nano-Dispersions: Insights into Membrane Physicochemical Properties. *J. Phys. Chem. B*, (2024).

[Related Papers]

1. Qiu, Min, Zachary Glass, Jinjin Chen, Mary Haas, Xin Jin, Xuewei Zhao, Xuehui Rui, et al. Lipid Nanoparticle-Mediated Codelivery of Cas9 Mrna and Single-Guide RNA Achieves Liver-Specific in Vivo Genome Editing ofAngptl3. *Proceedings of the National Academy of Sciences* 118(10) (2021).
2. Ma, Feihe, Liu Yang, Zhuorui Sun, Jinjin Chen, Xuehui Rui, Zachary Glass, and Qiaobing Xu. Neurotransmitter-Derived Lipidoids (NT-Lipidoids) for Enhanced Brain Delivery through Intravenous Injection. *Science Advances* 6(30) (2020).

[International Conference]

1. Xuehui Rui, Nozomi Watanabe, Yukihiro Okamoto, Hiroshi Umakoshi. Macrophage membrane camouflaged cubosome for DOX and siRNA delivery. Membrane Symposium 2022 (Kobe, Japan). Poster award.
2. Xuehui Rui, Yukihiro Okamoto, Nozomi Watanabe, Hiroshi Umakoshi. Lipid Nanoparticle Formulation for Enhancing the Membrane Lipid Therapy Performance of 2-OHOA. 16th International Symposium on Nanomedicine, 2023 (Osaka, Japan)

[Article Review]

1. Xuehui Rui. Macrophage membrane camouflaged cubosome for doxorubicin and siRNA delivery. *MEMBRANE*, 48(2), 84–85, (2023).

Acknowledgement

The author expresses deep gratitude to Prof. Dr. Hiroshi Umakoshi (Department of Chemical Science and Engineering, Graduate School of Engineering Science, Osaka University) for his exceptional guidance, valuable advice, and precious support throughout this research. Prof. Dr. Hiroshi Umakoshi's provision of a free and flexible research environment greatly enriched the author's doctoral studies and Prof. Dr. Umakoshi's mentorship played a pivotal role in shaping author's "Research Philosophy". The author is thankful to Prof. Dr. Shinji Deguchi (Department of Mechanical Science and Bioengineering, Graduate School of Engineering Science, Osaka University) and Prof. Dr. Shinji Sakai (Department of Chemical Science and Engineering, Graduate School of Engineering Science, Osaka University) for their valuable comments and suggestions during the completion of this thesis. The author greatly appreciates Assoc. Prof. Dr. Yukihiro Okamoto (Department of Chemical Science and Engineering, Graduate School of Engineering Science, Osaka University) for his generous support and insightful suggestions during the author's doctoral studies. Dr. Yukihiro Okamoto's shared expertise and provision of essential research tools were invaluable to the continuation of this work. The author also would like to express his gratitude to Assist. Prof. Dr. Nozomi Watanabe (Department of Chemical Science and Engineering, Graduate School of Engineering Science, Osaka University). Dr. Watanabe offered gentle and precious suggestions and worm encouragements for the author and provided valuable assistance during the author's research.

The author would like to show his greatest appreciation to Prof. Dr. Kaoru Mitsuoka (Research Center for Ultra-High Voltage Electron Microscopy, Osaka University), Dr. Naoko Kajimura (Research Center for Ultra-High Voltage Electron Microscopy, Osaka University), Dr. Shuichiro Fukushima (R3 Institute for Newly-Emerging Science Design, Osaka University) and Dr. Taro Shimizu (Research Institute for Microbial Diseases, Osaka University) for their kind corporation during this study. The appreciation is extended to Super Photon ring-8 GeV (Spring8) for its previous support during this study.

The author gratefully acknowledges the finical support from Japanese Ministry of Education, Culture, Sports, Science and Technology (MEXT).

Lastly, and most importantly, the author expresses his deepest thanks to his family members for their selfless and unwavering support.